Wake Effects of Large Offshore Wind Farms - a study of the Mesoscale Atmophere

Volker, Patrick

Publication date:
2014

Document Version
Publisher's PDF, also known as Version of record

Wake Effects of Large Offshore Wind Farms - a study of the Mesoscale Atmosphere

2014

Patrick J.H. Volker
DTU Wind Energy PhD-0035(EN)
January 2014

Author: Patrick Johannes Hendrik Volker
Title: Wake Effects of Large Offshore Wind Farms - a study of the Mesoscale Atmosphere
Division: Department of Wind Energy

DTU-PhD-35(EN)
December 2013

Abstract:
The power production contribution to the power system from offshore wind energy is continuously increasing in the northern European countries. A better understanding of the influence of wind farms to those downstream and to the lower atmosphere will help optimising energy production from large wind farm clusters.

Mesoscale models allow the simulation of large domains sufficiently to capture large wind farms and surroundings at reasonable computational costs, but processes below the horizontal resolution remain unresolved and have to be parametrised, such as the effects of the wind turbines to the flow. In the past, several approaches have been introduced, ranging from surface roughness change to drag approaches which usually also add turbulence. A new scheme is implemented in the Weather Research and Forecast (WRF) model. Measurements from Horns Rev I are used to evaluate the new scheme together with that in the WRF model. Results show an improvement of robustness in vertical resolution dependency. Furthermore, the velocity and "turbulence kinetic energy" fields agree better to those of high resolution models.

The two schemes are applied to various problems. A hypothetical offshore wind farm in northern California, shows a sensitivity of the velocity field around the wind farm to atmospheric conditions aloft. For a shallow boundary layer capped by a steep inversion, gravity waves were generated, with related anomalies of the atmospheric variables aloft. Dependencies of the wind farm efficiency and the wind farm's wake recovery to different atmospheric conditions aloft were found in an idealised case study. Moreover, the wind farm efficiency to different climates for wind farm sizes up to 375 km^2 was examined. The modelled production varied with wind climate and were well above 1 $W\,m^{-2}$, contrary to another study. Finally, wind farm shadowing was studied for the worst case scenario, in which two wind farms are perfectly aligned. For this scenario, considerable production losses of the downstream wind farm are expected, even with a separation of 5 wind farm lengths.

ISBN 978-87-92896-78-0

Contract no.:

Group's own reg. no.:

Sponsorship:
WAUDIT
Marie-Curie ESR-FP7

Pages: 132
References: 82

Information Service Department
RisøNational Laboratory for Sustainable Energy
Technical University of Denmark
P.O.Box 49
DK-4000 Roskilde
Denmark
Telephone +45 46774005
bibl@dtu.dk
Fax +45 46774013
www.dtu.dk

1

Abstrakt

Bidraget af elproduktion til elsystemet fra offshore vindkraft er konstant stigende ide nordeuropæiske lande. En bedre forståelse af vindmølleparkers indflydelse på nedstrøms vindmølleparker og på den nedre atmosfære vil hjælpe med at optimere energiproduktion fra store vindmølleparker.

Mesoscale modeller tillader simulering af tilstrækkeligt store domæner der kan repræsentere større vindmølleparker og deres omgivelser til beregningsmæssigt rimelige omkostninger, men ikke-opløste processer under den modellerede horisontale opløsning er nødt til at blive parametriseret, såsom påvirkningerne fra vindmøller på vinden. Flere metoder er tidligere blevet introduceret, fra ændring af overfladeruheder til træghedsmetoder der, desuden normalt, tilføjer turbulens. Et nyt skema er implementeret i Vejr Forskning og Prognose (WRF) modellen. Målinger fra Horns Rev I er anvendt til at evaluere det nye skema sammen med WRF modellen. Resultaterne viser en forbedret robusthed i afhængigheden af den lodrette opløsning. Endvidere stemmer hastigheden og den turbulente kinetiske energi bedre overens med resultater fra høj-opløsnings modeller.

De to skemaer er anvendt på forskellige problemer. En hypotetisk havvindmøllepark i det nordlige Californien viser at hastighedsfeltet omkring vindmølleparken er følsomt overfor de atmosfæriske forhold i højden. Et tyndt grænselag afgrænset af en stejl inversion viste udvikling af gravitationsbølger med tilhørende anomalier i de atmosfæriske variabler i højden. Afhængigheder af vindmølleparkens effektivitet og dets kølvandsgenoprettelse for forskellige atmosfæriske forhold i højden blev fundet i et idealiseret studie. Vindmølleparkens effektivitet i forskellige klimaer for vindmølleparker størrelser op til 375 km^2 blev desuden undersøgt. Den modellerede produktion varierede med vindklimæt og var et godt stykke over 1 W m^{-2}, i modsætning til en andenundersøgelse. Endelig blev skyggeeffekter fra vindmølleparker undersøgt for det værst tænkelige scenarie, hvori to vindmølleparker er på en ret linje. Et betydeligt produktionstab i vindmølleparken nedstrøms er forventligt i et sådant scenarie, selv med fem vindmølle længders adskillelse.

2

Motivation

Many European governments have publicly announced plans to significantly increase the production of energy from renewable sources compared to that from conventional power plants in the next decades[1]. The Danish Government, for example, is committed to produce 50% of their domestic electricity needs from wind energy in 2030[2]. This will lead to a further increment in the wind energy contribution to the electricity grid here in Denmark. Currently this figure is at about 20%. The commitment made by the European governments is challenging in many respects. One example is the realisation of an electrical power grid, which should be capable of distributing large electrical currents over long distances and across countries. Furthermore, additional suitable areas for wind turbine installation have to be made accessible. This can become challenging as the total amount of installed turbines increases and the remaining available areas with good wind conditions are limited. Therefore, the option to develop wind farms offshore becomes more important.

The North Sea is expected to become in the near future a major area for wind energy production. Fig. 2.1 gives a clear overview of the extent of the planned wind farm sizes, depicted in red colours, compared to the already existing ones, depicted in green. Although technical and political challenges might slow down the ambitious targets, the long-term benefits of offshore wind energy are such that eventually it will become competitive. Compared to onshore winds, offshore winds are generally steadier, higher and less turbulent. This leads to a more constant, higher and more durable electricity production. Furthermore, the installation of wind turbines offshore is less sensitive to public opposition. According to BTM Consult, a part of Navigant consulting, the total installed offshore power for Europe was in 2013 around 4.8 GW, whereas already in 2017 it is expected to grow fivefold, to circa 24.5 GW. Denmark has planned to increase its offshore capacity from 830 MW to 1.83 GW by 2017.

The cost of offshore wind energy is currently higher than that of onshore wind energy. The offshore wind energy cost is among others a function of individual turbine spacing, their distance to the coast, water depth, seabed type and wind speed. For offshore exploitation of wind resources, wind turbines are grouped together to form so called wind farms. Currently there are 16 wind farms installed in the North Sea, with a nominal

[1] http://ec.europa.eu/energy/renewables/action_plan_en.htm
[2] http://www.kebmin.dk/sites/kebmin.dk/files/nyheder-presse/2030_green_paper_danish_response.pdf

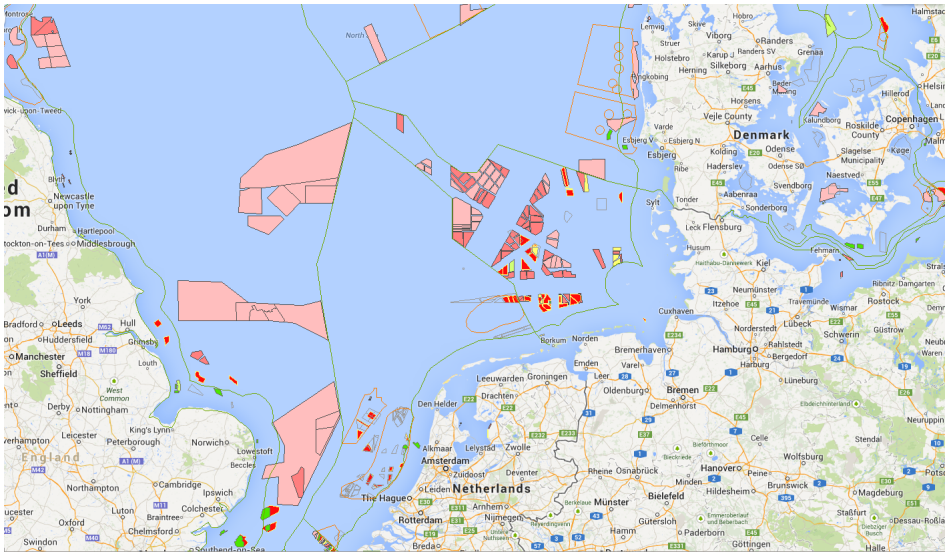
Denmark
Netherlands
England
Amsterdam
Rotterdam
The Hague
Hamburg
Bremen
Copenhagen
Kiel
Sheffield
Manchester
Leeds
Hull
Newcastle upon Tyne
Norwich
Cambridge
Ipswich
Peterborough
Nottingham
Derby
Leicester
Northampton
Oxford
Swindon
Luton
Chelmsford
Colchester
Braintree
Lowestoft
Beccles
King's Lynn
Louth
Grimsby
Huddersfield
Bradford
York
Durham
Hartlepool
Middlesbrough
Sunderland
Alkmaar
Leiden
Zuidoost
Deventer
Zwolle
Leeuwarden
Groningen
Drachten
Den Helder
Arnhem
Nijmegen
Breda
Münster
Osnabrück
Bielefeld
Hannover
Minden
Hildesheim
Peine
Brunswick
Wolfsburg
Magdeburg
Paderborn
Gütersloh
Hamm
Göttingen
Oldenburg
Delmenhorst
Bremerhaven
Cuxhaven
Norden
Emden
Leer
Varel
Harburg
Lüneburg
Celle
Stendal
Rostock
Lübeck
Neumünster
Itzehoe
Wismar
Schwerin
Flensburg
Sønderborg
Aabenraa
Haderslev
Kolding
Esbjerg
Odense
Aalborg
Aarhus
Randers
Viborg
Silkeborg
Horsens
Vejle
Roskilde
Helsingør
Hillerød
Slagelse
Næstved
Svendborg
Sylt
Husum
Tønder
Ribe
Skive
Holstebro
Herning
Struer
Lemvig
Hobro
Grenaa
Karup
Randers SV
Beder
Malmö
Halmstad
Varde
Esbjerg V
Esbjerg N
Kalundborg
Køge
Municipality
Naestved
Leck
Fehmarn
Travemünde
Ribnitz-Damgarten
Güstrow
Schwerin
Rahlstedt
Bergedorf
Celle
Wolfsburg
Stendal
Magdeburg
Staßfurt
Dessau-Roßlau
Halle
Detmold
Bielefeld
Hildesheim
Peine
Brunswick
Minden
Hannover
Osnabrück
Münster
Rheine
Enschede
Zwolle
Lelystad
Almere
Amsterdam
Zuidoost
Deventer
Apeldoorn
Arnhem
Nijmegen
Rotterdam
Breda
Eindhoven
Tilburg
Den Helder
Drachten
Leeuwarden
Groningen
Leer
Emden
Norden
Borkum
Cuxhaven
Bremerhaven
Oldenburg
Delmenhorst
Bremen
Harburg
Lüneburg
Hamburg
Norderstedt
Neumünster
Itzehoe
Wismar
Rostock
Lübeck
Schwerin
Flensburg
Sønderborg
Aabenraa
Haderslev
Kolding
Esbjerg
Odense
Aalborg
Aarhus
Randers
Viborg
Silkeborg
Horsens
Vejle
Roskilde
Copenhagen

regarding a changed upwelling that could be caused from the reduced surface velocities in the wind farm wake.

The atmospheric flow and its interaction with wind turbines can be analysed using measurements as well as models. One of the advantages of using models is their low cost, since simulations can be computed for different locations. A whole range of models have been developed. The first models to be used for estimating the impact of wind turbines to the downstream flow field, were the so called “engineering” models. Later-on, when computational power increased, Computational Fluid Dynamics (CFD) codes have been used to simulate the flow field around the turbine(s). Recently more advanced Large Eddy Simulation (LES) models have been adapted for the simulation of wind turbines and even wind farms. For larger scales, mesoscale models and even Global Circulation Models (GCM) have been utilised to simulate the interaction between wind farms and the atmosphere. The model choice is determined by the purpose of the investigation. Whereas CFD models allow the simulation of individual turbine wakes, models with a coarser resolution allow the simulation of larger scale flows with reasonable computational costs.

This thesis aims at improving the understanding of the mesoscale (1 - 20 km) flow field behaviour around wind farms. The findings can potentially be useful for wind speed assessment, the optimisation of wind farm designs and wind farm group separation. The thesis is structured as follows. In Chapter 3 we introduce briefly the characteristics of a turbine-induced wake and discuss the advantages and disadvantages of the various measurement and model techniques. In Chapter 4 we start by reviewing the existing literature in numerical wind farm modelling. Then the basic principles of mesoscale models are described, followed by an introduction of the different wind farm parametrisations. In Chapter 5 we evaluate the models against long-term measurements from the offshore wind farm Horns Rev I. The influence of a large hypothetical wind farm to the marine boundary layer, as well as the importance of the several mechanisms in the wind farm wake recovery process, are described in Chapter 6. Chapter 7 discusses possible applications of the introduced wind farm parametrisation approach and presents some preliminary results. In Chapter 8 the findings will be summarised and conclusions given.

3

Introduction into Wind Turbine Modeling

In this chapter some basic characteristics of the turbine-induced velocity reduction, or wake, are briefly explained. Thereafter, we introduce the measurement techniques and the most common models that are used to simulate the effects of the wind turbine to the surrounding velocity field.

3.1 Influence of Wind Turbines to the Atmosphere

A wind turbine converts kinetic energy of the wind into rotational energy and rotational energy into electricity. The blade forces cause a flow deceleration mainly in the flow direction. A precise description of an atmospheric turbine-induced wake is challenging due to the complexity of upstream flow conditions. A schematic diagram is presented in Fig. 3.1.

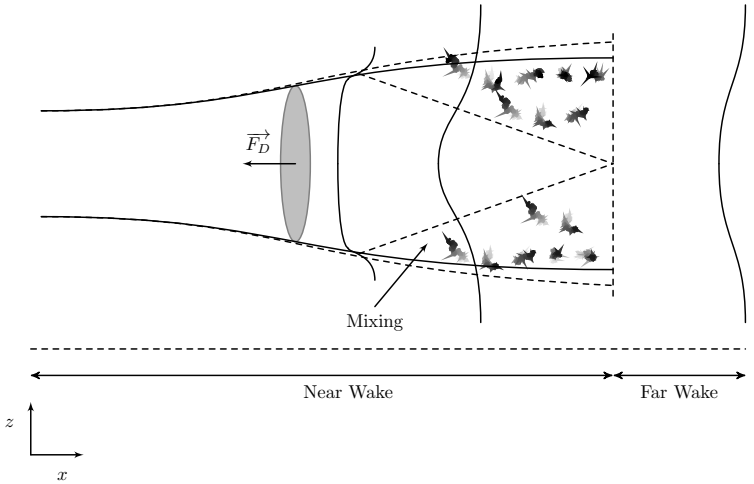

Figure 3.1: Schematic diagram of the flow field around the turbine in the stream-wise flow direction. The wind turbine is represented by the grey area. The drag force is indicated by F_D. The vertical direction is indicated by z and the horizontal direction by x.

Generally a wake can be divided into two regimes: the near and far wake. The near wake is determined by the turbine's blade aerodynamics and it is the region in which

tip vortices, caused by the pressure difference between the lower and upper blade side, can be found. This region extends around one turbine diameter downstream of the rotor (Vermeer et al., 2003), or more. After the turbine, large gradients between the turbine-induced wake and the environmental flow are found. Fig. 3.1 illustrates in a simplified way, the velocity field after a wind turbine. The turbulence shear mixes the high velocity from outside the wake with the wake's low velocity. Roughly at the end of the near wake the wake development is completely governed by turbulence shear mixing. Here also the pressure returns approximately to the background value. The far wake region can approximately be described by a Gaussian velocity deficit profile (Vermeer et al., 2003). Its expansion is characterised by a turbulent diffusion process that occurs between the velocity deficit region and the environmental flow. The analysis of the turbine-induced flow varies over a range of scales. At small scales the effect of the turbine blade geometry to the flow can be studied. Whereas, on large scales in the order of the far wake, the effects of the upstream to the downstream turbine, often referred to as turbine interaction, can be investigated. At even larger scales, the interaction between individual wind farms and the influence on the local atmosphere can be examined. Finally, on a global scale the impact of large wind farm clusters to the non-local environment can be investigated. For every step up in the model cascade, the turbine description in the model becomes less detailed. It is therefore necessary to estimate the importance of the details at the smaller scales.

3.2 Wind Turbine Wake Measurements

Experimental data and measurements are necessary for the optimisation (calibration) and evaluation of numerical models. Their acquisition, for wind energy analysis, is mainly obtained from atmospheric wind measurements and wind tunnel experiments.

Anemometers are used to measure the wind speed at a given position. The turbine's power production is to a good approximation obtained from the hub-height wind speed. For modern turbines this is between 70 m and 120 m. To install the necessary equipment on meteorological masts for the considered height is expensive and the costs increase further for remote places or open seas. Consequently, carefully performed, openly accessible measurements are rare.

Within the wind farm, measurements can be obtained from the Supervisory Control And Data Acquisition (SCADA) system. The SCADA database provides for every individual turbine, the power generated, yaw position, rotor speed, nacelle wind speed, etc. The data processing of those signals is however difficult. The SCADA data from the Danish offshore wind farm Horns Rev I has been extensively analysed in recent years. A complete description of the data can be found in Hansen (2012, 2013). Horns Rev I

is one of the first large wind farms and became operational in 2002. The study of its velocity field is very useful due to the wind farm's regular layout. It has been used for the evaluation of "engineering" and high resolution models. Since met masts and turbines provide one point measurements, a comparison with the flow field from mesoscale models is more challenging, due to the fact that the mesoscale model's output represents an area average.

Because of the increasing turbine and wind farm sizes, remote sensing measurement methods are becoming increasingly convenient compared to mast measurements. Wake measurements are recently performed with satellites (Christiansen and Hasager, 2005), Doppler wind light detecting and ranging (LIDAR) instruments (Iungo et al., 2012) and mobile radio detection and ranging (RADAR) devices (Hirst et al., 2012). One disadvantage of remote sensing data is the relative high amount of post-processing needed to obtain usable data. However, the main advantage of remote sensing is that flow fields over large areas can be obtained and that the devices are more mobile and easily relocatable.

On the other hand, numerous experiments in small wind tunnels have been performed to investigate e.g. turbine interaction (Ross and Ainslie, 1981), the effect of roughness on the turbine-induced wake (Chamorro and Porté-Agel, 2009) and the influence of thermal stability on the wake recovery (Chamorro and Porté-Agel, 2010; Zhang et al., 2013). The drawback of these measurements are the low Reynolds number flows, which act differently on the blades compared to the atmospheric flow. Experiments with high Reynolds numbers in large wind tunnels are more expensive. One example is the MEXICO (Model Experiments in Controlled Conditions) project, financed by the European Union. It has been performed in the large German-Dutch Wind tunnel (DNW) (Snel et al., 2007). This experiment has been used for the evaluation of CFD models (Réthoré et al., 2011).

3.3 Wind Turbine Wake Modeling

From the early 1980's onwards the recovery of turbine-induced wake recovery has been extensively studied. In the early "engineering" approaches the turbine wake is transported downstream considering only the conservation of mass. In those models the background is not considered. An often used model is the PARK wake model (Katic et al., 1986), based on the Jensen model (Jensen, 1983). The PARK model is used in the Wind Atlas Analysis and Application Program (WA^{s}P) (Mortensen et al., 2007). The disadvantage of this simple approach, is that no interaction between the wake and the environmental flow is considered. However, the models are computationally inexpensive and have shown to fit measurements fairly well (Peña et al., 2013). In the past years the very fast linearised wake model FUGA has been developed (Ott et al., 2011). This model solves the linearised Reynolds Averaged Navier-Stokes (RANS) equation and is

several orders of magnitudes faster than conventional high resolution models. Evaluated against the Horns Rev I and Lillegrund wind farm, it has been shown to produce very good results (Gaumond et al., 2012).

Additionally, (Frandsen, 2007), proposed the representation of the effects of a wind farm with a changed roughness element. In this approach a thrust dependent wind farm roughness is applied to the turbine hub-height. Peña and Rathmann (2013) extended the model, by including atmospheric stability in the formulation. This model is planned to be evaluated against wind farm data in the near future.

3.3.1 High Resolution Models

In recent years, since computational costs have been significantly reduced, applications of high resolution models for the simulation of wind turbine wakes have become more widespread. Here two types of models can be distinguished: CFD and LES models. The CFD models resolve generally the steady RANS equation, where the turbulence part of the spectrum remains completely unresolved. The LES models resolves unsteady flows up to the filter frequency within the inertial part of the energy spectrum, the remaining unresolved part of the spectrum is described by a sub-grid-scale model. Due to the fine grid-size of both models a wind turbine is represented by a local drag force only. The model accounts afterwards for the downstream flow development. There are general three methods to describe the turbine-induced drag force. The simplest way is to consider the wind turbine as an irrotational actuator disc. At each grid-cell within the actuator disc, a drag force is applied in the opposite direction to the flow. This can be done since the forces in the flow direction are normally an order of magnitude higher than the rotational forces, see Réthoré et al. (2013, Fig.(16)). More advanced approaches take into account the turbine's disc rotation (rotational actuator disc), or apply forces in all three directions to rotating blades (actuator line). From LES simulations it has been shown that all three approaches converge in the far wake (Porté-Agel et al., 2011).

The main advantage of CFD models are the lower computational costs. However, most often steady, neutral conditions are assumed. Furthermore, they often use a simple linear turbulence closure, which has been shown to be too diffusive and consequently with too fast wake recovery (Réthoré et al., 2009). On the other hand, the computational costs involved in LES simulations are about three orders of magnitude higher than those in CFD RANS. However, their results are generally reliable and often used as a reference. Recently Chamorro and Porté-Agel (2009) and Porté-Agel et al. (2011) have shown that their LES model performed well against measurements and wind tunnel data. Due to increasing computational capacity it is already possible to simulate the flow of complete wind farms with LES models (Wu and Porté-Agel, 2012).

3.3.2 Mesoscale Models

Mesoscale models use the complete prognostic RANS equations to simulate the atmospheric flow. Their domain size is typically in the order of 100 to 1000 km. To reduce computational costs, a relatively low horizontal resolution is often utilised, usually between 2 and 20 km. Processes smaller than the horizontal resolution are unresolved and have to be parametrised. The effect of the wind turbines are also part of these processes, since the wind turbine wake, with a horizontal size similar to the blade diameter, is several times smaller than the horizontal grid-size Δx, which is in the order of km's.

In the past, several wind farm approaches have been developed. The most straightforward approach is to approximate a wind farm by a changed surface roughness element. In a mesoscale model the roughness information is only used within the first model layer, where the velocity profile is often described by the Monin-Obukhov similarity theory. Above this layer the flow is prognosed by the model. An example of wind farm simulations with mesoscale models is given in Frandsen et al. (2009). The authors studied the local near wind farm wake effects by applying an increased roughness (in different spatial configurations) to a mesoscale model. They found that for a large wind farm, that covered an area of 900 km^2, the velocity deficit at the turbine hub-height reached an asymptotic minimum within the wind farm. It took around 60 km downstream for the wind farm wake to recover to the background wind speed.

A more advanced approach compared to the changed roughness approach, is to simulate wind turbines as a drag force. In this way one can account for 1) a more accurate estimate of energy extracted by a wind turbine as a function of wind speed and 2) a more realistic vertical wake distribution. Roy et al. (2004), Roy and Traiteur (2010), and Roy (2011) studied the near-surface impact of onshore wind farms. They assumed wind turbines to be a sink for the kinetic energy (KE) and a source for turbulence kinetic energy (TKE). Based on upstream and downstream measurements, they derived expressions for the TKE source and the velocity. The velocity measurements were performed at hub-height. Roy and Traiteur (2010), for example, simulated a 41 turbines containing wind farm near to Palm Springs, CA. The installed turbines were 28 m tall and had a blade diameter of 17 m. The implemented model wind farm contained 21 turbines, with a hub-height at 100 m and 100 m blade diameters. The observations showed, during a two months measurement campaign in summer 1989, significant cooling at 5 m above the ground for most of the day (up to 3 K cooling) and a statistical less significant warming during the night, between a upstream and downstream station. The model temperature difference was obtained by subtracting the average temperature within the wind farm from the average temperature for the same grid-cells, without wind farm. The model results confirmed the observed wind farm-induced surface cooling during the day and surface heating during the night, in the wake of the wind farm. However, the cooling was less pronounced (up to 0.3 K cooling) and during the night up to 1 K heating.

Adams and Keith (2013) used the drag parametrisation from Adams and Keith (2007), to study the power production sensitivity as a function of the wind farm size and turbine density. In this approach, a conventional drag force is applied to the RANS equations and an additional source term to the TKE equation. The additional term turbulence term is $\propto C_e|U|^3$, where the constant C_e is $C_T - C_P$ and $|U|$ the absolute velocity. In this parametrisation the thrust coefficient, C_T and power coefficient, C_P are obtained from turbine specific thrust and power curves. The mechanical losses are neglected in this approach. Their simulations suggest that the amount of production is limited to around $1\,\mathrm{W\,m^{-2}}$. In Chapter 7 this finding is analysed further. Blahak et al. (2010) proposed a drag approach, very similar to that used in Adams and Keith (2007). This approach accounts for mechanical losses and uses wind speed independent relationship between the thrust and power coefficient. The Weather Research and Forecast (WRF) model (Skamarock et al., 2008) added in their V3.2 release a wind farm parametrisation, hereafter referred to as WRF-WF (Fitch et al., 2012). This scheme assumes a wind speed independent relationship between the thrust and power coefficient. In this scheme the mechanical losses are neglected. Later, Fitch et al. (2013) studied with the same approach the quantitative impact of a large wind farm to the near surface variables. Their findings were similar to those in Roy and Traiteur (2010).

3.3.3 Global Circulation Models

Global Circulation Models (GCM) solve the same set of equations as mesoscale models. However, since the simulations are performed over the entire globe, the grid-spacing ranges generally from around 100 to above 200 km. Due to the very coarse grid spacing, these models are hydrostatic, incompressible and have simple turbulence closures. The vertical resolution is also coarser given a boundary layer flow that is simulated more poorly. To account for the atmosphere-ocean interaction they are often coupled with ocean models. GCMs have also been used to study the climate impact of large wind farms to the atmosphere. Due to their coarse resolution it is more customary to simulate wind farms with a changed roughness length, since the lowest model level is mostly above the upper turbine blade tip. Examples are Kirk-Davidoff and Keith (2008), Barrie and Kirk-Davidoff (2010) and Wang and Prinn (2010).

Barrie and Kirk-Davidoff (2010) studied the impact of a very large wind farm to the atmosphere. The hypothetical wind farm, that covered around 23% of the North American continent, was represented by a changed roughness length approach proposed by Lettau (1969), $z_0 = 0.86$ m, where z_0 is the roughness length. They found that at the first model level, 170 m above the surface, the largest velocity anomalies occurred within the wind farm. The model simulated, furthermore, positive velocities due to the dynamical adjustment which extended from southern Greenland up-to the West coast of Europe.

Wang and Prinn (2010) investigated with a fully coupled atmosphere-ocean model, the long term impact of very large wind farms, represented by an increased roughness over all land surfaces covered by grass and shrub. They performed four simulations with different roughness and displacement heights. For the simulation with a roughness length of 2.62 m and a displacement height of 23.45 m they found a horizontally averaged positive temperature bias of around 0.7 K on the ground. Furthermore, enhanced large scale precipitation was found in mid-latitude regions. Marvel et al. (2013) estimated with a GCM the upper limit of available wind energy, by adding a drag term only to the surface layer and to the whole atmosphere. They found the total amount of available energy for ordinary wind turbines placed on the surface to be above 400 TW.

4

Wind Turbine simulation with Mesoscale Models

We will use throughout this thesis the open source WRF model. As briefly mentioned in Chapter 3, it includes a wind farm parametrisation, which is very similar to those presented in Adams and Keith (2007) and Blahak et al. (2010). This allows us to focus our analysis on a comparison between four different approaches. First, the wind farm is represented simply by a changed roughness length. Then, we investigate the differences between a drag formulation without additional turbulence, hereafter referred to as ROTOR-DRAG approach and the WRF-WF scheme. Finally, a new approach is introduced and analysed. It will be referred to as Explicit Wake Parametrisation (EWP). In the next paragraph we introduce the fundamental mesoscale model equations which will be used later on in the different approaches.

4.1 Mesoscale Models

In this section the basic mesoscale model equations and notation that are used throughout the thesis are introduced. Mesoscale models have been developed to simulate weather phenomena in a wide range of scales, from large scale synoptic systems that extend over areas of several hundreds of kilometres to phenomena that occur at scales in the order of tens of kilometres, such as sea-breezes. To limit computational costs a relatively course horizontal resolution is used. Whereas, the vertical resolution, in the turbulent part of the atmosphere, can be in the order of decametres. For this study we use the non-hydrostatic and fully compressible WRF model. It includes prognostic equations for the velocity components, (potential) temperature and water vapour, cloud water, rain, cloud ice etc.. Furthermore, equations for the geopotential and the conservation of mass per column are solved. The equation of state is used to close the system.

In the main part of the thesis a wind turbine is described as a drag device, which is an additional forcing term to Newton's second law of motion. The ensemble Averaged Navier Stokes (RANS) equation, without viscosity term reads

$$\frac{\partial U_i}{\partial t} + U_j \frac{\partial U_i}{\partial x_j} + \frac{\partial \overline{u_i u_3}}{\partial x_3} = -\frac{1}{\rho}\frac{\partial P}{\partial x_i} - 2\varepsilon_{i3k} f U_k - \delta_{i3} g + F_{D_i}. \tag{4.1}$$

The upper-case letters in Eq. (4.1) represent the Reynolds averaged quantities and the

lower-case letters indicate the perturbation of the mean quantity. The mean velocity components are denoted by $U_i(\mathbf{x},t)$, the mean pressure by $P(\mathbf{x},t)$ and the mean turbine induced drag by $F_D(\mathbf{x},t)$. Furthermore, $\rho(\mathbf{x},t)$ stands for the density, f for the Coriolis parameter and g for the gravity acceleration. The index $i = 1,2$ and 3 represents the directions x, y and z. The Kronecker delta is denoted by δ_{ij} and the Levi-Civita symbol by ε_{ijk}. The second term on the left hand side is the resolved transport of momentum and the third term the divergence of the Reynolds stress. The right hand side of Eq. (4.1) contains all forcing terms: the pressure gradient force, Coriolis force and acceleration due to gravity, as well as the turbine-induced forcing.

Throughout the thesis a 1.5 order (Level 2.5) closure scheme is used to model the turbulent fluxes, such as the Reynolds stresses in Eq. (4.1). Assuming the turbulent mixing process to be local, the dominating components of the Reynolds stress become

$$\overline{u_i u_j} = -K_m \frac{\partial}{\partial x_j} U_i. \tag{4.2}$$

Here $K_m = q\ell S_m$ is the turbulence diffusion coefficient for momentum, where $q(\mathbf{x},t)$ stands for the turbulence velocity, $\ell(\mathbf{x},t)$ for the turbulence mixing length and $S_m(\mathbf{x},t)$ for the momentum stability correction. The turbulence velocity, q, is defined as the square root of twice the turbulence kinetic energy, $q = \sqrt{2e}$. Furthermore, the index i represents the x and y direction. The formulation for the turbulence mixing length and stability function depends on the boundary layer scheme. We will use exclusively the MYNN boundary layer scheme (Nakanishi and Niino, 2009). In this scheme the turbulence mixing length is defined as

$$\frac{1}{\ell} = \frac{1}{\ell_s} + \frac{1}{\ell_t} + \frac{1}{\ell_b},$$

where ℓ_s, ℓ_t and ℓ_b are the buoyancy, turbulence and surface length scales (Nakanishi and Niino, 2009). In a Level 2.5 closure, a prognostic equation for $e(\mathbf{x},t)$ is solved. It reads

$$\frac{\partial e}{\partial t} + \frac{\partial}{\partial x_j}\left(U_j e + \frac{1}{2}\overline{u_l u_l u_j} + \overline{p u_j}\right) = \frac{g}{\Theta}\overline{u_3\theta} - \overline{u_l u_j}\frac{\partial U_l}{\partial x_j} - \varepsilon + \overline{u_i f_{D_i}}, \tag{4.3}$$

where Θ and θ are the mean and fluctuating part of the potential temperature. The second term in Eq. (4.3) includes the advection and turbulent transport of e, as well as the divergence of the pressure correlation. The right hand side contains all production/destruction terms, the buoyancy production/destruction, shear production and dissipation. The additional turbine-induced term $\overline{u_i f_{D_i}}$, where f_{D_i} indicates the turbine drag perturbation, is obtained from the Reynolds decomposition of the turbine drag force in Eq. (4.1).

4.2 Wind Turbine Parametrizations - A review

We evaluate the roughness length (RL) change and the ROTOR-DRAG approach against measurements from Horns Rev I. The WRF-WF as well as the EWP approach are validated more extensively in Chapter 5. In that chapter a complete description of the measurements and model configuration can be found, see Sect. 5.1.3 and Sect. 5.1.4. For completeness a summary is given here.

The Horns Rev I wind farm contains 80 wind turbine with a rated capacity of 2 MW. The turbine's blade diameter is 80 m and the hub is mounted at 70 m above mean sea-level. Because of the geometry we analysed the wind farm wake flow for the westerly wind direction. In this wind direction the wind farm has an approximately rectangular shape. It contains 10 columns, with 8 turbines in each column, see Fig. 4.1.

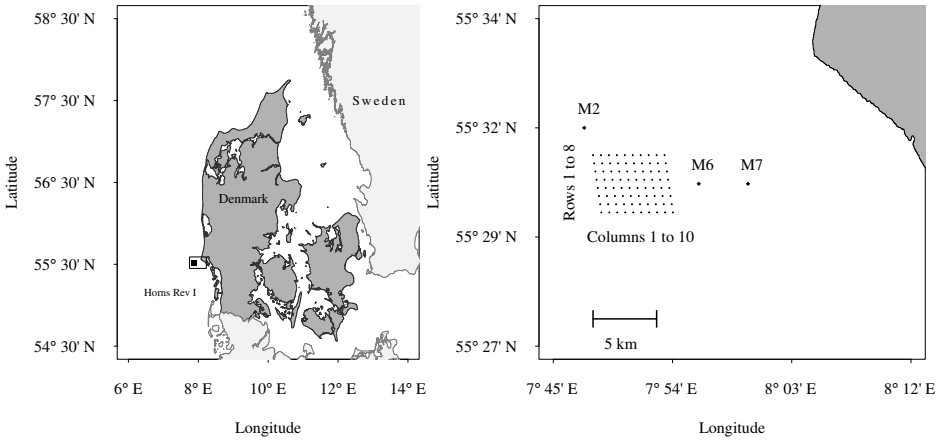

Figure 4.1: Left side: Map of Denmark. The location of the Horns Rev I is indicated with rectangle. Right side: Sketch of the single turbine and the met masts, indicated with dots and diamonds, respectively.

For the evaluation the most northern and southern row are excluded, since these rows experience different flow conditions. From the remaining turbines a hub-height wind speed is derived from the power production. The column wind speed is obtained by averaging over all rows. Additional to the turbine measurements, two met masts, M6 and M7, to the East of the wind farm provide wind farm wake wind speeds at 70 m height. For the comparison with the mesoscale model, wind speeds between 7.5 m s^{-1}and 8.5 m s^{-1}, within a wind direction interval of $255° \leq \phi \leq 285°$, are selected (Hansen, 2013). The selection criteria are shown in Table 4.1.

Table 4.1: Summary of measurement selection

Period (Year):	$2005 - 2009$
Wind directions $(^\circ)$:	$255 - 285$
Up-stream wind speed $\left(ms^{-1}\right)$:	$7.5 - 8.5$

The WRF model is set-up in a so called idealised case mode. The model is initialised with a homogeneous, dry atmosphere over the entire domain. The lateral boundaries are open, which implies that no forcing from these boundaries takes place. Furthermore, the surface heat flux was set to zero. In this way the model converges towards neutral conditions, with a turning wind speed in height, caused by the Coriolis force. In this study we ran the WRF model with three different vertical resolutions. The experiments contain 28, 40 and 80 vertical layers and are hereafter referred to as L28, L40 and L80 simulation. They contain 3, 5 and 11 layers within the turbine rotor area. The horizontal grid-spacing was in all simulations set to $\Delta x = 1120\,\mathrm{m}$. The model wind farm contains in all simulations 5 grid-cells in the West-East direction and 5 grid-cells in the North-South direction, see Fig. 4.2.

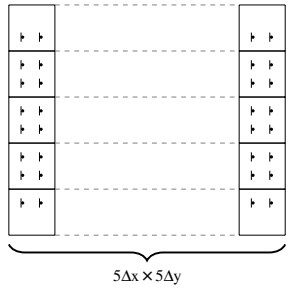

Figure 4.2: A sketch of the wind farm layout, as defined in the model. The number of turbines are indicated within the 25 model grid-cells.

The turbine density is 2 turbines per grid-cell in the most northern and southern rows, while in the 3 central rows it is 4 turbines per grid-cell. Similar to the measurements, the outer rows were excluded from the model analysis. The wind field wake evolution within the wind farm is evaluated for the central rows. The mesoscale model was forced with hub-heights wind speeds in the directions between 258.75° and 281.25° with a 3.75° interval. The absolute velocity at hub-height is for these simulations, $U_0 = 8 \pm 0.03\ \mathrm{m\,s^{-1}}$. The wind speed variation results from the various simulations in wind direction and vertical resolution. The model set-up is shown in Table 4.2.

Table 4.2: WRF set-up

Wind directions (°):	258.75/262.5/266.25/270/273.75/277.5/281.25
U_0 (ms^{-1})	8
Grid-points (nx,ny):	80, 30
Domain extension x, y (km, km):	89.6, 33.6
Grid-points (nz):	28, 40, 80
Horizontal grid spacing (m):	1120
Wind farm extension (nx × ny):	5 × 5
Boundary condition:	OPEN
PBL scheme:	MYNN (1.5)

4.2.1 Roughness Length Change

In the first simulation the wind farm was modelled as an area with an increased roughness length. The increased roughness length reduces the velocity within the wind farm, analogously to what occurs in a real wind farm. For our experiments we used the Frandsen equation from the infinite wind farm (Frandsen, 2007, Eq.(A.2.10)) to determine the roughness length of the wind farm, namely:

$$z_{0_{WF}} = z_h \exp\left[-\frac{\kappa}{\sqrt{c_T + \left[\frac{k}{\ln(h/z_0)}\right]^2}}\right]. \tag{4.4}$$

In Eq. (4.4), h denotes the turbine hub-height, κ the Von Kármán constant, z_0 the surface roughness length of the background sea-surface and c_T the normalised thrust coefficient. The normalised thrust coefficient is $c_T = \pi C_T / (8 D_x D_y)$, where $D_x = x_c/D_0$ and $D_y = y_c/D_0$ are the normalised turbine spacings in the x and y direction, D_0 the turbine diameter and C_T the turbine thrust coefficient. We use throughout the thesis a Von Kármán constant, $\kappa = 0.4$ and for the idealised case studies a constant sea-surface roughness length, $z_0 = 2 \cdot 10^{-4}$ m. At Horns Rev I, the turbine's hub-height is $h = 70$ m, the turbine diameter $D_0 = 80$ m and the turbine spacing is 560 m in the North-South, as well as in the West-East directions. The thrust coefficient is $C_T = 0.81$ for a wind speed of $8\,\mathrm{m\,s^{-1}}$. Using these values in Eq. (4.4), we obtain for the wind farm roughness length, $z_{0_{WF}} = 0.7$ m. The used values are summarised in Table 4.3.

This value is in-line with the roughness length $z_{0_{WF}} = 0.5$ m used in Frandsen et al. (2009) for the simulation of a turbine hub-height at 50 m. Wu and Porté-Agel (2012) estimated from LES wind farm simulations the roughness length with a logarithmic extrapolation from the cross-stream averaged upper wake (from hub-height upwards) to the surface. The authors found that the roughness length was higher than that of all consid-

Table 4.3: Table with the values used for the Roughness length change.

Variable	$U_0\,(\mathrm{m\,s^{-1}})$	C_T	$D_0\,(\mathrm{m})$	$z_0\,(\mathrm{m})$	$z_{0_{\mathrm{WF}}}$
Value	8	0.81	80	$2{\cdot}10^{-4}$	0.7

ered analytical models (Lettau, 1969), (Frandsen et al., 2009) and (Calaf et al., 2010).

In Fig. 4.3 the normalised velocity at hub-height is shown, U_h/U_{0_h}, where U_h is the hub-height velocity within and in the wake of the wind farm and U_{0_h} the upstream hub-height velocity. The measured upstream velocity is defined, as that of the wind farm's first column, since no quality measurements from the upstream mast were present. In the model we use the wind speed of the reference run. It is expected that the velocity field of the first turbine column is already influence, due to an increased pressure. However, we assume the effect to be relatively small for the considered wind farm size. The simulated hub-height velocities are obtained by averaging over all wind directions. Furthermore, we average within the wind farm over the inner three wind farm grid-cells and consider further downstream in the wind farm wake, the central grid-cell only.

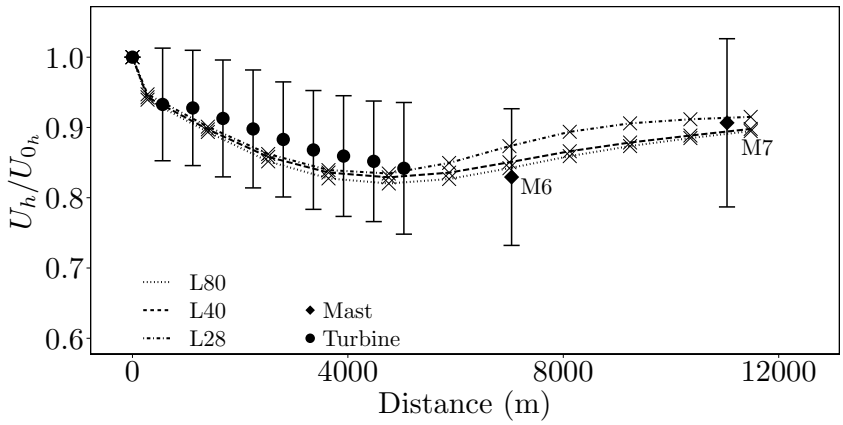

Figure 4.3: The normalised velocity, U_h/U_{0_h}, as a function of the downstream distance for the Roughness Length approach for the L28, L40 and L80 simulations. The crosses indicate the grid-cell centre. The dots represent the long-term averaged normalised turbine power measurements and the diamonds the normalised met mast measurements from M6 and M7 at 70 m height. The bars indicate the standard deviations of the measurements.

The simulated velocities are well within the standard deviations of the measurements. However, we notice that the hub-height velocity reduction, $1 - U_h/U_{0_h}$, increases with an increase in the resolution. Especially the velocity reduction in the L28 simulation is

smaller than that obtained in the other simulations. In Fig. 4.4 we plot the downstream normalised velocity at hub-height for the simulation with a 270° wind direction. The

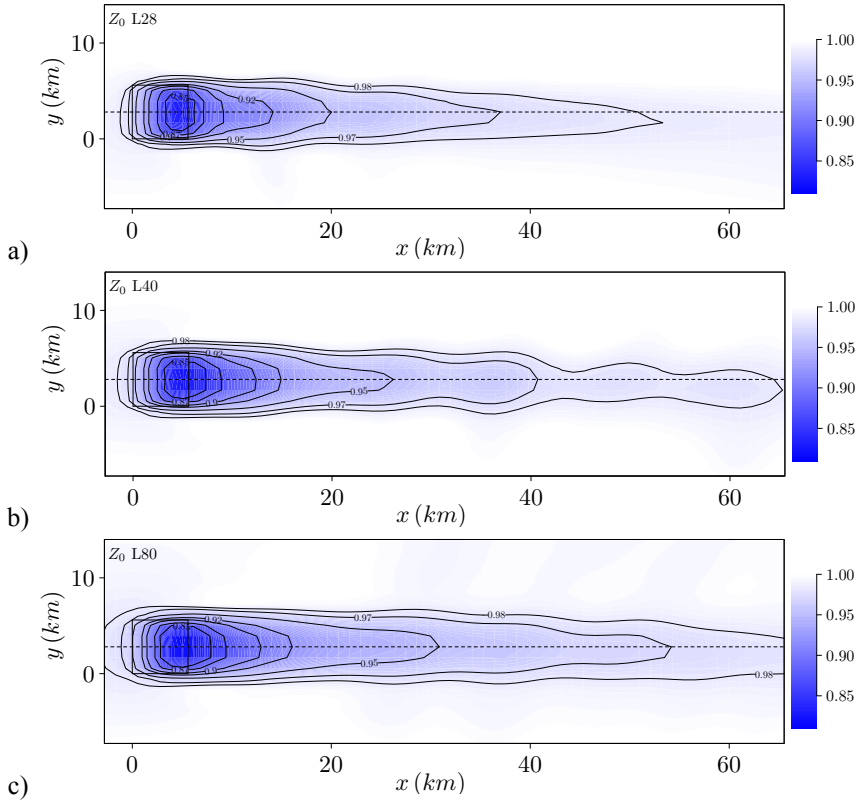

Figure 4.4: Normalised velocity, U_h/U_{0_h}, of the Roughness Length approach for the: a) L28, b) L40 and c) L80 simulation. The dashed line passes through the wind farm centre. The model wind farm is indicated by the square.

wake extension increases with the resolution, where the wake extension for a 5% velocity reduction is around 15 km, 20 km and 25 km for the L28, L40 and L80 simulation, respectively. The velocity deficit axis deviates to the right. The action of the Coriolis force on the reduced wind speed would result in a wind speed deviation to the left.

Figure 4.5a shows the normalised velocity deficit as a function of the normalised height according to the hub-height for the L40 and L80 run. The velocity profiles for the second (C2) and third (C3) wind farm containing grid-cell, as well as for the second grid-cell after the wind farm (C7) have been selected. The normalised velocity is de-

fined as $\Delta U / U_{0_h}$. Here the velocity deficit is $\Delta U = U(z) - U_{\text{up}}(z)$, with $U(z)$ being the velocity of the considered grid-cell and $U_{\text{up}}(z)$ the unperturbed velocity. The height is normalised against the turbine hub-height, z_h. Figure 4.5b shows the normalised velocity profiles from the unperturbed flow and those within and in the wake of the wind farm. The profiles, shown in Fig. 4.5a and Fig. 4.5b, are from the 270° simulation. Fig. 4.5a,

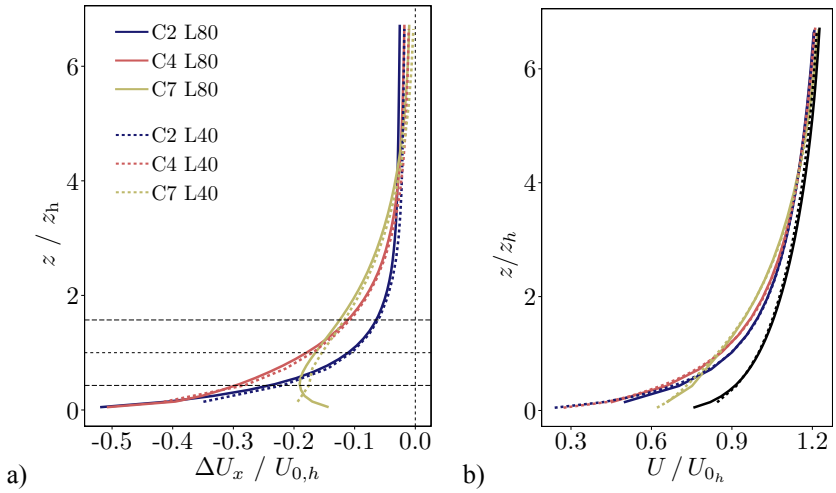

Figure 4.5: a) Normalised velocity deficit of the roughness length approach for the second (C2) and third (C3) wind farm grid-cell and at the second grid-cell (C7) after the wind farm. The velocity profiles from the L40 simulation are indicated with dashed lines and those ones from the L80 simulation with solid lines. The turbine blade top and bottom are represented by the top and bottom horizontal lines and the hub-height by the horizontal central line. b) Horizontal velocity profile for the same grid-cells as in Fig. 4.5a. The dashed and solid lines are from the L40 and L80 simulation, respectively. The black line represents the simulated normalised upstream wind profile.

shows that within the wind farm the maximum velocity deficit is for the L40 and L80 simulation at the lowest model level. At the second downstream grid-cell the maximum velocity deficit starts, at least in the L80 simulation, to develop upwards. In the lower resolution run, however, this process seems to occur with a delay. The velocity deficit profiles as shown in Fig. 4.5a do not agree with the profiles simulated by LES models (Porté-Agel et al., 2011) or those measured (Vermeer et al., 2003), which show approximately symmetric features around hub-height.

It can be concluded that regarding the velocity field the RL approach produces in first approximation good results at hub-height. However, the vertical structure of the velocity field does not agree with the measurements (Vermeer et al., 2003). The differences in the velocity profile will lead to different turbulence shear production. A good

estimation of turbulence is important, since it transports momentum from aloft into the wind farm induced velocity deficit region. In the RL approach we find within the wind farm an enhanced shear from the lowest model level up to the height of the wind farm induced internal boundary layer, whereas the measured far wake velocity profiles show a reduced shear below and an enhanced shear above hub-height (Vermeer et al., 2003). The difference in shear production will lead to a different surface interaction, as well as to a different wake recovery. An additional challenge is the estimation of the roughness length with an analytic approach (Wu and Porté-Agel, 2012). To overcome these shortcomings, we parametrise wind turbines in the next section as drag devices.

4.2.2 Rotor Drag Approach

Wind turbines are designed to convert kinetic energy into electrical power. The energy extracted by the turbine will manifest itself in a reduced velocity in the turbine's wake. The amount of velocity reduction can be in good approximation explained by the thrust forces acting in the horizontal flow direction only.

In the following, we attempt to achieve a better understanding of the importance of the unresolved turbine-induced wake development. In a first attempt a single turbine will be treated as an actuator disc, similar to that used in LES and CFD simulations. In Fig. 4.6 the schematic representation of a wind turbine is given.

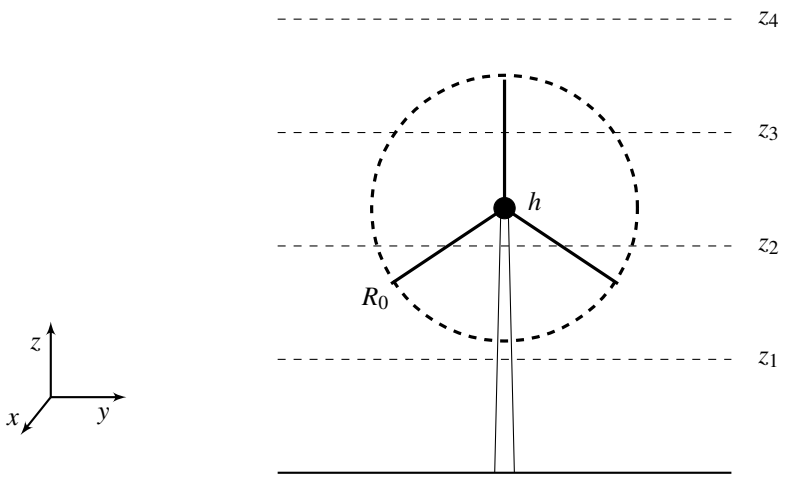

Figure 4.6: Schematic representation of the lower atmosphere where the wind turbine is located. The turbine blade sweep area with radius R_0 is indicated by the dashed circle. The turbine hub-height is represented by h. The model layers are represented by the horizontal dashed lines.

In Fig. 4.6 the vertical model levels are indicated by horizontal dashed lines and the border of the turbine's blade sweep area, $A_0 = \pi R_0$, where R_0 is the turbine rotor radius, is marked by the dashed circle. In this approach a drag force is applied to every turbine blade intersecting model (mass) level z_i, this will be referred to as the ROTOR-DRAG approach. The total force per mass applied by N turbines within a grid-cell reads

$$F_{D_i}(k) = -\frac{C_T\, N A(k)\, U_i(k)\, |U(k)|}{2\,(\Delta x)^2\, \Delta z(k)}. \tag{4.5}$$

Where $A(k)$ is the turbine blade area intersecting with the model level k, $|U(k)|$ the absolute horizontal velocity at level k, $U_i(k)$ the horizontal velocity in the direction $i = x, y$ and Δx, Δz the horizontal and vertical model grid spacing. In this method Eq. (4.5) is applied to Eq. (4.1) in every turbine blade containing grid-cell.

For the analysis of this approach, the same model configuration is used as for the RL method, see Sect. 4.2. The Vestas V80 thrust curve is used to determine the thrust coefficient. The wind farm contains again 5 grid-cells in the West-East direction and also 5 grid-cells in the North-South direction. The turbine per grid cell density N is 4 for the 3 inner grid-cells and 2 in the most northern and southern grid-cell. Fig. 4.7 is the analogue to Fig. 4.3 for the ROTOR-DRAG approach.

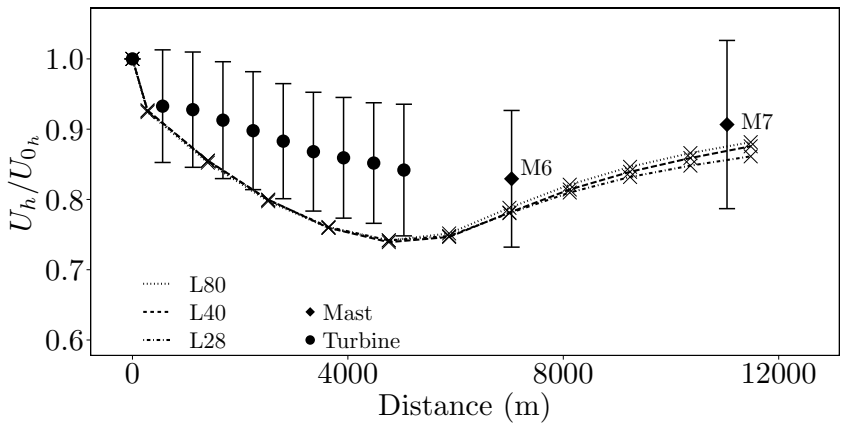

Figure 4.7: Normalised Velocity plot similar to Fig. 4.3, but for the ROTOR-DRAG approach.

The modelled velocity reduction at the end of the wind farm (5000 m) is lower than that measured. It is even outside the standard deviation of the measurements. After the wind farm the velocity recovers fast and at mast M7 it almost fits the measurements. This approach is vertical resolution independent for the various resolutions within the wind farm, however, in the wind farm's wake the solutions diverge.

In Fig. 4.8 we show the normalised velocity at hub-height for the 270° run. The wake

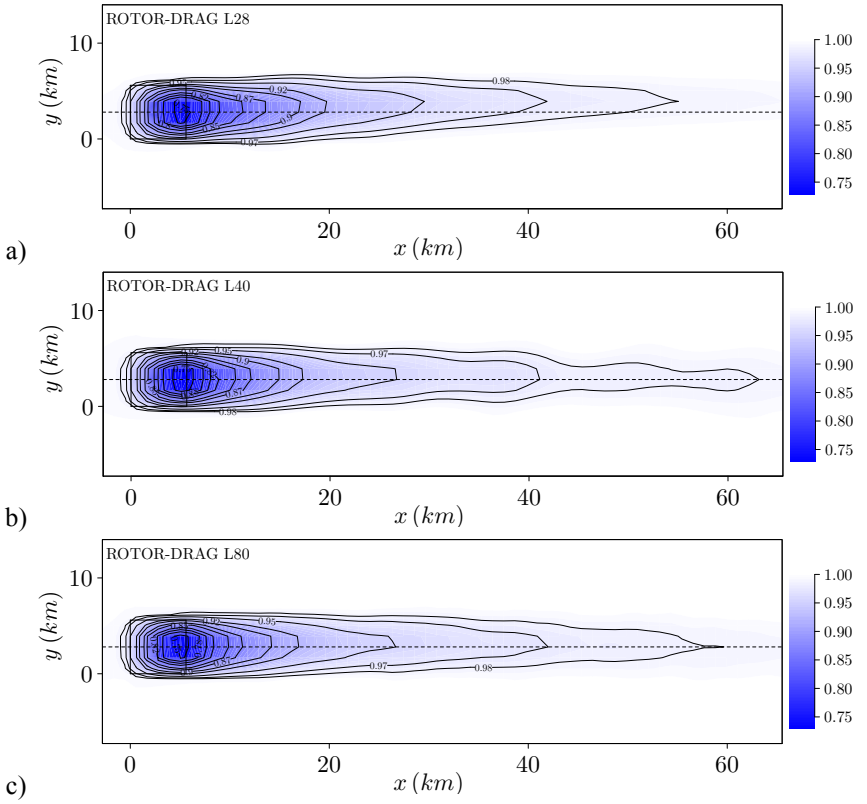

Figure 4.8: Normalised velocity at hub-height of the ROTOR-DRAG approach for the: a) L28, b) L40 and c) L80 simulation. The model wind farm is indicated by the square. The plots show the normalised velocities for the 270° wind direction only.

extension with a 5% velocity reduction is almost resolution independent. The wake extension is more then 20 km. Furthermore, we notice that the wind farm wake deviates the to left in the downstream direction. This is expected due to the reduced Coriolis force, acting on the decelerated flow. The wake extension with a 2% velocity reduction is comparable to the one in the roughness length change approach.

In Fig. 4.9a and Fig. 4.9b the normalised velocity deficit and the normalised velocity as a function of the normalised height are shown. The velocity deficit is distributed almost symmetrically around the hub-height. However, the maximum velocity deficit is within the wind farm above hub-height. We notice, furthermore, that the velocity deficit

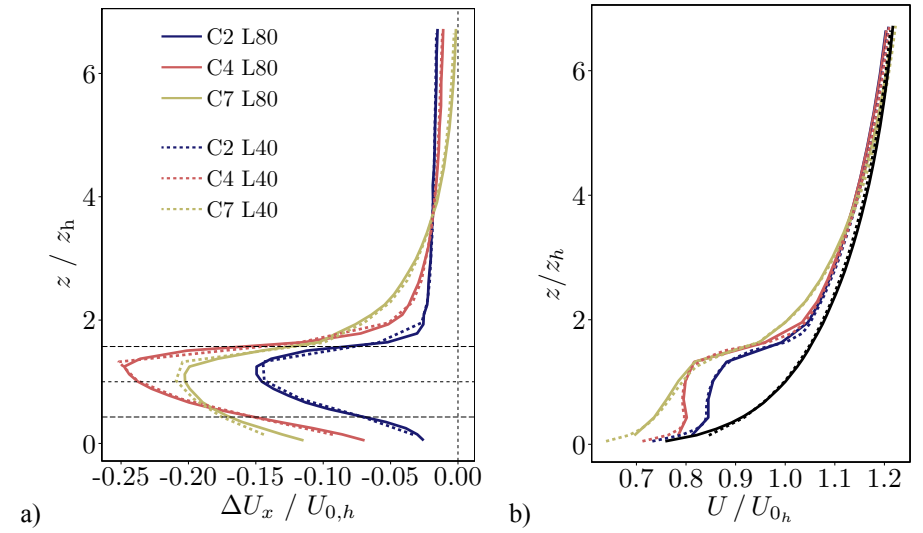

Figure 4.9: This figure is analogous to Fig. 4.5a and Fig. 4.5b, this time for the ROTOR-DRAG approach.

within the wind farm is concentrated within the turbine blade area, causing very large velocity gradients. Behind the wind farm (C7) we notice the vertical wake expansion, due to turbulence mixing. Fig. 4.7a tells us, that the grid-cell interaction is too strong, i.e. a too large drag force at hub-height is applied to the flow. Fig. 4.9a suggests that the too strong interaction can be a consequence of the too concentrated velocity deficits around hub-height.

A comparison between Fig. 4.3 and Fig. 4.7, shows that for the roughness length change approach the velocity reduction at the end of the wind farm is less than 19%, whereas in the ROTOR-DRAG approach it is more than 25%. This difference would lead to a systematic bias in the estimated energy production of a wind farm. Since, the wind farm parametrisation should also be used to estimate the velocity reduction in the near wake of larger wind farms, we discuss two wind farm parametrisation that account for by the mesoscale model unresolved processes.

4.2.3 WRF Wind Farm Scheme

In this section we introduce the WRF-WF approach, which is described in Blahak et al. (2010) and Fitch et al. (2012). These descriptions differ by the fact that the former formulation neglects the possible losses due to mechanical friction.

In the WRF-WF scheme the drag force from Eq. (4.5) is applied to Eq. (4.1). Additional it has been assumed that a wind turbine is, in the grid-cell average, a net source of turbulence kinetic energy. This means that $\overline{u_i f_{D_i}}$ in Eq. (4.3) needs to be parametrised.

The loss of kinetic energy from the atmosphere due to the action of N wind turbines, is obtained by multiplying Eq. (4.5) by the absolute velocity. This gives

$$\frac{\partial E_D}{\partial t} = -\frac{C_T N \sum_k A(k) |U(k)|^3}{2 (\Delta x)^2 \Delta z(k)}, \tag{4.6}$$

On the other hand, the total wind power that is used for the production of electrical energy is

$$\frac{\partial E}{\partial t} = \frac{C_P N \sum_k A(k) |U(k)|^3}{2 (\Delta x)^2 \Delta z(k)}, \tag{4.7}$$

where C_P is the power coefficient. Now, it is assumed that the difference between the total power extracted by the turbines, Eq.(4.6), and the power converted into electricity, Eq.(4.7), is converted into turbulence kinetic energy. With this assumption the additional source term in Eq. (4.3) becomes

$$\overline{u_i f_{D_i}} = \frac{C_e N \sum_k A(k) |U(k)|^3}{2 (\Delta x)^2 \Delta z(k)}. \tag{4.8}$$

The factor of proportionality is consequently, $C_e = C_T - C_P$. In the WRF-WF scheme the relation between the thrust and power coefficient is expected to be in first approximation independent on the wind speed.

In Chapter 5 the WRF-WF scheme is, together with the EWP scheme, evaluated against measurements.

4.3 Explicit Wake Parametrisation

In this section the EWP scheme is introduced. Similarly to the WRF-WF approach, it applies a thrust force to the horizontal components of Eq. (4.1). However, in the EWP approach a grid-cell averaged drag force is applied to the flow, instead of a local thrust force that acts on the turbine blade swept area. A parametrisation for the unresolved turbine-induced wake development within the grid-cell, is chosen, since it is expected to be noticeable. This means that, in order for the EWP scheme to be valid, the grid-size should be larger than a few turbine rotor diameters at least, assuming that the near wake extension is in atmospheric conditions between one (Vermeer et al., 2003) and three rotor diameters (Crespo and Hernández, 1996). This would require for the currently largest

turbine, which has a rotor diameter smaller than 150 m, a horizontal grid-spacing larger than 450 m. This is below the minimum resolution required from the assumptions made in usual mesoscale model parametrisation schemes Wyngaard (2004).

In the EWP parametrisation, the far wake theory is used to estimate the grid-cell averaged wake expansion (Tennekes and Lumley, 1972; Wyngaard, 2010). The downstream development of the approximately Gaussian shaped wake is described by a vertical wake extension and a maximum velocity deficit at the wake centre. These concepts will be described next.

4.3.1 Vertical Wake Extension

The sub-grid-scale flow development is assumed to be approximately stationary for grid-cell advection time scales. This is around 3 min. for a 2 km grid cell and a advection wind speed of 10 $\mathrm{m\,s^{-1}}$. For offshore conditions this assumption is likely to hold, since the changes in sea surface temperature in time and space are mostly small. We define the advection wind speed to be at hub-height (h), $U_0 = \sqrt{U^2+V^2}$, where U and V are the horizontal velocity components in x and y direction, respectively. We assume that the advection and turbulence diffusion term, which are the second and third term on the left hand side of Eq. (4.1), dominate and that the mixing in the turbine wake can be described by a single diffusion coefficient only, $K \equiv K_m(h,t)$. In this way we can obtain a similar equation as Eq. (4.1) for the unresolved wake velocity $\widehat{U}(x,t)$.

$$U_0 \frac{\partial}{\partial x}\left(U_0 - \widehat{U}\right) = K \frac{\partial^2}{\partial z^2}\left(U_0 - \widehat{U}\right). \tag{4.9}$$

Now, the velocity deficit, which is the difference between advection velocity and the unresolved wake velocity, can be written as $U_0 - \widehat{U} = U_s f$. Here the maximum velocity deficit is denoted by $U_s(x)$ and the generic function of the downstream velocity deficit profile by $f(x,z)$. For convenience a non-dimensional length scale $\zeta = z/\sigma$ can be introduced, where σ describes the vertical wake extension. With these definitions, Eq. (4.9) can be written as

$$\frac{U_0\sigma}{KU_s^2}\frac{dU_s}{dx} f - \frac{U_0}{KU_s}\frac{d\sigma}{dx}\zeta f' = \frac{1}{U_s\sigma} f'', \tag{4.10}$$

where the primes denote the derivative with respect to ζ. If we restrict the coefficients in front of f, $\zeta f'$ and f'' in Eq. (4.10) to be constant, we obtain the pair

$$U_s = A\, x^{-1/2} \qquad \text{and} \qquad \sigma = B\, x^{1/2}. \tag{4.11}$$

Equation (4.11) can be found in Tennekes and Lumley (1972, Eq. (4.2.9)) and describes the downstream evolution of the wake. Initially the wake will be narrow with a small

vertical extension and relatively large maximum velocity deficit at its centre. For an increase in distance, the wake depth will decrease, while its vertical extension will increase. If we insert Eq. (4.11) into Eq. (4.10), we obtain

$$\frac{U_0}{2K} B^2 \left(\zeta f' + f\right) + f'' = 0. \tag{4.12}$$

When we define the constant $B^2 = 2K/U_0$. The vertical wake extension as a function of the downstream distance becomes from Eq. (4.11)

$$\sigma^2 = \frac{2K}{U_0} x + \sigma_0^2, \tag{4.13}$$

where σ_0 is the initial wake extension. Eq. (4.13) can be found in Wyngaard (2010). A solution for Eq. (4.12) in a domain that extends vertically from the surface, $z = 0$, to a given height, z_m, reads

$$f = \exp\left[-\frac{1}{2}\left(\frac{z-h}{\sigma}\right)^2\right] \pm \exp\left[-\frac{1}{2}\left(\frac{z+h}{\sigma}\right)^2\right]. \tag{4.14}$$

Here the first term on the right hand side represents the velocity deficit around hub-height, while the second term is the mirror solution to it. A positive and a negative term imply the no momentum flux and momentum flux solutions at the lower domain boundary, respectively. In the following the no flux solution is used.

For this application, the average in the downstream x direction of the Gaussian distribution in Eq. (4.14), is well approximated by a Gaussian with the spread $\overline{\sigma}$ (Appendix A 5.1.7), where

$$\overline{\sigma} = \frac{1}{L}\int_0^L \sigma \, dx = \frac{U_0}{3KL}\left[\left(\frac{2K}{U_0} L + \sigma_0^2\right)^{\frac{3}{2}} - \sigma_0^3\right]. \tag{4.15}$$

Here, L is the sub-grid-scale wake extension. The grid-cell averaged velocity deficit is now determined from the total amount of thrust applied by the wind turbine.

4.3.2 Maximum Velocity Deficit

The grid-cell averaged maximum velocity deficit, U_s, can be obtained by equating the turbine thrust, T, to the momentum removed by the turbine

$$\frac{1}{2}\rho C_T \pi R_0^2 U_0^2 = \rho \int_{\Delta y}\int_0^{z_m} U_0 \left(U_0 - \widehat{U}\right) dz\, dy, = \rho \int_{\Delta y} dy \int_0^{z_m} U_0 U_s f \, dz. \tag{4.16}$$

Here, Δy denotes the width of the wake, while R_0 and $C_T(U_0)$ denote respectively the turbine's rotor radius and the thrust coefficient. Using Eq. (4.14) in Eq. (4.16) gives

$$U_s = \sqrt{\frac{\pi}{2}} \frac{C_T R_0^2 U_0}{2 \Delta y \, \overline{\sigma}}. \tag{4.17}$$

Eq. (4.17) is the maximum velocity deficit, for a velocity deficit profile with a grid-cell averaged vertical wake extension. The final total decelerations in the x and y directions are obtained by inserting Eq. (4.17) into the last term in Eq. (4.16) and dividing by the mass. For the deceleration at the individual vertical levels we obtain

$$F_{D_x}(k) = -\sqrt{\frac{\pi}{2}} \frac{C_T}{2\overline{\sigma}} \left(\frac{R_0 U_0}{\Delta x} \right)^2 f(k) \, \cos\left[\varphi(k)\right] \tag{4.18}$$

$$F_{D_y}(k) = -\sqrt{\frac{\pi}{2}} \frac{C_T}{2\overline{\sigma}} \left(\frac{R_0 U_0}{\Delta x} \right)^2 f(k) \, \sin\left[\varphi(k)\right]. \tag{4.19}$$

Eq. (4.18) and Eq. (4.19) are applied to the discrete Reynolds Averaged Navier-Stokes Eq. (4.1). The function $f(k)$ is equivalent to Eq. (4.14), where the vertical distance, z, is replaced by the height of level k. The wind direction at level k is expressed by $\varphi(k)$. Similar to Peña et al. (2013), we neglect, to a first approximation, the surface reflection of the wake. Eq. (4.18) and Eq. (4.19) are applied for all turbines within a grid-cell. Consequently, we do not consider turbine interaction within one grid-cell. However, the interaction takes place between grid-cells, since a downstream grid-cell experiences a lowered wind speed, due to the applied thrust of the upstream grid-cell. To a first approximation all turbines are considered to be at the grid-cell centre and produce a wake over $L = \Delta x/2$. In this way the parametrisation is independent of grid translation or rotation. Later-on more advanced approaches can be applied. The distance could be a function of the flow angle or we could aim to develop a parametrisation that takes turbine interaction within one grid-cell into account.

4.3.3 Wind Farm Implementation

In this section a short documentation of the practical implementation and a short guideline of the EWP scheme is given. The approach described in Sect. 4.3 is implemented in the WRF model. After the WRF-WF was included in an official WRF release, an optional switch has been build in, to allow the selection between several options. At the moment the WRF-WF, EWP, ROTOR-DRAG, RL and microscale-model (MSC) options are available. The last option uses look-up tables for the thrust generated by a second model. This approach is discussed in Chapter 7.

The EWP approach can be run either in the serial, the shared-memory, or in the distributed memory option. It is not possible to run the approach with the mixed shared

and distributed memory option. The scheme can be used for idealised cases, as well as for real cases. In real case simulations also grid-rotation is possible (this is not possible with the WRF-WF scheme). In the WRF release the WRF-WF scheme depends on the MYNN Planetary Boundary Layer (PBL) scheme and is therefore called right after the MYNN scheme, within the PBL "case". However, since the other options (EWP, ROTOR-DRAG, RL and MSC) do not dependent on a specific PBL scheme, the wind farm schemes obtained their own "case". This "case" is placed in the boundary layer driver right after the PBL scheme has been called.

Initialisation

At the initial time step (not necessarily the first time-step), the required wind farm information is read. The EWP scheme requires a file that includes the wind farm coordinates. This file should contain the specific turbine positions within the model grid-cell, for example "11.5 11.5" would mean a turbine positioned in the centre of grid-cell 11. For the standard application the specific positions are not used, however they can optionally be taken into account. The turbine specification file includes all the turbines within the domain, it can contain the coordinates of several wind farms. In the header of this file the user should specify whether specific turbine types are used, in which case, every turbine coordinate line should also include the turbine type, .i.e. 'V80'. The program will identify the coordinates with the specific turbine type. Additionally a separate file "V80.turbine" should include the turbine characteristics, such as the hub-height and diameter, and the thrust and power coefficients as a function of wind speed. If no turbine type is specified, the Betz limit is used for constant thrust and power coefficients.

Simulation

Throughout the thesis only the default option is used. Optionally turbine positions within the grid-cell can be used, in order to account for the unresolved turbine interaction. With this option the unresolved turbine hub-height velocity is determined for the turbine specific position. The downstream velocity reduction depends on the wind speed, direction, stability and turbine distance. The turbine interaction occurs between all turbines within a wind farm. However, to a first approximation, all turbines within one grid-cell have the same upstream hub-height wind velocity. The interaction takes place only between grid-cells. In the model simulation the wind farm scheme is called every time-step. Within the scheme, a loop over the turbine containing grid-cells if performed. If a turbine containing grid-cell is found within a model tile, the grid-cell averaged thrust and power coefficients are determined using linear interpolation. Thereafter, a loop over the turbines within the specific grid-cell is performed and a total grid-cell thrust per mass in the x and y direction is determined, given by Eq. (4.18) and Eq. (4.19). Finally this thrust is applied to the model Reynolds Averaged Navier-Stokes equation Eq. (4.1).

5

Evaluation of two Wind Farm Parametrisations

5.1 Implementation and evaluation of a wind farm parametrisation in a mesoscale model

P. J. H. Volker, J. Badger, A. N. Hahmann and S. Ott

Wind Energy Department, Technical University of Denmark,
Frederiksborgvej 399,
4000, Roskilde, Denmark

abstract In this article we introduce, implement and evaluate a new wind farm parametrization for mesoscale models. This approach, the Explicit Wake Parametrization (EWP), is compared to i) the current wind farm parametrization as implemented in the Weather Research and Forecast (WRF) Model and calibrated to ii) long term, in situ, measurements from the offshore wind farm Horns Rev I, situated off the west coast of Denmark. The EWP parametrisation is shown to be vertical resolution independent and the velocity deficit remains on hub-height.

5.1.1 Introduction

The contribution from offshore wind energy to the total electricity supply of northern European countries has significantly increased in the last two decades. The growth prospects are promising, since several new large wind farms are planned. Whereas the total installed offshore power for Europe in 2013 was around 4.8 GW, in 2017 it is expected to grow fivefold, to 24.5 GW, as reported by BTM Consult a part of Navigant consulting (2012). Some of the advantages of offshore wind energy compared to that onshore include higher and more steady wind speeds, which lead to an increased and better controllable electricity production. The drawbacks are higher installation and maintenance costs. Since the available areas for construction with favourable conditions are limited, the wind turbine density will probably increase in regions such as the German Bight an the Dogger Bank. Already today we find several wind farm groups, one example being the offshore wind farms Rødsand 2 and Nysted, which are only a few kilometres apart. From a financial perspective, this implies that the study of how wind resources are impacted by the shadowing effect of neighbouring wind farms becomes increasingly important.

High resolution models resolve the flow field around individual wind turbines and account therefore for turbine interactions. This is relevant for an accurate flow estimation within the wind farm, since, especially in the first part of the wind farm, the turbine-induced velocity field varies significantly in the cross-stream direction. With today's computer resources complete wind farm simulations have already been carried out with Large Eddy Simulation (LES) models (Porté-Agel et al., 2013). However, the computational costs are high and the study of wind farm wake flows is still not affordable. From a computational cost perspective, the most favourable models for analysing wind farm wakes are mesoscale and linearised Computational Fluid Dynamics (CFD) models, such as e.g. FUGA (Ott et al., 2011). These two types of models have contrasting advantages and disadvantages. Mesoscale models are not able to simulate the development of the wind velocity deficit in the wake of individual wind turbines due to their coarse resolution, whereas the linearized CFD models, generally, cannot account for mesoscale atmospheric conditions. For the domain size of large groups of wind farms, the variation in atmospheric conditions is of relevance. Furthermore, the flow field is expected to become more homogeneous in the wind farm wake. This encourages the choice of a mesoscale model.

Due to the coarse horizontal resolution of mesoscale models, many atmospheric processes are unresolved and have to be parametrized. An additional unresolved process is the influence of wind turbines to the atmospheric fields. In recent years steady progress has been made in the parametrization of wind farms; from the representation of wind farms by an increased roughness length in Hansen (2007) and Frandsen et al. (2009), up to more sophisticated drag formulations in Adams and Keith (2007), Blahak et al. (2010) and Fitch et al. (2012).

From version 3.2.1 onwards the Weather Research and Forecast (WRF) Model (Skamarock et al., 2008) contains an optional wind farm parametrization (Fitch et al., 2012), hereafter referred to as WRF-WF, which is based on Blahak et al. (2010). The WRF-WF scheme applies a drag force as well as a source term for turbulence kinetic energy (TKE) to every vertical level within the turbine rotor plane. In a qualitative analysis of the WRF-WF scheme we found the following characteristics. The total velocity deficit increased with the vertical resolution, where from a certain vertical resolution onwards the maximum velocity deficit was displaced upwards, to the upper turbine blade tip. The intense mixing causes the velocity deficit to exist up to the Planetary Boundary Layer (PBL) top. These features of the WRF-WF parametrization, however, do not match observations, wind tunnel and LES experiments (Vermeer et al., 2003; Barthelmie et al., 2004; Chamorro and Porté-Agel, 2009; Porté-Agel et al., 2011; Wu and Porté-Agel, 2012). In this article a new wind farm parametrization is presented, which aims at improving the aforementioned limitations. In this parametrization, we account for the unresolved turbine-induced wake development. In this regard the classical wake theory from Ten-

nekes and Lumley (1972) and Wyngaard (2010) is used. The turbine-induced velocity deficit is vertical resolution independent and shows no lifting of the velocity deficit. Furthermore, the smoother vertical distribution of decelerations makes the parametrization numerically stable.

The article is structured as follows. In Sect. 5.1.2 the Explicit Wake Parametrization (EWP) is described. In Sect. 5.1.3 and Sect. 5.1.4 the measurement site is introduced and the model configuration is presented. In Sect. 5.1.5 the WRF-WF and EWP approaches are evaluated against long-term averaged meteorological mast measurements in the wake of the wind farm Horns Rev I. Additionally, we compare the wind farm wake and the velocity profiles of both approaches in a qualitative way. A discussion finalizes the article in Sect. 5.1.6 followed by the conclusion in Sect. (5.1.7).

5.1.2 The Explicit Wake Parametrization

Wind turbines extract atmospheric kinetic energy for electrical power generation. The removal of kinetic energy from the atmosphere brings about a velocity deficit in the wind turbine's wake. To a good approximation, wind turbines can be described as drag devices that slow down the wind velocity from the unperturbed upstream value U by the amount of ΔU. Due to mixing of fluid particles within and outside the wake, the velocity deficit is gradually reduced up to the point at which the background conditions are restored. For offshore wind farms it takes tens of kilometres for the wind velocity to return to its environmental value (Christiansen and Hasager, 2005). The total TKE production associated with the full wake recovery is $P_w = \rho A_r U_r (\Delta U)^2/2$, where U_r is the absolute velocity at the wind turbine rotor, A_r the turbine blade sweep area and ρ the air density. This TKE production accounts for all turbulence production mechanisms associated with the presence of the wind turbine. Within one-dimensional momentum theory (Hansen, 2003), the TKE production in the wake recovery is given by $P_w = \rho A_r 4a^2(1-a)U^3/2$, where a is the induction factor. We will return to P_w later in this section.

We use the mesoscale model to represent as accurately as possible the turbine-induced velocity deficit. Mesoscale models solve, among others, the Reynolds averaged Navier-Stokes (RANS) equations,

$$\frac{\partial U_i}{\partial t} + U_j \frac{\partial U_i}{\partial x_j} + \frac{\partial \overline{u_i u_j}}{\partial x_j} = -\frac{1}{\rho}\frac{\partial P}{\partial x_i} - \varepsilon_{i3k} f U_k - \delta_{i3} g + F_{D_i}. \tag{5.1}$$

In Eq. (5.1) the Boussinesq approximation has been used, i.e. density fluctuations are only considered in the turbulence buoyancy production. The upper-case letters refer to mean quantities, whereas lower-case letters refer to fluctuations, with the exception of $\rho(\mathbf{x},t)$ which represents the average atmospheric density. $U_i(\mathbf{x},t)$ and $P(\mathbf{x},t)$ without subscript denote respectively the mean velocity components and the pressure and f, g

and t, the Coriolis frequency, the gravitational acceleration constant and time. Moreover, we use the Einstein notation, where the index $i = 1,2$ and 3 represents the horizontal directions x, y and the vertical direction z. The Kronecker delta is denoted by δ_{ij} and the Levi-Civita symbol by ε_{ijk}. Equation (5.1) describes the ensemble-averaged velocity evolution, where the second term on the left hand side (l.h.s.) is the advection of velocity by the mean flow and the third term the turbulence flux divergence. The right hand side (r.h.s.) contains the forcing terms, where $F_{D_i}(\mathbf{x},t)$ represents the averaged forcing due to the action of wind turbines ($F_{D_3} = 0$).

The components of the Reynolds stress are in a 1.5-order boundary layer scheme

$$\overline{u_i u_j} = -K_m \frac{\partial U_i}{\partial x_j}, \tag{5.2}$$

where $K_m(\mathbf{x},t) = S_m \ell \sqrt{2e}$ is the turbulence diffusion coefficient for momentum. Here, $S_m(\mathbf{x},t)$ is the stability function for momentum, $\ell(\mathbf{x},t)$ the turbulence length scale and $e = \overline{u_i u_i}/2$ the TKE per unit mass. The only prognostic equation solved in a level 2.5 closure scheme is for the TKE. The most general form of the TKE equation reads

$$\frac{\partial E}{\partial t} + T = P_s + P_b + P_t - \varepsilon, \tag{5.3}$$

where on the l.h.s. the symbol E denotes the TKE and T the transport, which includes the material derivative and the turbulence transport of TKE, as well as the divergence of the pressure correlation. On the r.h.s. P_s represents the turbulence production from the vertical shear in the velocity, P_b the turbulence production or destruction related to buoyancy forces, ε the dissipation and P_t the turbulence induced by the turbine rotor.

For the implementation in the mesoscale model the variables are defined on a 3 dimensional grid. The WRF model uses an Arakawa C grid, in which the bulk variables are defined at the centre of the grid-cell, while all velocity components are defined on the grid-cell boundary. The horizontal and vertical grid-spacing is in the order of kilometres and tens of metres (near to the surface), respectively. Due to the discretization, flow properties smaller than the grid-size remain unresolved and need to be parametrized. Examples of sub-grid scale processes that affect directly or indirectly Eq. (5.1) are: turbulence motion, atmospheric convection, sub-grid scale orographic drag, and wind turbine-induced wakes. A new velocity equation is derived by integrating Eq. (5.1) over each grid-cell and making approximations for the surface integrals that result from the grid-cell averaging. Equation (5.3) is treated in a similar way, resulting in an equation with the same terms as Eq. (5.3) and with E replaced by the grid-cell average of E. In this setting, the TKE represents the fluctuations around the ensemble averaged velocity U (not grid-cell averaged), which includes the mean wake velocity deficit. This means that P_w does not appear as an explicit, additional term in the equivalent form of Eq. (5.3).

The TKE that emerges from the wake decay is taken care of by the shear production term.

We aim to obtain expressions for the terms F_D and P_t that are consistent with the model flow equations. The expression for P_t is found by multiplying the Navier-Stokes equations with the velocity fluctuation and then applying Reynolds averaging. This gives $P_t = \overline{\rho A_r c_T u_i (U_i + u_i)^2}/2$, where c_T is the instantaneous thrust coefficient. The additional turbulence occurs directly after the turbine blades and its magnitude depends on factors, such as the angle of attack that can affect c_T. Its turbulence length scale is of the order of the blade's cord length and it is therefore much smaller than that of the atmospheric flow around hub-height, h, which is around 25 m at $h = 70$ m. This implies a significant higher dissipation rate, $\varepsilon = \overline{u_i u_i}^{3/2}/(b_1 \ell)$, where b_1 is a constant. Moreover, its production occurs only locally near the turbine blade and will therefore hardly affect the grid-cell representative TKE.

In the WRF-WF approach, a forcing term F_D is applied to every turbine blade sweep area intersecting model level and thus describes the local forces that occur at the turbine rotor. The additional TKE source term is parametrized as $P_{t,\mathrm{WRF-WF}} = \rho A_r (C_T - C_P) U^3/2$, where C_T and C_P are the turbine thrust and power coefficients and U the absolute grid-cell velocity. This term is much larger than P_t derived from the Navier-Stokes equations. Furthermore, the application of one-dimensional theory gives, $P_{t,\mathrm{WRF-WF}} = \rho A_r 4a^2 (1-a) U^3/2$, which is equal to the TKE production in the entire wake recovery zone, P_w. From the definition of P_w, it follows that the wake recovery should take place within the grid-cell and the deviation should be that from the grid-cell averaged velocity, instead of around the ensemble mean. Moreover, since P_t, as implemented in the WRF-WF scheme, accounts for all TKE production mechanisms, it includes mainly shear production, which is already part of the model's TKE equation.

In the EWP scheme we assume P_t to be negligible, since the wake expansion due to turbulence by shear production dominates from the near-wake onwards. In the literature it is documented that the near wake ends between D_0, (Vermeer et al., 2003), and $3\,D_0$, (Crespo and Hernández, 1996) after the wind turbine. Here D_0 is used to denote the turbine rotor diameter. The turbulence shear production as included in the discretized Eq. (5.3) acts, however, only on horizontal scales in the order of the grid-spacing Δx. Within the turbine containing grid-cell, where the velocity gradients are the largest, we expect that the sub-grid scale wake expansion from the turbulence by shear production is not negligible. Therefore, we estimate next the sub-grid scale wake expansion in the turbine containing grid-cell and assume that the velocity development in the turbine's wake is described by a turbulence diffusion process resulting from turbulence by shear production. In this way a grid-cell representative forcing term F_D is obtained. The associated turbulence shear production, P_s, is determined by the mesoscale model.

Both schemes have caveats: In the WRF-WF scheme the additional TKE by $P_{t,\mathrm{WRF-WF}}$ dramatically increases the turbulent mixing and because wake recovery does not take place in one grid-cell, superfluous turbulence shear production by the mesoscale model's TKE equation will be added. In the EWP scheme P_w is supplied gradually in the wake by P_s, but the discretization means that the local turbulence shear production in the wake is not resolved and probably underestimated.

Grid-Cell Averaged Vertical Wake Extension

Assuming an even turbine spacing within the wind farm, to a first approximation we position all turbines in their grid-cell centre. Due to the large horizontal grid size, the velocity deficit, which is related to the drag force at the turbine blade's sweep area at the centre of the grid-cell centre, expands until the wake reaches the boundary of the cell (Wu and Porté-Agel, 2012). We account for this wake expansion and apply a grid-cell representative deceleration to the numerical approximation of Eq. (5.1).

In the simple model the velocity field is plane in the cross-stream direction and the unresolved velocity in the stream-wise direction x is denoted by $\widehat{U}(x)$. We assume that in the turbine's wake the horizontal advection of velocity and the turbulence diffusion are the dominant terms in Eq. (5.1) and that the wake's expansion is described by a single turbulence diffusion coefficient, $K \equiv K_m(h,t)$. The unresolved advection velocity is at hub-height, $U_0 = |U(h,t)|$. This gives from Eq. (5.1) and Eq. (5.2) the diffusion equation

$$U_0 \frac{\partial}{\partial x}\left(U_0 - \widehat{U}\right) = K \frac{\partial^2}{\partial z^2}\left(U_0 - \widehat{U}\right). \tag{5.4}$$

The profile of the velocity deficit is defined as a velocity deficit at the centre of the wake times a function ξ, i.e., $U_0 - \widehat{U} = U_s\,\xi$. Here we use $U_s(x)$ for the maximum velocity deficit and $\xi(x,z)$ for the function describing its shape. A solution of Eq. (5.4) is

$$\xi = \exp\left[-\frac{1}{2}\left(\frac{z-h}{\sigma}\right)^2\right] + \exp\left[-\frac{1}{2}\left(\frac{z+h}{\sigma}\right)^2\right], \tag{5.5}$$

where the length scale that determines the vertical wake extension is

$$\sigma^2 = \frac{2K}{U_0}x + \sigma_0^2, \tag{5.6}$$

with σ_0 being its initial length scale. Equation (5.5) and Eq. (5.6) describe the shape of the ensemble-averaged velocity deficit profile at a given distance x. The first term in Eq. (5.5) represents the velocity deficit's shape around hub-height (Tennekes and Lumley, 1972), whereas the second term represents the positive mirror solutions to it. Equation (5.6) is similar to the far wake solution of Eq. (4.29) in Wyngaard (2010). However,

in Wyngaard (2010) the initial length scale was left out.

For mesoscale modelling application, we use a grid-cell representative velocity deficit profile

$$\overline{\xi} = \exp\left[-\frac{1}{2}\left(\frac{z-h}{\overline{\sigma}}\right)^2\right] + \exp\left[-\frac{1}{2}\left(\frac{z+h}{\overline{\sigma}}\right)^2\right], \tag{5.7}$$

with a distance averaged length scale,

$$\overline{\sigma} = \frac{1}{L}\int_0^L \sigma\, dx = \frac{U_0}{3KL}\left[\left(\frac{2K}{U_0}L+\sigma_0^2\right)^{\frac{3}{2}} - \sigma_0^3\right], \tag{5.8}$$

where L represents the horizontal wake extension over half a grid-cell. For this application, the spatial averaged Gaussian shaped velocity profile given by Eq. (5.5) is well approximated by a Gaussian shaped velocity profile of Eq. (5.7), with the spread $\overline{\sigma}$ (Appendix A 5.1.7).

Velocity Deficit at the Wake Centre

The velocity deficit at the centre of the wake determines the velocity deficit's intensity. The maximum velocity deficit is found by equating the total thrust applied to the flow, to the momentum removed by the action of the wind turbine. This leads to

$$\frac{1}{2}\rho\, C_T\, \pi R_0^2 U_0^2 = \rho \int_{\Delta y}\int_0^{z_m} U_0 \overline{U_s}\,\overline{\xi}\, dz\, dy, \tag{5.9}$$

where z_m is the height of the model domain, Δy the width of the wake in the cross-stream direction, $C_T(U_0)$ the thrust coefficient and R_0 the rotor radius. From Eq. (5.9) and Eq. (5.7), we obtain for the grid-cell averaged maximum velocity deficit,

$$\overline{U_s} = \sqrt{\frac{\pi}{2}}\,\frac{C_T R_0^2 U_0}{2\Delta y\,\overline{\sigma}}. \tag{5.10}$$

Inserting Eq. (5.10) and Eq. (5.7) in the right hand side of Eq. (5.9) gives the total turbine-induced force. The final equations for the horizontal force components in Eq. (5.1) are obtained by applying a fraction of the total turbine-induced force (per unit mass) to the relevant vertical levels:

$$F_{D_1}(k) = -\sqrt{\frac{\pi}{2}}\,\frac{C_T}{2\overline{\sigma}}\left(\frac{R_0 U_0}{\Delta x}\right)^2 \overline{\xi}(k)\cos[\varphi(k)] \tag{5.11}$$

and

$$F_{D_2}(k) = -\sqrt{\frac{\pi}{2}}\,\frac{C_T}{2\overline{\sigma}}\left(\frac{R_0 U_0}{\Delta x}\right)^2 \overline{\xi}(k)\sin[\varphi(k)]. \tag{5.12}$$

Here, $\overline{\xi}(k)$ is the discretized function of Eq. (5.7) at the model mass levels k, and $\varphi(k)$ the wind direction. In the EWP scheme we follow Peña et al. (2013), which improved the results for the Park wake model (Katic et al., 1986), when neglecting the second term in Eq. (5.7). Both equations are applied to the numerical approximation of Eq. (5.1) for all wind turbines to all WRF model levels k. Similarly to the linearised CDF model FUGA (Ott et al., 2011), we assume that within one grid-cell the total velocity deficit is obtained from a superposition of single velocity deficits, although in FUGA the individual deficits can be of different magnitude.

5.1.3 Measurements

Horns Rev I

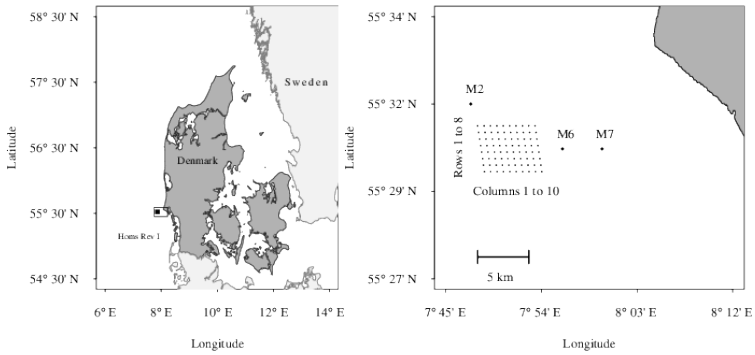

Figure 5.1: Left side: Map indicating the location of the offshore wind farm Horns Rev I. Right side: Map indicating the wind farm layout (dots) and the location of the three met masts (diamonds).

The parallelogram shaped Horns Rev I wind farm is situated about 15 km off the west coast of Denmark (Fig. 5.1). It was, until summer 2013, made up of 80 Vestas V80 wind turbines, resulting in a rated capacity of 2 MW. The turbine diameter is 80 m and the hub is mounted at 70 m above sea level. The equally spaced turbines are placed in 10 columns from west to east, each column has 8 turbines. The turbine spacing between columns and rows is 560 m, which is equivalent to 7 turbine diameters.

Horns Rev I was initially equipped with three met masts. Mast M2 was installed prior to the wind farm installation to document the wind conditions and was located northwest of the wind farm. This mast provided data from 1999 up to the complete calendar year 2006, however the quality of the wind speed and wind direction measurements on M2 was low during 2005, due to a lack of maintenance and during 2006 measurements were even more faulty. Masts M6 and M7 are identically equipped and are located at 2000 m

and 6000 m to the east of the wind farm, aligned exactly between rows 4 and 5. It was intended that for the most frequently occurring westerly winds, these masts would be influenced by the wind farm wake during westerly winds. Mast M6 and M7 continued taking measurements from 2004 up to 2009. Furthermore, wind power measurements produced by the wind farm were stored from 2005 onwards. All data used was 10 min averaged.

Data Selection and Averaging

The power production data is utilised to define the initial length scale, σ_0, in the EWP scheme. From the power production an averaged wind speed over the turbine blade sweep area is derived, which is taken as the hub-height velocity. A column-averaged wind is derived from the inner 6 rows, 2 to 7. The outer rows are excluded because of different wake conditions. The point measurements from the top mounted (70 m) Risø cup anemometers' at mast M6 and M7, have been used to evaluate the modelled wake recovery. The measurements were always normalized against the averaged velocity of the first turbine column, since almost no reliable measurements from the upstream mast M2 were available for this period. Hereafter, we refer to the normalized velocity simply as velocity.

We consider only filtered data from 2005 to 2009, for westerly winds in the range of 7.5 m s^{-1} to 8.5 m s^{-1} at the reference turbine in the 2$^{\text{nd}}$ row of the 1$^{\text{st}}$ column under neutral conditions, $|L_m| > 500$ m, at mast M7. The atmospheric stability is expressed by the Monin-Obukhov length scale, L_m, as a function of the bulk Richardson number (Grachev and Fairall, 1996). A complete description of the masts and the instrumentation and for the data selection can be found in Hansen at al. (2012) and Hansen (2013).

Figure 5.2 shows the time and column-averaged measured velocities for three wind direction intervals: $270^\circ \pm 2.5^\circ$, $270^\circ \pm 7.5^\circ$ and $270^\circ \pm 15^\circ$. The lowest velocities are found within the wind farm for the wind direction interval $270^\circ \pm 2.5^\circ$. A decreasing spread between the different wind direction intervals in distance is shown. This means that, although the turbine interaction is the strongest for small wind direction averaging intervals, it becomes almost independent of the selected wind direction interval due to horizontal wake merging within the wind farm. At half a wind farm distance downstream the lowest velocity is for the $270^\circ \pm 15^\circ$ case. This could be explained by be the position of the met mast, which is exactly between two wind turbine rows. It is expected that for very narrow wind direction bins, the near wind farm wake still depends on this position. Hence, the wake between two wind turbines is less pronounced, when averaged over a small wind direction interval. At around one wind farm distance, the wind farm wake becomes independent of the local turbine positions and consequently the velocity at mast M7 is insensitive to the wind direction interval. Due to the model's coarse resolution, the

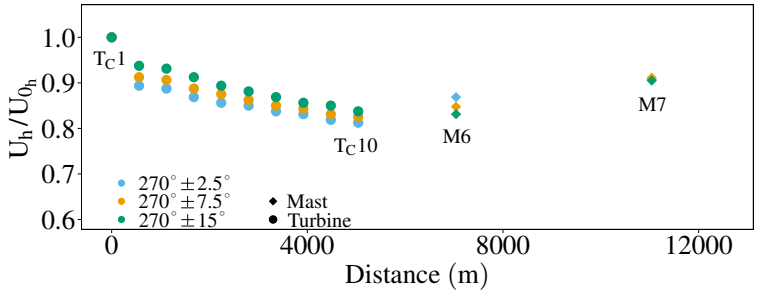

Figure 5.2: Time averaged velocity for three different wind direction sectors. The dots are the averaged turbine wind speeds per turbine column, T_C and the diamonds the averaged met mast wind speeds. All measurements have been normalized by the wind speed of the first column. The wind speeds are from 7.5 - 8.5 m s^{-1}.

local features observed at the first turbine columns and at mast M6 for the small wind direction bins would not be resolved. Therefore, the wake measurements for the largest wind direction interval, $270° \pm 15°$, are selected as a reference.

5.1.4 Model Configuration and Averaging

For the simulations we have used the WRF model version 3.4. The model was run in idealized case mode, with open lateral boundary conditions (Skamarock et al., 2008, p.51), Coriolis forcing on the velocity perturbation from the initial condition and zero heat fluxes from the lower boundary. At the surface the no slip condition holds. The model was initialized with a homogeneous, dry, slightly stable atmosphere and with a constant geostrophic wind, which converged to a neutral boundary layer with an absolute velocity of 8 m s^{-1} $\pm$0.03 m s^{-1} in the different model runs. The roughness length was constant and set to a typical value for the sea-surface, $z_0 = 2 \cdot 10^{-4}$ m. In the idealized case mode the Coriolis frequency is set to $f = 1 \cdot 10^{-4}$ s^{-1} corresponding to a value for mid-latitudes.

To study the model's sensitivity to the vertical resolution, three experiments with a relatively low, medium and high resolution were conducted. The three domains contain 28, 40 and 80 vertical layers and are indicated in the following as L28, L40 and L80, respectively. With increasing vertical resolution there are 3, 5 and 10 grid-cell volumes intersecting with the turbine rotor. The experiment with the coarsest resolution is included to provide an example for the use of computationally inexpensive calculations. Roy and Traiteur (2010) used a similar vertical resolution in their simulations performed with the Regional Atmospheric Modeling System (RAMS) model. The fully compressible WRF model uses (terrain-following) hydrostatic pressure coordinates. Figure 5.3a

shows the vertical model grid position of the unstaggered mass-levels for the three model configurations at the moment of evaluation. At the evaluation time the model hub-height levels were at 70.4 m, 70.9 m and 70.1 m and the lowest model levels at 24 m, 10 m and 3.4 m for the L28, L40 and L80 simulations, respectively.

In the horizontal plane the model was set-up with 80×30 grid-cells, with a grid-spacing

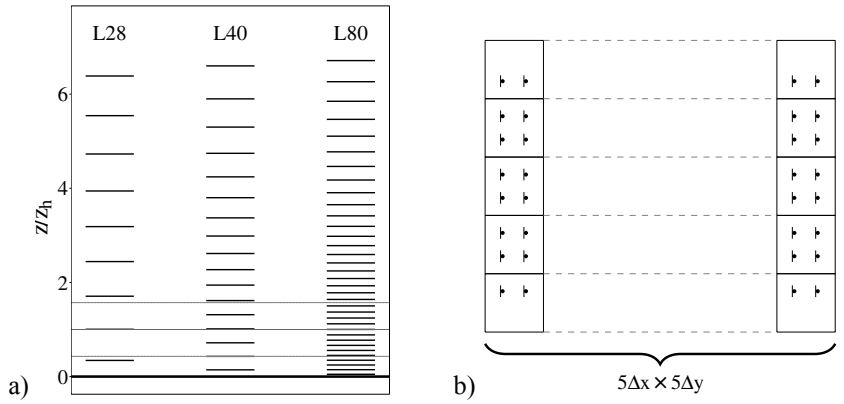

Figure 5.3: a) Vertical grid positions of the model mass-levels for the three simulations with a different vertical grid-spacing. The turbine hub-height is marked by the solid grey line, the upper and lower turbine blade tip by the dashed lines. b) an illustration of the model wind farm layout as applied in the mesoscale model. The squares indicate the model grid-cells.

$\Delta x = 1120$ m, which is optimal for the wind farm turbine spacing. The model wind farm extension is 5 grid-cells in the West-East, as well as in the North-South direction (Fig. 5.3b). With this layout the 3 central rows contain 4 turbines per grid-cell, whereas the most northern row and the most southern row contain 2 turbines per grid-cell. In this set-up the three central rows are comparable to the column average applied in the observations, since they do not include turbines from the most northern and southern turbine rows. To account for the wind direction averaging in the measurements, the mesoscale model was run for 7 wind directions ranging from 258.75° to 281.25°, with a 3.75° interval. For all simulations the MYNN 1.5 order Level 2.5 PBL scheme (Nakanishi and Niino, 2009) was used. The model configuration is shown in Table 5.2. The thrust coefficient was taken from the Vestas V80 thrust curve. For the analysis, simulations were performed for 7 wind directions and 3 resolutions, with and without a wind farm. The model simulations without a wind farm served to determine the unperturbed flow conditions. These runs are used for the normalization of the wind farm simulations. In the same way as for the measurements, the simulated absolute velocities are always normalized and hereafter simply referred to as velocity. Within the wind farm, a column averaged wind speed is obtained by averaging over the 3 central grid-cells. In the wind

Table 5.1: Table describing the WRF configuration used for the simulations

Wind direction range (°):	258.75 – 281.25
Wind direction interval $\Delta\theta$ (°):	3.75
Domain (nx,ny):	80, 30
Horizontal domain extension x, y (km, km):	89.6, 33.6
Domain (nz):	28, 40, 80
Horizontal grid spacing (m):	1120
Wind farm extension (nx $\times$ ny):	5×5
Boundary condition:	OPEN
PBL scheme:	MYNN (1.5)
Convection/Microphysics scheme	Not used
pert Coriolis:	TRUE

farm wake only the central grid-cell is used, to conform with the mast measurements. In the comparison with measurements, an average over the different wind directions has been performed. For consistency with the measurements, we set the unresolved hub-height velocity of the first model turbine column at distance zero to unity. The first wind farm grid-cell velocity is then located at 280 m downstream.

Wind Farm Scheme Adjustments

EWP scheme

We use the power production measurements of the turbine to determine the initial length scale σ_0 in Eq. (5.8). The initial length scale is, in first approximation, defined to be independent of upstream conditions and is therefore constant for all turbines. In the experiments the initial length scale was varied from $\sigma_0 = R_0$ to $\sigma_0 = 1.5R_0$. In Fig. 5.4a we show the wind direction averaged, hub-height velocity within the wind farm for $\sigma_0 = 1.5R_0$. We find that the velocity deficit is independent of the vertical resolution within the wind farm. This guarantees that the amount of energy extracted by the turbines does not change with the vertical resolution. The experiment with an initial length scale $\sigma_0 = 1.5R_0$, shows a fairly good agreement with the power measurements. The initial length scale is assumed to be at the end of the control volume used in the one-dimensional momentum theory. At this point, the turbine-induced pressure perturbation has returned to the background value and the radius of the top-hat velocity field is $R = \sqrt{2}R_0$ (Frandsen, 2007). However, viscid effects and atmospheric vertical meandering (Bingöl et al., 2007) are also expected to influence the initial vertical wake extension.

Figure 5.4b shows the difference in velocity, when using an initial length scale $\sigma_0 = R_0$ and $\sigma_0 = 1.5R_0$ for a horizontal cross-section at hub-height. It shows that the sensi-

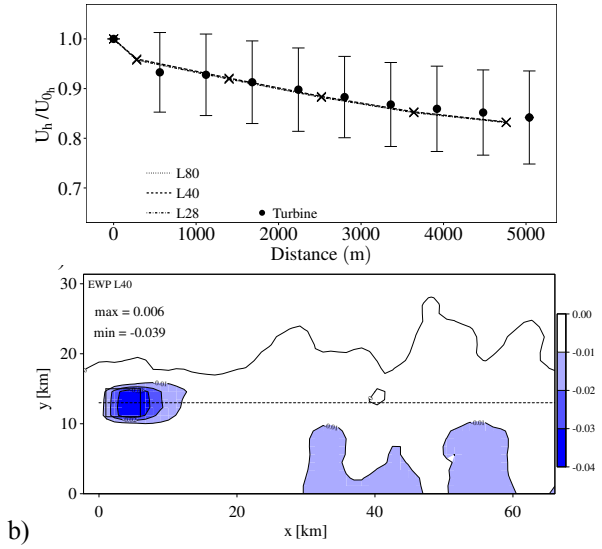

Figure 5.4: Velocity fields for the EWP scheme. a) Hub-height velocity within the wind farm. The turbine row averaged velocities and their standard deviations are represented by the dots and bars, respectively. The lines show the model's wind direction averaged velocities with an initial length scale $\sigma_0 = 1.5R_0$ for the 3 vertical resolutions. The crosses mark the grid-cell centre. U_h and U_{0_h} denote the downstream and reference hub-height velocity, respectively. b) Velocity deficit difference with an initial length scale of $\sigma_0 = R_0$ and $\sigma_0 = 1.5R_0$ on the x,y plane at hub-height for the L40 simulation.

tivity to the initial wake extension is less than 4% at the end of the wind farm and that it is limited to the near wind farm wake.

WRF-WF scheme

The WRF-WF scheme applies the additional source term $P_{t,WRF-WF}$ (Sect. 5.1.2) per unit mass, to the model's TKE (per unit mass) equation. The intensity of this term depends on the difference between the thrust and power coefficients. In the default WRF-WF scheme, the power coefficient is obtained from a predefined power curve. The thrust coefficient is then derived by the empirical relation $C_T = \min(7C_p/4, 0.9)$. Figure 5.5 shows the wind direction averaged velocity for the L40 simulation of the WRF-WF scheme as it is implemented in the WRF model, i.e. the thrust coefficient has not been corrected to match that of the V80 turbine. The velocity reduction, $1 - U_h/U_{0_h}$, is underestimated with the default WRF-WF scheme. At mast M6 the difference between the measured average velocity is the largest, whereas difference at mast M7 is reduced. The

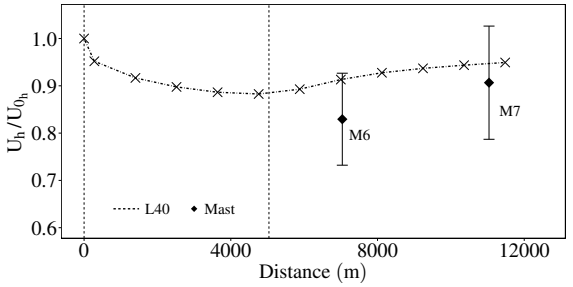

Figure 5.5: The hub-height velocity as a function of the downstream distance. The diamonds represent measurements at mast M6 and M7 for the wind direction interval between 255° and 285°, with the standard deviation as a bar. The dashed line represents the wind direction averaged velocity for the default WRF-WF scheme for the L40 simulation only. The crosses indicate the velocity at the grid-cell centre. The vertical lines show the horizontal wind farm extension in the West-East direction.

too high velocities can be explained by the too low thrust coefficient.

To be consistent with the EWP scheme, we use in the analysis the thrust coefficient from the specific turbine thrust curve. Thereafter, we update the power coefficient with the inverse relationship from above, namely $C_p = C_T/1.75$. The maximum thrust coefficient for the V80 turbine is less than 0.9, hence there is no conflict with the minimum selection of the expression for C_T.

Wind Direction Selection

Before the model is evaluated against the measurements, its sensitivity to the wind direction variation is examined. Figure 5.6 shows the velocity at hub-height for the EWP and WRF-WF scheme for the L40 simulations. Many similarities for both parametrizations are apparent. In the first turbine containing grid-cells, almost no sensitivity to the wind direction is found. After a few grid-cells, the 255° simulation starts to diverge slightly, since the upstream grid-cell affects less that downstream. In the wake of the wind farm, the model runs start to diverge from each other for the different flow angles. The divergence is slightly larger for the EWP approach. The asymmetrical features in the model solution are explained by the action of the Coriolis force. A slowing down of the flow results in a further turning to the left. This is clearly recognized in the EWP simulations, where the velocity reduction in the 258.75° is less than in the 281.25° simulation. In the WRF-WF simulation, the reduction of the velocity in these two simulations is, however, reversed.

A Comparison of Fig. 5.6 and Fig. 5.2 reveals some differences in model and mea-

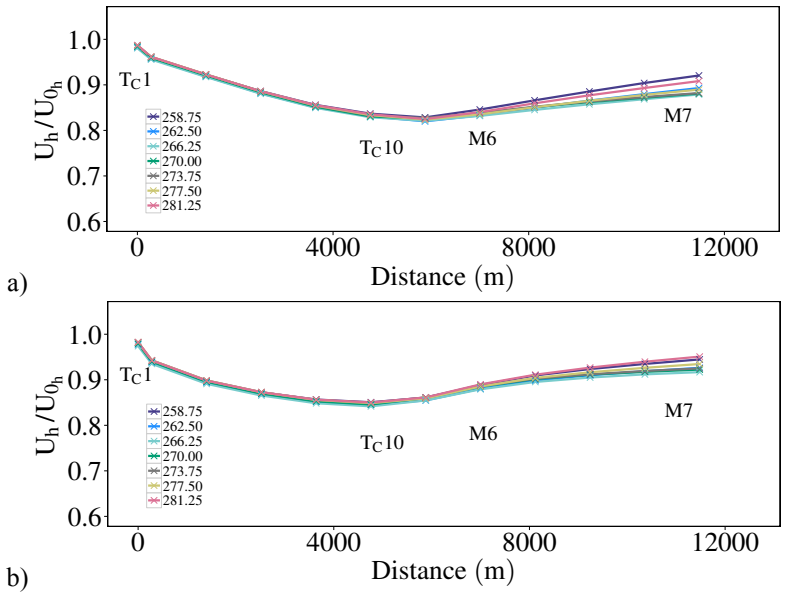

Figure 5.6: Velocity from the L40 simulations for the individual wind directions within and in the near wind farm wake for a) the EWP scheme and b) the WRF-WF scheme. Similarly to Fig. 5.2, the positions of the first and tenth turbine column, as well as the met masts' positions are indicated.

surement behaviour. Within the wind farm, only the measured wind speeds at the first turbine columns are sensitive to the chosen wind direction interval. From the wind farm layout in Fig. 5.1, it can be seen that the turbine interaction between two columns is the strongest for wind directions around 270°. If we consider that in the first wind farm columns the wakes of different rows might not have merged yet, it becomes clear that the turbine's measurements in the first columns, when averaged over a small wind direction interval, behave as point measurements which do not represent a large area. On the other hand, the modelled velocity is within the first wind farm grid-cells independent of the wind direction. Furthermore, the model is not able to account for the observed local flow features at mast M6, when averaged over 270 $\pm$2.5°. Consequently, to obtain two comparable data-sets the measurements have to be averaged over the large wind direction interval 270 $\pm$15° as it was chosen in Sect. 5.1.3. Further downstream, the measured velocity at mast M7 is independent of the wind direction interval (Fig. 5.2), whereas the model is not. The layout in Fig. 5.1 suggests that mast M7 should be in the complete wind farm wake only for wind directions between 260° and 280°. The fact that even for a 30° interval the measured velocities are invariant to wind direction averaging, is partially explained by a horizontal wind farm wake expansion. However, also additional

atmospheric mechanisms, such as horizontal wake meandering, are required, which are not accounted for in our idealized case flow. Hence, we chose not to simulate the flows with a converged wind direction of 255° and 285°.

5.1.5 Evaluation of the Wind Farm Schemes

We examine the velocity at hub-height, the near and far wind farm wake characteristics, as well as the vertical profile of wake deficits. The velocities have always been normalized, see Sect.(5.1.3) and Sect.(5.1.4). The term near and far wind farm wake is used for a respectively 10% and 5% velocity reduction compared to the reference velocity. The definition of the near and far wake is not related to any physical regime change, but it has been used for terminology convenience.

Velocity Recovery at Turbine Hub Height

Figure 5.7a shows the wind direction averaged velocity for the EWP scheme as a function of the downstream distance. The velocity is nearly independent of the vertical resolution inside and in the near wake of the wind farm. Only a small difference is found at mast M7, which converges further downstream (not shown). The modelled velocity in the near wind farm wake is in line with the measurements. However, the wake depth is overestimated at mast M7.

Figure 5.7b shows a horizontal plot of the hub-height velocity for the L40 simulation in the 270° wind direction. The near wind farm wake extension is around 10 km, the far wind farm wake 23 km. The velocity reduction, $1 - U_h/U_{0_h}$, at the end of the wind farm and at 2 kilometre downstream is 16.7% and 16.3%, respectively.

Figure 5.8 shows the same plots as Fig. 5.7, this time for the WRF-WF scheme. The simulated velocity is overestimated, but fits inside one standard deviation of the measurements. Furthermore, inside the wind farm a decrease in the velocity with increasing vertical resolution is shown. The velocity difference between the L28 and L40 simulations is almost equal to that between the L40 and L80 simulations. At mast M7, the simulations with the different resolutions nearly converge to the same value. Figure 5.8b shows that the near wind farm wake extends to 3 km, while the far wind farm wake to 17 km. For the WRF-WF scheme we find a velocity reduction at the end of the wind farm of 15.3%, which is reduced to 11.5% at 2 kilometre downstream.

A comparison between Fig. 5.7a and Fig. 5.8a, shows for the EWP scheme within the wind farm an almost linear velocity decrease with distance, whereas the velocity in the WRF-WF simulation is closer to constant at the end of the wind farm. The linear decrease in velocity suggests that there is still no equilibrium reached between the extracted momentum by the wind turbines and the compensating flux of momentum from

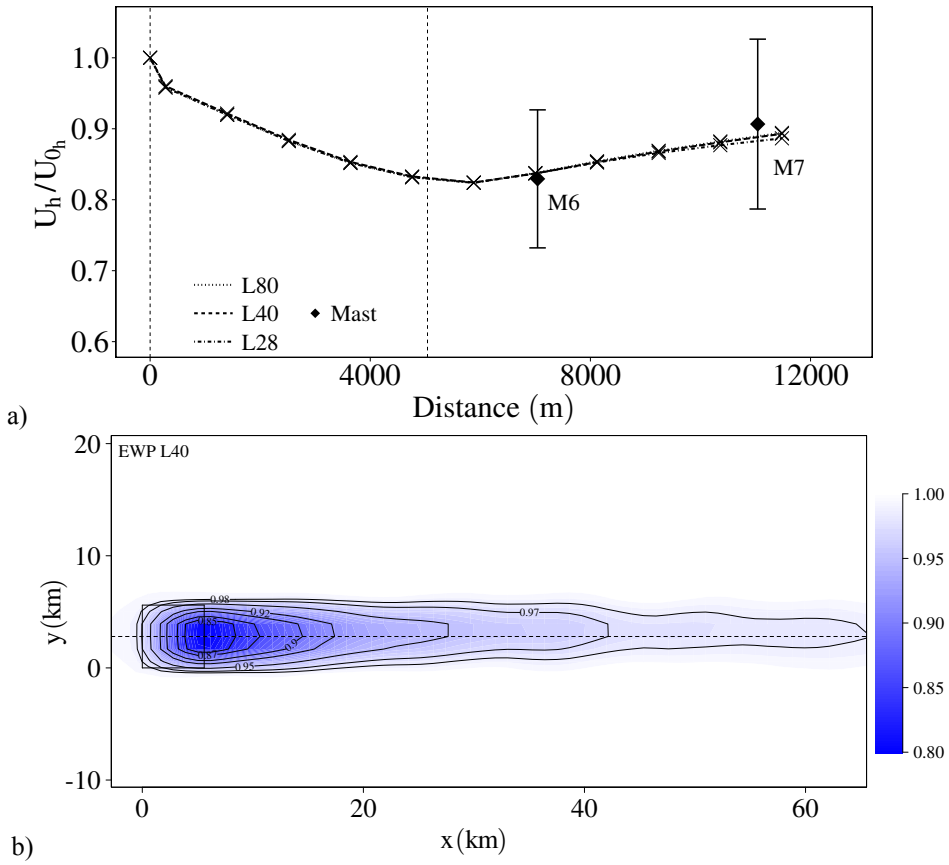

Figure 5.7: Velocity field for the EWP scheme: a) Wind direction averaged velocity at hub-height for the L28, L40 and L80 simulations as a function of distance. The symbols used are equal to those in Fig. 5.5. b) Horizontal view of the velocity field at hub-height for the L40 simulation in the 270° wind direction. The dotted line from left to right indicates the centre of the wind farm. The rectangle represents the wind farm location.

above. On the other hand, the nearly constant velocity at the end of the wind farm in the WRF-WF scheme indicates that the extraction of momentum is almost balanced by the turbines and the flux of momentum from aloft. This strong and maintained momentum flux may be responsible for the fast near wind farm wake recovery in the WRF-WF scheme.

Figure 5.7b and Fig. 5.8b show that the velocity reduction between the schemes dif-

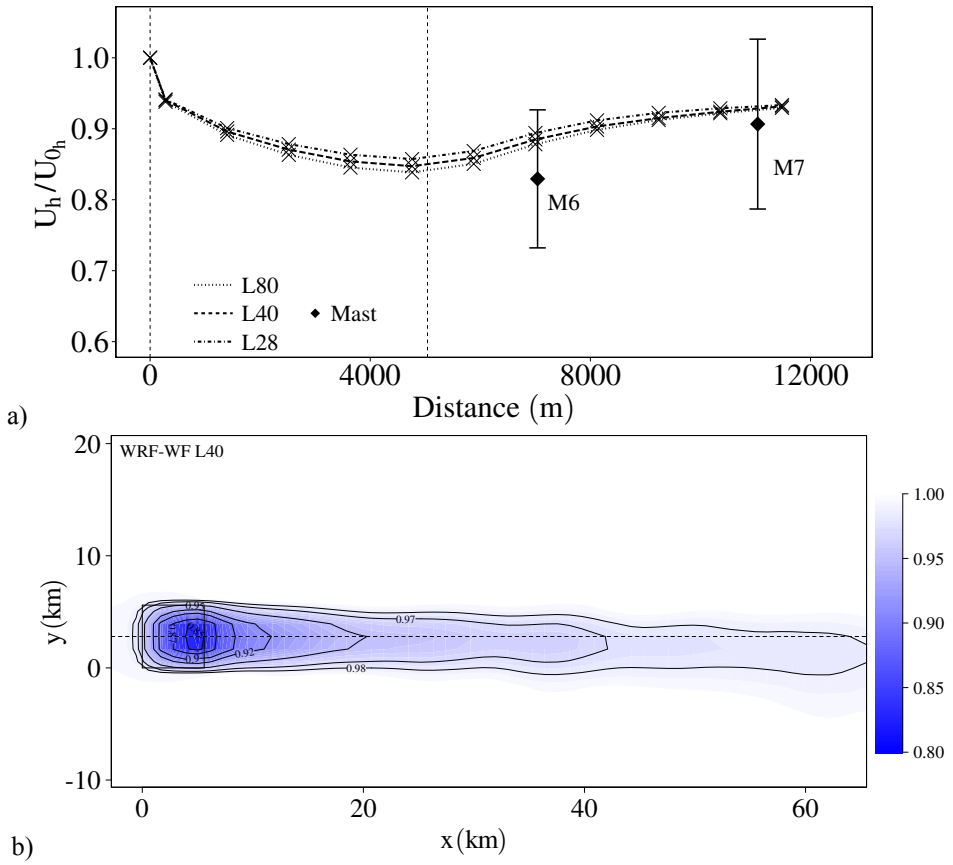

Figure 5.8: Velocity field for the WRF-WF scheme. A description is given in Fig. 5.7.

fers at the end of the wind farm only by 1.7%, which at mast M6 is increased to 5.5%. Further downstream after around 35 km the velocity fields from the two parametrizations start to converge. Finally, a difference in the wake orientation exists. In both simulations the steady-state wind direction of the unperturbed flow was 270.1°. Due to the slowing down of the wind speed after the wind farm, a turning of the wind speed to the North is expected due to the changed Coriolis forcing. This effect is simulated with the EWP scheme (Fig. 5.7b), however, in the WRF-WF scheme the wake turns in the opposite direction (Fig. 5.8b). A possible reason for this behaviour could be the turbulence transport of wind from aloft (which is turned clockwise).

Wind Velocity Profile

To obtain a better understanding of the schemes' mechanisms, we compare the simulated TKE (per mass) and the velocity deficit profiles for the 270° wind direction. The cross-sections in the x, z plane used for the TKE plots are in the West-East direction and they pass through the centre of the wind farm. Figure 5.9 shows the TKE difference for the wind farm minus control simulation for both parametrizations and all resolutions. The wind farm averaged TKE profile from the reference run is shown in Fig. 5.10. In the Figs. 5.9a,b,c and Figs. 5.9d,e,f different colour intervals have been used, due to the relatively large differences in TKE production between the two schemes. The contour lines start from the same TKE difference. The figures show that the TKE production is nearly resolution independent in both parametrizations. Figures 5.9a,b,c show for the EWP scheme an increased TKE above hub-height and a decreased TKE below hub-height. The increased and decreased TKE are caused by an enhanced and reduced shear production, respectively. The maximum increase happens right after the wind farm where the accumulative velocity deficit is the largest. On the other hand, Figures 5.9d,e,f show for the WRF-WF scheme an increased TKE from the lowest model level upwards within the wind farm. The maximum TKE increase is at hub-height due to the additional source term P_t. The combination of the additional source term and the turbulence shear causes a strong mixing in the vertical direction. Compared to the environmental TKE (Fig.5.10), we find that for the EWP scheme the TKE increases in the wind farm wake by a factor of 2, whereas for the WRF-WF scheme it increases by a factor of more than 5.

The turbulence, which is completely parametrized in mesoscale models is not directly comparable to the turbulence in LES models. However, a comparison between the turbulence intensity in Fig. 5b from Wu and Porté-Agel (2012) and the simulated grid-cell representative TKE with the EWP parametrization shows some common features. In both cases we find a decreased turbulence under the lower turbine blade tip and increased turbulence above the upper turbine blade tip. Furthermore, Fig. 12 of Wu and Porté-Agel (2012) shows for aligned wind turbines an upper wake edge of around 3.5 turbine hub-heights after 60 turbine diameters. Wu and Porté-Agel (2012) defined the wake edge at the point where the velocity reduction at a given height was 1%. Similarly the wake edge is found from an increased TKE due to shear production. A crude estimation gives that the vertical wake extension is around 4 and 6 turbine hub-heights at 60 turbine diameters in the EWP and WRF-WF scheme,respectively. Furthermore, a better agreement is found for the EWP scheme in the downstream growth of the internal mixing layer compared to Fig. 12 in Wu and Porté-Agel (2012).

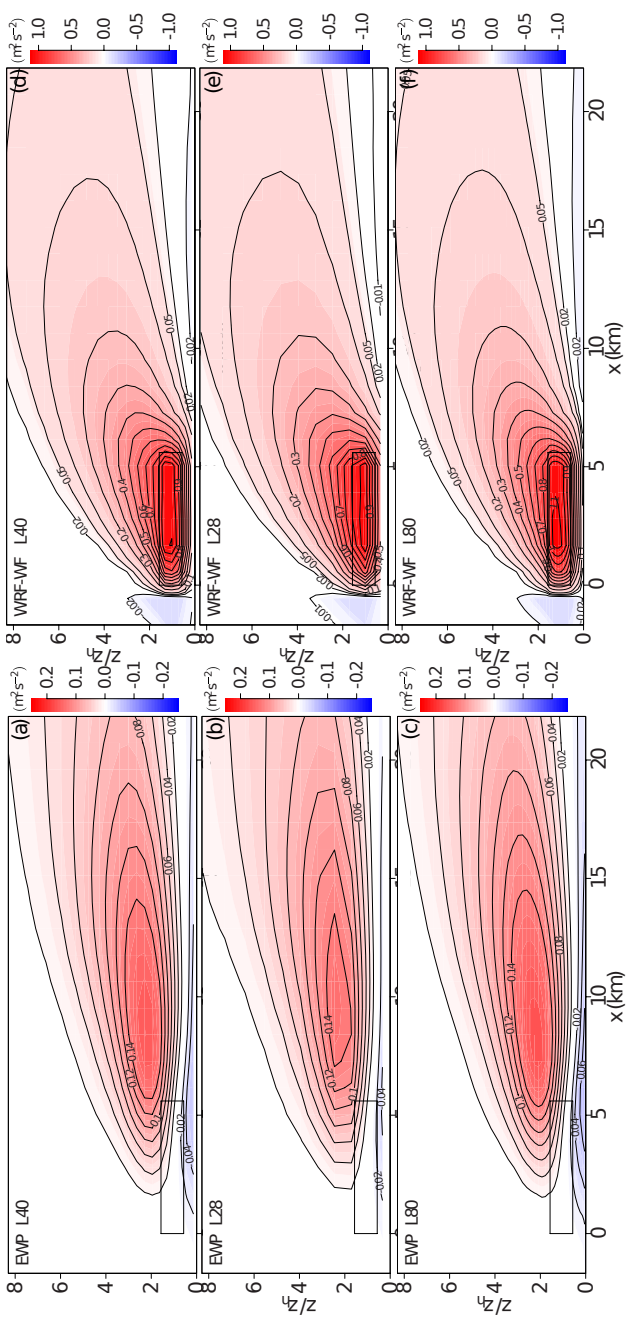

Figure 5.9: TKE difference $(e_{\mathrm{wf}} - e_{\mathrm{ref}})$ $(\mathrm{m}^2\ \mathrm{s}^{-2})$ for both wind farm parametrizations and all vertical resolutions. The cross-sections pass through the wind farm. The rectangle encloses the area spanned by the turbine rotor and the horizontal wind farm extension. The horizontal wind farm extension is from the left boundary of the first turbine containing grid-cell to the right boundary of the final turbine containing grid-cell. a) L40 EWP scheme, b) L28 EWP scheme, c) L80 EWP, d) L40 WRF-WF e) L28 WRF-WF, f) L80 WRF-WF.

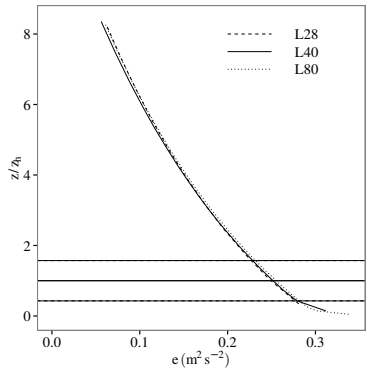

Figure 5.10: TKE profile from the reference simulation. The line types represent the different resolutions. The vertical turbine blade extension is marked by the dashed horizontal lines.

Figure 5.11 shows for both schemes and all resolutions the velocity deficit $\Delta U_x/U_{0_h}$ at two points within the wind farm and one point in the wind farm's wake. The velocity deficit is defined as $\Delta U_x = U(z) - U_{\text{up}}(z)$, where $U_{\text{up}}(z)$ is the upstream velocity from the reference simulation and $U(z)$ the velocity from the wind farm simulation for the considered grid-cell. We notice that the vertical extension of the velocity deficit shown in Fig. 5.11 is in line with the contour lines of an $0.02\,\text{m}^2\,\text{s}^{-2}$ increased TKE (Fig 5.9). For the WRF-WF scheme there is a shifting of the maximum velocity deficit above hub-height. With increasing downstream distance the vertical displacement of the maximum velocity deficit increases and it reaches the upper wind turbine blade tip at mast M6. The apparent fast recovery at hub-height in the WRF-WF scheme, shown in Fig. 5.8a, is partially explained by the upwards displacement of the maximum velocity deficit. In the EWP scheme, instead, the maximum velocity deficit remains at hub-height. LES simulations and measurements (Porté-Agel et al., 2011; Wu and Porté-Agel, 2012; Vermeer et al., 2003) show also a maximum velocity deficit in the far turbine wake at, or even below, hub-height. Figure 5.11b confirms the vertical resolution independence of the EWP parametrization: the velocity deficits of the L28 and L80 simulations are almost identical. A small difference is found after the wind farm at around 3 turbine hub-heights. The difference could be caused by slightly different atmospheric conditions aloft in the L28 and L80 simulation. Figure 5.11c shows that in the WRF-WF scheme the integral of the velocity deficit over height increases with the resolution, i.e. the total velocity deficit for the profile with the solid lines is smaller than that with the dashed lines. Furthermore, we observe increased velocities inside the wind farm at the lowest model level with a high vertical resolution. In the aligned wind farm simulations of Wu and Porté-Agel (2012) (Fig. 13), no higher velocities were simulated in the lower wake.

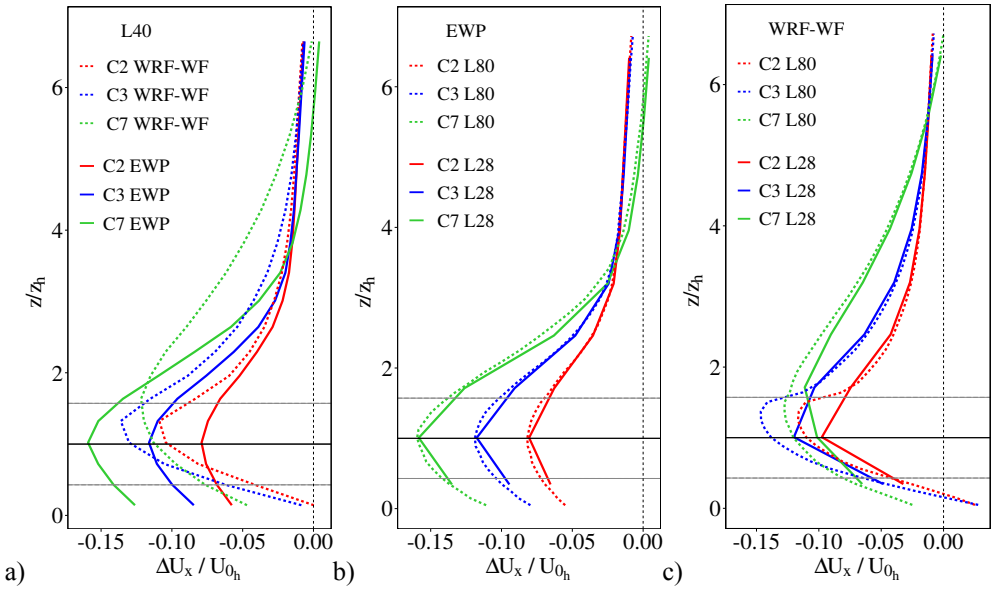

Figure 5.11: Velocity deficit for the second (C2) and third turbine containing grid-cell (C3) at 1400 m and 3640 m and for mast M6 (C7) at 7000 m downstream. The wind turbine hub-height is indicated by the horizontal solid line and the turbine blade top and bottom by the dashed lines. a) L40 simulation for EWP and WRF-WF scheme, b) L28 and L80 simulation for the EWP scheme, c) same as Fig. 5.11b, but for the WRF-WF scheme.

5.1.6 Discussion

In this article we use the mesoscale model to simulate the effects of a large wind farm to the flow. The steady-state solution of the velocity field in the wind farm wake has been evaluated with the long-term average of meteorological mast measurements at 2 and 6 km downstream from the wind farm. Measurements were selected for the wind direction range between 255° and 285° and importantly the model has been run for several wind directions within the same wind direction interval. However, to obtain an as large as possible data sample, wind direction steadiness has not been taken into consideration for the met masts. This might underestimate the measured normalized velocity deficit at M7, since the velocity reduction is becoming more sensitive to a wind direction steadiness with increasing distances from the wind farm. Furthermore, the measurement data had to be normalized against the first turbine column, since no upstream measurements were available. On the other hand, in the same way the model velocity fields were normalized against a reference simulation without turbines. Thereby, we assumed that the upstream flow deceleration due to the positive pressure gradient is for the considered wind farm size still low.

Within the wind farm turbine power measurements were used to determine the unknown initial length scale ($\sigma_0 = 1.5R_0$) of the EWP parametrization. The derived wind speed from the power measurements represents a turbine blade sweep area averaged velocity, which is assumed to be comparable to the hub-height wind speed. Future measurements or results from LES models should be used to confirm this value.

The point measurements of the met masts in the wake of the wind farm have been used for the model evaluation. The modelled velocity field in the wind farm's wake was sensitive to the wind farm parametrization, especially for small distances. Whereas the velocity reduction between the two methods differed at the final turbine column by 1.7% only, at 2 km downstream the difference grew more than threefold to 5.5%. This implies, that the parametrizations not only influence the atmospheric fields within the wind farm differently, but also those in the wind farm wake. Furthermore, a turning to the left of the wind farm wake was found with the EWP parametrization and to the right direction with the WRF-WF parametrization. From the action of the Coriolis a turning to the left is expected. A turning to the right can be explained from the intensive downwards transport of wind from aloft, caused by the large momentum fluxes in the WRF-WF scheme. To obtain a more complete picture of the wind farm wake recovery, remote sensing is a promising source of data for future work and current Light Detection And Ranging (LIDAR) and Synthetic Aperture Radar (SAR) measurement campaigns are expected to contribute.

5.1.7 Conclusion

In this article we introduced a new wind farm parametrization for mesoscale models. We compared the EWP parametrization to that implemented in the WRF model and evaluated both schemes against long-term mast measurements in the wake of the wind farm. We performed simulations for a low, medium and high vertical resolution, with 28, 40 and 80 vertical model levels, respectively.

The EWP parametrization, is based on classical wake theory. In contrast to the WRF-WF scheme, we aim to describe the unresolved turbine-induced wake expansion explicitly in the turbine containing grid-cell, where the largest velocity gradients occur. The associated turbulence shear production is then determined by the model itself. In the evaluation we found that the velocity field of both wind farm parametrizations fitted within the measurements' uncertainty, given by their standard deviation. However, several fundamental differences in behaviour were found.

For mesoscale applications it is important that the parametrization produces vertical resolution independent results. This guarantees that the same amount of energy is

extracted by the wind farm for every vertical resolution. We found that the EWP was resolution independent inside the wind farm. Regarding the WRF-WF scheme no flow convergence within the wind farm for the three vertical resolutions was found. The differences in the hub-height velocity between the low and standard resolution are nearly the same as those between the standard and high resolution. Therefore, a flow convergence test within the wind farm is recommended before applying the WRF-WF scheme.

From LES simulations (Wu and Porté-Agel, 2012), we find an increased turbulence intensity above hub-height and a decreased turbulence intensity below hub-height, for areas with increased and decreased turbulence shear production. A comparable behaviour was found in the simulations with the EWP parametrization. The evolution of the vertical wind farm wake extension in the EWP parametrization is therefore similar to that in Wu and Porté-Agel (2012). One consequence of the TKE profile as simulated with LES models (Wu and Porté-Agel, 2012) or modelled with the EWP scheme, is that the maximum velocity deficit is found close to the hub-height.

In the study of wind farm interaction, the aforementioned differences in the EWP and WRF-WF scheme can be important. The wind farm spacing of offshore wind farms can be down to only a few kilometres as in the case of the Danish wind farms Rødsand 2 and Nysted. At two kilometres downstream of the wind farm, the difference between the two schemes was 5.5%. In the future a quantitative evaluation against remote sensing data, should give further insights regarding the wind farm wake recovery and the velocity deficit profile over the sea-surface.

Appendix A

We compared the difference between a distance averaged velocity profile from 5000 single profiles and the approximated distance averaged Gaussian shaped velocity profile for typical parameters. The velocity profile is given by $U_s\,\xi$, where U_s is the maximum velocity (deficit) at the centre of the wake and ξ the first term of the velocity's shape function. In the first case we apply at any distance from 0 m to 500 m, Eq.(5.6) to

$$U_s = \sqrt{\frac{\pi}{2}}\,\frac{C_T\,R_0^2\,U_0}{2\Delta y\,\sigma}$$

and Eq. (5.5). Thereafter, the profiles have been averaged over distance. In the second case we calculate the distance averaged velocity profile from

$$\overline{U_s} = \sqrt{\frac{\pi}{2}}\,\frac{C_T\,R_0^2\,U_0}{2\Delta y\,\overline{\sigma}},$$

Eq. (5.7) and Eq. (5.8). For the comparison we used $U_0 = 8\,\mathrm{m\,s^{-1}}$, $R_0 = 40\,\mathrm{m}$, $\sigma_0 = 60\,\mathrm{m}$, $C_T = 0.8$, $K = 6\,\mathrm{m^2\,s^{-1}}$ and a wake width, $\Delta y = 1120\,\mathrm{m}$. The wake centre is defined at $z = 0\,\mathrm{m}$. The result in Fig. 5.12 shows that the differences between the spatial averaged

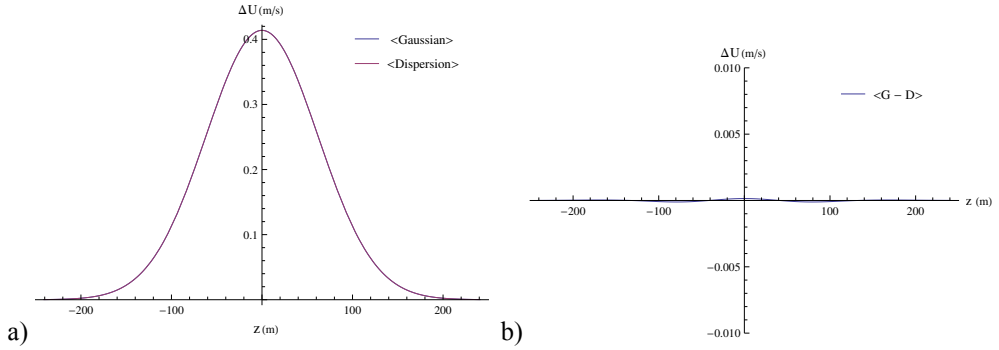

Figure 5.12: The Fig. a) shows a comparison between the average of the Gaussian velocity deficit profiles (blue line) and the Gaussian profile with the average spread $\overline{\sigma}$ (red line) and Fig. b) the difference between the space averaged Gaussian profiles and the Gaussian profile with the average spread.

Gaussian profiles and the Gaussian profile with the space averaged spread is in the entire velocity deficit region far less than $0.001\,\mathrm{m\,s^{-1}}$.

Acknowledgements

Funding was provided by the Wind resource Assessment audit and standardization (WAUDIT) programme, financed by Marie Curie ESR-FP7. We would like to acknowledge

Vattenfall AB and DONG Energy A/S for providing us with data from the Horns Rev I offshore wind farm. The authors acknowledge Kurt Schaldemose Hansen help with the for the data selection. The authors gratefully acknowledge the suggestions of Paul van der Laan of DTU Wind Energy as well as the helpful discussions with Jerry H-Y. Huang and Scott Capps, both from the Department of Atmospheric and Oceanic Sciences, UCLA.

5.2 Wind-Farm Parametrisations in Mesoscale Models

P.J.H. Volker, J. Badger, A.N. Hahmann and K.S. Hansen

Wind Energy Department, Technical University of Denmark Roskilde, pvol@dtu.dk

Abstract In this paper we compare three wind-farm parametrisations for mesoscale models against mast measurement data from the Horns Rev I offshore wind-farm. The parametrisations vary from a rotor drag method, to more sophisticated models. Additionally, we investigated the horizontal resolution dependence of the considered approaches.

5.1.1 Introduction

The offshore wind-farm technology has matured significantly in the past decade. The current largest installed wind farm, the London array phase I, with a nominal capacity of 630 MW, is almost four times larger than the Horns Rev I (160 MW) wind farm, which began to operate in 2005. The North Sea area, which is at the moment the most lucrative region for offshore wind farms, is however limited. Therefore it will become increasingly important to study the effect of large wind farms on the atmosphere from an economical (wind farm efficiency, wind farm interaction), as well as from an ecological point of view.

We use in this study the mesoscale model for its ability to take atmospheric conditions into account, which can influence the wake extension. A drawback is the lack in resolution compared to Computational Fluid Dynamics (CFD) models, implying that it is not possible to simulate single turbine wakes. Instead a wind farm parametrisation models the average effects of wind turbines inside a mesoscale grid cell.

Three wind farm schemes will be analysed. The first approach, hereafter ROTOR-DRAG, adds only a drag force to the flow, which is proportional to the turbine blade area intersection with the model grid level. The second parametrisation, hereafter referred to as WRF-WF, is included in the Weather Research and Forecast Model (WRF) (Skamarock et al., 2008), a publicly available open source model written in Fortran. It applies a drag and a Turbulence Kinetic Energy (TKE) source term to the flow at each rotor intersecting vertical grid level. The third wind farm scheme, Explicit Wake Parametrisation (EWP) (Volker et al., 2013), has been developed at the DTU Wind Energy Department.

Similarly to the other approaches, also in the EWP approach a drag force is added to the momentum budget. However, it accounts for the unresolved wake expansion. Here we assume that the unresolved wake expansion can be described by a turbulence diffusion process (Tennekes and Lumley, 1972; Wyngaard, 2010). The parametrisation has been implemented in the WRF model.

In a previous study Volker et al. (2013) we analysed the WRF-WF and EWP approach against long term measurements from the offshore wind farm Horns Rev I. We found that the additional TKE in the WRF-WF approach caused an intensive mixing zone, leading to a too fast velocity deficit recovery close to the wind farm. Furthermore, the scheme was found to be vertical resolution dependent, consequently the energy extracted from the flow varies with vertical resolution. In this article we extend that study by analysing the horizontal dependence of both parametrisations. This is done by simulating the same wind farm size with a 1.12 km, 1.68 km and 2.24 km horizontal resolution. We verify the wind farm parametrisations against long term in-situ measurements from the Horns Rev I wind farm. The mesoscale model was run in the idealised case mode with 40 vertical layers. The vertical resolution was in the planetary boundary layer (PBL) in the order of 10 m (the five lowest mass points were on 10, 30, 50 ,71 and 92 meters respectively).

5.1.2 Mesoscale Model

Mesoscale models are designed to forecast weather phenomena with typical length scales down to around 10 km. Therefore, to limit computational costs, a relatively coarse horizontal resolution in the order of kilometres is required. The model's vertical resolution is in the Planetary Boundary Layer (PBL) typically in the order of decametres to allow the vertical temperature and moisture structure to be resolved sufficiently. Mesoscale models are intended to resolve, similarly to Reynolds Averaged Navier-Stokes (RANS) models, only the mean flow, whereas the turbulence part of the spectrum is completely modelled. The basic assumption is that there is a scale separation between the resolved mesoscale processes and the unresolved turbulent ones, since no explicit filtering is applied. This means that the solution will not converge to the expected value with horizontal grid refinement, since from a certain horizontal resolution onwards, double counting will take place. Mesoscale models are generally non hydrostatic and fully compressible. This means that they contain a prognostic equation for each of the three wind velocity components and a complete continuity equation. Furthermore, they contain a prognostic equation for the temperature as well as for all moisture components. Finally, the pressure is obtained via the equation of state. The time step used in the prognostic equations is determined by the Courant number, which is a function of the advection velocity and the horizontal grid size. The lower boundary values are, over land, provided by soil (diffusion) models and over water they are generally obtained from reanalysis data.

Parametrisation of Wind Turbines

All unresolved processes need to be parametrised. Examples are local and non-local (convection) turbulent transport, turbulent surface fluxes, moisture phase changes and radiation. Since $D_0 \ll \Delta x$, where D_0 is the wind turbine diameter and Δx the horizontal grid spacing, the effect of wind turbines remain unresolved. On the other hand, since $D_0 > \Delta z$, where Δz is the vertical grid spacing, the vertical turbine-induced wake structure can be described. Due to the coarse horizontal resolution in mesoscale models, typically several turbines will be located within one grid-cell. It is therefore not possible to resolve single turbine wakes and hence the interaction between single turbines is not accounted for in the model. Instead the parametrisation should apply a grid cell averaged deceleration, accounting for the average impact of all the grid cells containing turbines. After that point, the mesoscale model is intended to simulate the wind farm wake. We aim of describing the grid cell average deceleration as accurately as possible, since the wake expansion within a mesoscale grid-cell is expected to be considerable. The energy extracted from a single turbine can be modelled by adding an additional force in the opposite flow direction to the velocity balance equation. For a compressible fluid, neglecting viscous effects, the most general form of the RANS equation reads

$$\frac{\partial U_i}{\partial t} + U_j \frac{\partial U_i}{\partial x_j} + \frac{\partial \overline{u_i u_j}}{\partial x_j} = F_i. \tag{5.13}$$

Here, we use capital letters for mean quantities and lower-case letters for the fluctuations. The index i represents the x, y and z direction. All the forcing contributions are incorporated in the force (per mass) term F_i on the right hand side, such as the pressure gradient force or Coriolis force. Also the turbine induced drag force, F_{D_i}, is part of the forcing term F_i.

Rotor Drag

In this approach, a drag force is applied to the horizontal components of Eq. (5.13) at every turbine blade intersecting model level k. The additional thrust force in the horizontal direction i reads

$$F_{D_i}(k) = -\frac{C_T\, N\, A(k)\, U_i(k)\, |U(k)|}{2\,(\Delta x)^2\, \Delta z(k)}, \tag{5.14}$$

where C_T is the thrust coefficient, N the number of turbines per grid cell, $A(k)$ the turbine blade area intersecting with model level k and $U_i(k)$ the horizontal wind velocity component in the direction $i = x, y$. The absolute horizontal velocity at the model level k is $|U(k)| = \sqrt{U(k)^2 + V(k)^2}$, where $U(k)$ and $V(k)$ are the horizontal velocity components in the x and y direction, respectively. Δx and $\Delta z(k)$ denote the horizontal and vertical grid spacing at level k. In this approach the sub-grid velocity deficit expansion in the vertical direction is neglected, since the vertical velocity deficit is restricted to the turbine blade tip to tip extension.

WRF-WF

The WRF-WF scheme is from version 3.2.1 included in the WRF model. This parametrisation applies the drag force Eq. (5.14), as well as an additional source term of TKE, to the flow. The total TKE applied to the model level k reads

$$\overline{u_i f_{D_i}} = \frac{C_e N \sum_k A(k) \, |U(k)|^3}{2 \, (\Delta x)^2 \, \Delta z(k)}. \tag{5.15}$$

Here we used C_e for the factor of proportionality, which is equal to $C_T - C_p$, where C_P is the power coefficient. The additional TKE will lead to an increased turbulence (diffusion) coefficient for momentum $K_m = q \ell S(m)$, where $q = \sqrt{2e}$ is the turbulence velocity, ℓ the turbulence length scale, e the turbulence kinetic energy and $S(m)$ a stability correction for momentum. In this way the vertical sub-grid-scale wake expansion is obtained implicitly.

Explicit Wake Parametrisation

In the EWP scheme it has been assumed that the directly turbine-blade-induced turbulence is small compared to the shear production in the wake flow. This can be justified, since the turbulence length scales of the turbine-induced turbulence are in the order of the turbine cord length and occur locally at the turbine. Whereas the entire wake flow is governed by shear production, with length scales of the atmospheric boundary layer. The downstream sub-grid scale velocity deficit development, at distances $x < \Delta x$, is described explicitly by a turbulence diffusion process.

The velocity deficit is assumed to be approximately Gaussian shaped and can be described by a length scale $\sigma(x)$, which determines the vertical extension of the velocity deficit and the maximum velocity deficit at the wake's centre, $U_s(x)$. The velocity deficit profile can be written as,

$$U_0 - \widehat{U} = U_s f, \tag{5.16}$$

where $\widehat{U}$ is the sub-grid scale velocity, U_0 the hub-height velocity and f a function that describes the shape of the velocity deficit. From the one dimensional diffusion equation, we can obtain the expression for the shape function,

$$f = \exp\left[-\frac{1}{2}\left(\frac{z-h}{\sigma}\right)^2\right] \pm \exp\left[-\frac{1}{2}\left(\frac{z+h}{\sigma}\right)^2\right], \tag{5.17}$$

and for the length scale

$$\sigma^2 = \left(\frac{2K}{U_0}\right) x + \sigma_0^2, \tag{5.18}$$

where σ_0 denotes the initial length scale, h the hub-height and K the turbulence diffusion coefficient at hub-height. The maximum velocity deficit U_s can be obtained from the total thrust equation. This gives

$$\frac{1}{2}\rho\, C_T\, \pi\, R_0^2\, U_0^2 = \rho \int_{\Delta y} \int_0^{z_{\max}} U_0\,(U_0 - U)\, dz dy = \rho \int_{\Delta y} dy \int_0^{z_m} U_0\, U_s\, f\, dz, \tag{5.19}$$

where ρ is the atmospheric density, R_0 the turbine blade radius, y the horizontal direction perpendicular to the flow and Δy the model grid spacing in the y direction. Inserting Eq. (5.17) in Eq. (5.19) and integrating it over the domain height $z_{\max}$ gives for the maximum velocity deficit

$$U_s = \sqrt{\frac{\pi}{2}}\, \frac{2\, C_T\, R_0^2\, U_0}{\Delta y\, \overline{\sigma}}. \tag{5.20}$$

Where $\overline{\sigma}$ is the grid-cell averaged length scale. The force per mass for the horizontal components becomes

$$F_{D_1}(k) = -\sqrt{\frac{\pi}{2}}\, \frac{C_T}{2\overline{\sigma}} \left(\frac{R_0\, U_0}{\Delta x}\right)^2 f(k)\, \cos\left[\varphi(k)\right] \tag{5.21}$$

and

$$F_{D_2}(k) = -\sqrt{\frac{\pi}{2}}\, \frac{C_T}{2\overline{\sigma}} \left(\frac{R_0\, U_0}{\Delta x}\right)^2 f(k)\, \sin\left[\varphi(k)\right]. \tag{5.22}$$

Here we denote the vertical levels by k. Eq. (5.21) and Eq. (5.22) are applied to the horizontal components of Eq. (5.13).

5.1.3 Measurement Data

For the model evaluation we use the measurements from the Horns Rev I wind farm, see Fig. 5.13. The Horns Rev I wind farm consists of 80 2 MW wind turbines, each with a blade diameter of 80 m and a hub at 70 m above sea level. The turbines are arranged in 10 columns from East to West and 8 rows from South to North. The turbine spacing is 560 m in the West to East direction. Two masts are installed to the East of the wind farm. The masts M6 and M7 are located 2000 m and 6000 m downstream, see Fig.(5.13). The masts contain cup anemometers at 70 m height A full description of the wind farm layout is given in Hansen (2012). For the model validation only measurements from the year 2005 to 2009 under neutral atmospheric conditions have been selected. The wind direction interval is from $255^\circ \leq \phi \leq 285^\circ$ and the wind speed interval from $7.5\,\mathrm{m\,s^{-1}}$ to $8.5\,\mathrm{m\,s^{-1}}$. The Northerly wind direction is defined to be at 0° and the rotation is in the clockwise direction. The neutral conditions are defined for Monin-Obukhov lengths $|L| > 500\,\mathrm{m}$.

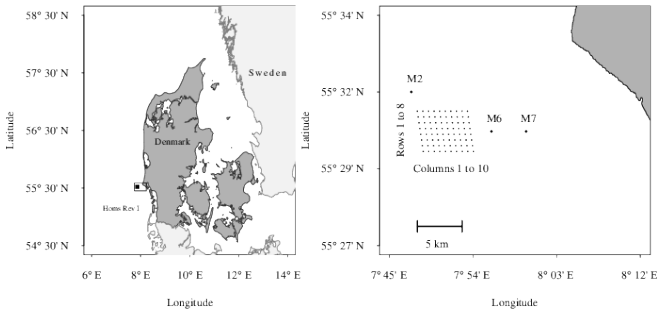

Figure 5.13: Location of the Horns Rev I wind farm and the meteorological masts.

5.1.4 Model Set-Up

We used the WRF model in idealised case mode with open boundaries and no surface heat fluxes. The model is initialised with a constant Geostrophic wind, which converges to $U = 7.97\,\mathrm{m\,s^{-1}}$ and $V = 0.09\,\mathrm{m\,s^{-1}}$ ($\phi = 269.4°$) at hub-height. In this model configuration the Coriolis force acts on the velocity perturbation from the initial condition. The dry atmosphere converges to a neutral temperature profile with an inversion height at around 700 m. The cloud micro-physics, as well as the convection scheme, were turned off. For all simulations the MYNN (1.5) PBL turbulence diffusion scheme Nakanishi and Niino (2009) has been used as required by the WRF-WF parametrisation. The model was set-up with 80×30 grid cells in the horizontal direction. In the vertical direction we used 40 layers. The lowest layers were at 10, 30, 50 ,71 and 92 m respectively. To study the horizontal dependence of the three wind farm parametrisations, we ran the WRF model with a 1120 m (R1120), 1680 m (R1680) and 2240 m (R2240) horizontal grid spacing, respectively. The model set-up is shown in Table 5.2. In the evaluation the velocities

Table 5.2: WRFV3.4 simulation set-up of the horizontal resolution study

	R1120	R1680	R2240
Grid points (nx,ny,nz):	$80 \times 30 \times 40$	$80 \times 30 \times 40$	$80 \times 30 \times 40$
Top (m):	10000	10000	10000
Horizontal grid spacing:	1120 m	1680 m	2240 m
Boundary condition:	OPEN	OPEN	OPEN
PBL scheme:	MYNN (1.5)	MYNN (1.5)	MYNN (1.5)
Coriolis:	TRUE	TRUE	TRUE

from a single model simulation are evaluated, against the wind direction averaged wind speed of the met masts.

Wind-Farm Layout

The wind farm's layout for the three simulations is depicted in Fig. 5.14. The number of turbines for all simulations is equal to 80, distributed in 8 rows and 10 columns. The number of turbine-containing grid-cells is 20, 12 and 6, for the R1120, R1680 and R2240 simulation, respectively.

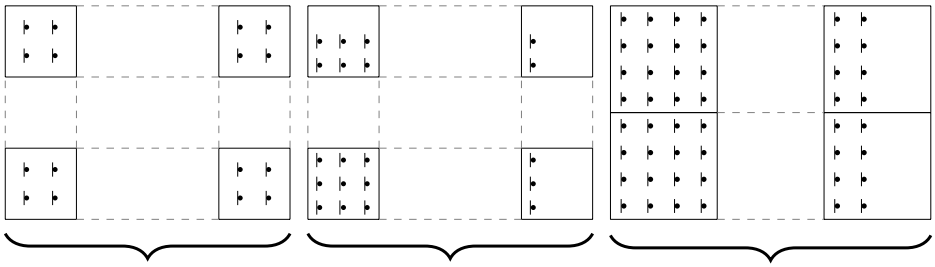

Figure 5.14: In this figure the different wind farm layouts are plotted. From the left side to the right side we plotted the wind farm layout for the R1120, R1680 and R2240 simulation.

We use the dotted lines for the grid cells with an unchanged turbine density. The turbine density per grid-cell is constant in the R1120 simulation. However, it is not constant for the R1680 and R2240 simulations.

Wind-Farm Scheme Adjustments

WRF-WF scheme

The WRF-WF scheme uses by default an empirical power curve for obtaining the power coefficient C_P. The thrust coefficient is afterwards derived by the empirical relationship $C_T = \min(7C_p/4, 0.9)$. To guarantee a scheme independent thrust, we use the thrust coefficient from the Vestas V80 thrust curve as in the EWP scheme. Thereafter, the inverse relationship from above is applied to obtain the power coefficient, $C_p = C_T/1.75$. In this way the ratio between the thrust and power coefficient remains unchanged in the WRF-WF parametrisation.

EWP scheme

The initial length scale has been set to $\sigma_0 = 1.5\,R_0$. Here we included viscous effects and vertical meandering to the inviscid fluid solution $\sigma_0 = R_0$.

5.1.5 Wind Farm Evaluation

In the next section we evaluate the model hub-height velocity field for the different approaches and horizontal resolutions, against the wind direction averaged velocities obtained from cup anemometers mounted at 70 m. Thereafter, we analyse quantitatively the horizontal resolution dependence of the modelled wind farm wake velocity field. In this study we use the near and far wind farm wake for a 10% and 5% velocity reduction, respectively. This definition was made for terminology convenience only.

Near Wind-Farm Wake

In Fig. 5.15 we show the normalised hub-height velocity for the three approaches. The

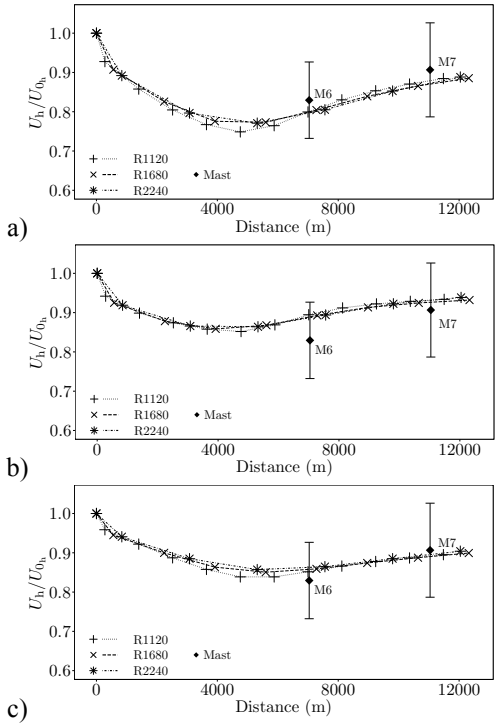

Figure 5.15: Normalised velocity, U_h/U_{0_h} recovery plot for the ROTOR-DRAG, WRF-WF and EWP scheme. The mast measurements are represented by the diamonds. a) ROTOR-DRAG, b) WRF-WF and c) EWP approach. Here U_h stands for the downstream hub-height velocity and U_{0_h} for the reference velocity at hub-height. The bars represent the standard deviation σ of the measurements.

normalised velocity within the wind farm has been obtained by averaging over all turbine containing grid-cells in the cross-stream direction, i.e. for the R1120, R1680 and R2240 simulation we averaged over 4, 3 and 2 rows respectively (Fig. 5.14). Figure 5.15 shows the normalised velocity field for the ROTOR-DRAG, WRF-WF and the EWP approach. Fig. 5.15a shows in the wind farm wake a low bias for the modelled normalised velocity compared to the long-term averaged measurements. Furthermore, the velocity is shown to be horizontal grid-size dependent. The hub-height velocity fields for the R1680 and R2240 simulations are similar. Whereas the velocity field for the higher resolution run shows a slightly lower normalised velocity field at the end of the wind farm, at a distance of around 5000 m and a higher normalised velocity in the near wind farm wake. The maximum difference in normalised velocity is 3% at the end of the wind farm, at mast 7 the difference between the simulations is reduced to less than 1%. Fig. 5.15b, shows a positive bias for the simulated normalised velocity at hub-height for the WRF-WF approach, compared to the measurements. We notice also that the velocity field is less sensitive to a variation in horizontal resolution. Similarly to the ROTOR-DRAG approach, the velocity fields for the lower resolution runs are almost identical within the wind farm and in the near wake. The velocity field with the higher horizontal resolution is again slightly lower within the wind farm and slightly higher closely after mast M6. The differences are always less than 1%. Figure 5.15c shows for the EWP approach a higher modelled normalised velocity at mast M6 and a slightly lower one at mast M7.

For the EWP scheme, the velocity deficit increases with an increase in the resolution within the wind farm. Between M6 and M7 the velocity fields become horizontal resolution independent. The difference in normalised velocity between the R1120 and R2240 simulation is slightly higher at the end of the wind farm.

Wind-Farm Wake

In Fig. 5.16, Fig. 5.17 and Fig. 5.18, we show the normalised velocities at hub-height for the ROTOR-DRAG, WRF-WF and EWP approaches, respectively. The velocity from the wind farm simulation is again normalised by the velocity from the reference simulation. We show always from the top to the bottom panel, the results from the R1120, R1680 and R2240 simulations.

ROTOR-DRAG Approach

The near wake extends to around 7 km downstream in all simulations,whereas the far wind farm wake extension becomes resolution dependent. This results from the decreasing wake width in the cross-wind direction, which can not be resolved anymore with a lower model resolution.

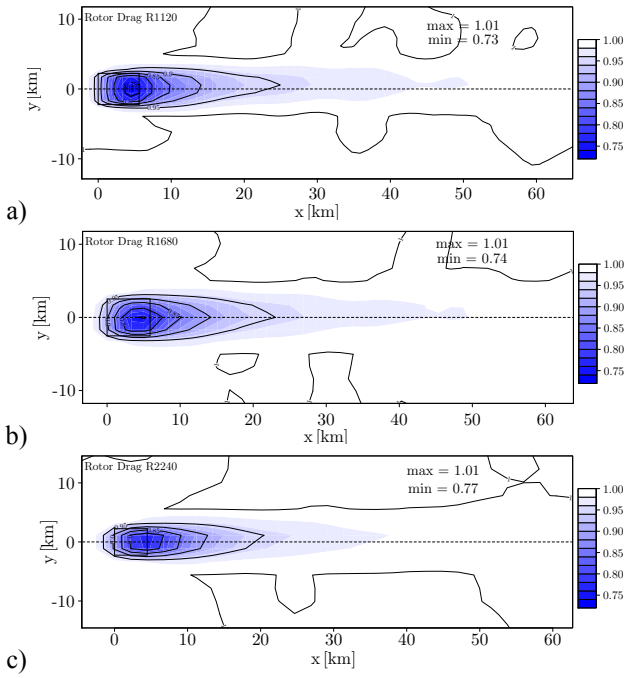

Figure 5.16: Velocity deficit recovery plot for the ROTOR-DRAG approach. For the R1120, R1680 and R2240 simulation respectively.

WRF-WF Scheme

In Fig. 5.17, where the normalised velocity for the WRF-WF has been plotted, we see that the near wake velocity reduction varies almost 40% (around 1.7 km in the R1680 run and around 2.8 km in the R2240 simulation). Although the maximum velocity reduction in the WRF-WF approach is around 15%, which is around 10% less than with the ROTOR-DRAG approach, the wind farm induced wake extends further downstream for the WRF-WF approach. This implies that the velocity restoring mechanisms differ for both approaches. Similarly to the results from the ROTOR-DRAG approach, the wake width in the far wake is not resolved anymore in the lower resolution simulations.

EWP Scheme

Fig. 5.18 shows that the near wake extension varies by circa 6%, between the R1120 and R2240 simulation (around 8.0 km in the R1120 compared to 7.5 km in the R2240). The contour lines for a 2% velocity reduction are almost identical to those one of the WRF-WF scheme. The wake orientation differs however, see Volker et al. (2013).

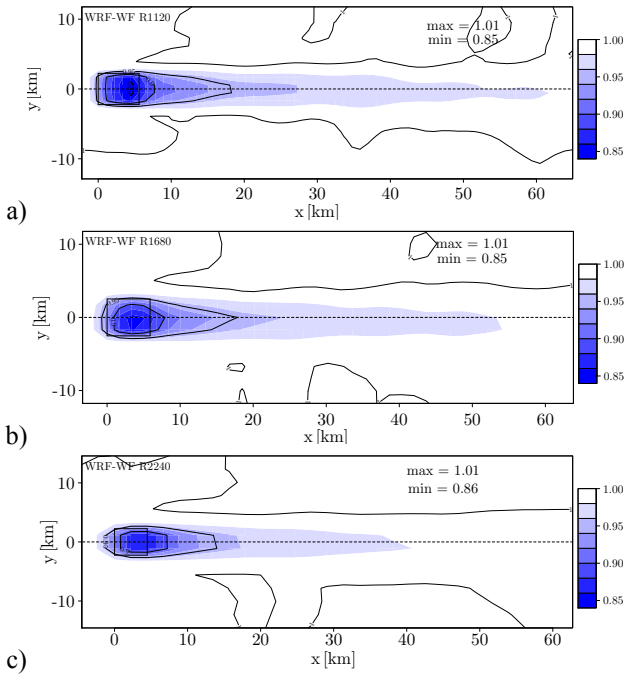

Figure 5.17: Identical to Fig. 5.16, this time for the WRF-WF approach

5.1.6 Discussion & Conclusion

We analyse three wind farm approaches (ROTOR-DRAG, WRF-WF and EWP) against long term averaged measurements from Horns Rev I.

For the near wind farm wake, Fig. 5.15, we found that compared to mast measurements the velocity reduction was overestimated in the ROTOR-DRAG approach and underestimated in the WRF-WF approach. For the EWP approach we found an underestimation of the velocity reduction at mast M6, 2000 m downstream from the wind farm and a slightly overestimated velocity reduction at mast M7, 6000 m downstream. Furthermore, we found that the ROTOR-DRAG approach was the most sensitive to the horizontal resolution variation within the wind farm. The near wake extension was however almost horizontal resolution independent. The EWP scheme is shown to be sensitive to a horizontal resolution variation within the wind farm (1% difference). In the wind farm wake, between M6 and M7, the normalised velocity converged. The near wake extension varied around 6% between the R1120 and R2240 simulation. The horizontal resolution sensitivity within the wind farm was the smallest for the WRF-WF. However, the near

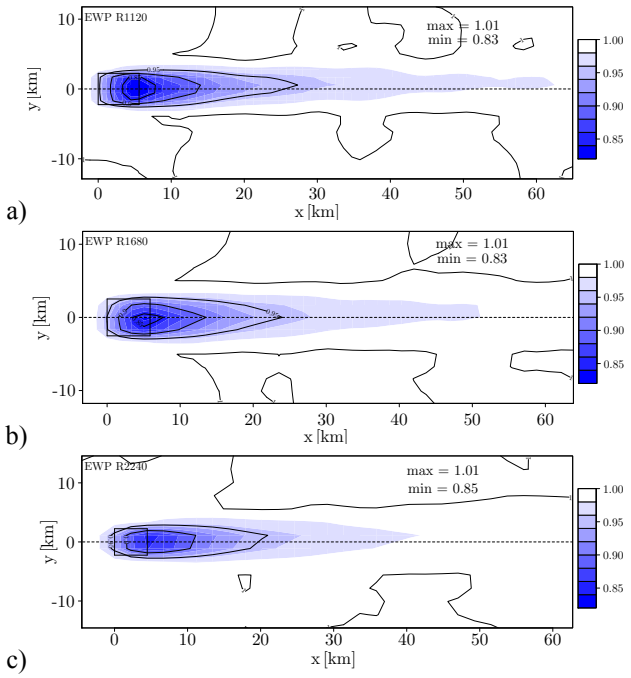

Figure 5.18: Identical to Fig. 5.16, this time for the EWP scheme

wind farm wake extension differed by around 40% between the R1680 and R2240 simulation. Regarding the far wake extension, we found that the wake width in the horizontal cross-stream direction becomes too small to be resolved with a decreasing horizontal resolution. This leads to a reduced wind farm wake extension in the R2240 simulation for all the schemes.

6

Interaction between Wind Farms and the Lower Atmosphere

In Chapter 5, we evaluated the EWP and WRF-WF parametrisation. In this chapter we use these wind farm parametrisations to analyse the interaction between a hypothetical large offshore wind farm and the lower atmosphere. In Sect. 6.1, a wind farm simulation with the EWP parametrisation is performed in the northern California area, where high persistent wind speeds along the coast are observed. The findings from that simulation are used in Sect 6.2, in which the velocity recovery mechanisms for different atmospheric conditions are analysed for the EWP and WRF-WF parametrisation.

6.1 Lower Marine Atmosphere Response to a Large Offshore Wind Farm

6.1.1 Introduction

Electrical power generation through renewable energy resources is expected to play an increasingly important role in the near future. The power generation from wind energy, one of the major contributors to renewable energy resources, increased exponentially in the last decades and it is predicted to keep growing. Whereas two decades ago commercial wind turbines had rated capacities still below 1 MW, currently trial turbines have a nominal capacity of over 7.5 MW. In Europe, for example, the contribution from offshore wind farms to the total power production has increased significantly in the past decade.

Offshore power production offers several advantages compared to those onshore. This, since offshore winds are generally higher and more steady and the turbulence intensities are lower, which potentially leads to increased production and longer turbine lifetimes. However, offshore wind farms have still higher installation and maintenance costs. According to BTM Consult, a part of Navigant consulting, the total installed capacity in the North-Sea area will be above 24 GW in 2017, compared to 4.8 GW in 2013. Furthermore, according to the Chinese Renewable Energy Industries Association, China expects to expand their offshore wind energy production to 30 GW by 2020. The largest currently installed wind farm in the North-Sea, the London array, has in its phase I a nominal capacity of 630 MW, using 175 turbines with a rated capacity of 3.6 MW. After

finishing the final phase the London array will have a nominal capacity of 1.2 GW. It is expected that the knowledge gained from such large projects, leads to more efficient offshore wind farm layout. In the United States, the State of California has the ambition to increase the contribution of renewable energy in the coming 30 years. Although no offshore wind farms are installed along the Californian coast yet, the excellent wind conditions provide a high potential for power production through offshore wind energy. The high wind speeds along the northern California coast were simulated in a numerical study by Dvorak et al. (2010). To the South of point Arena the averaged model wind speed at 80 m height was above 8.5 $\mathrm{m\,s^{-1}}$. However, the northern California coastal region is also known for its complex ecosystem, where persistent along-shore winds cause upwelling of nutrient rich, deep water. The cold Sea Surface Temperature (SST) in turn is associated with persistent anti-cyclonic conditions and determines the strength of the inversion, which caps the Marine Boundary Layer (MBL). In this study we investigate in which way this environment is affected by the presence of a large wind farm and vice versa how these conditions affect the flow around the wind farm.

For this study we use the Weather Research and Forecast mesoscale model for the wind farm simulation. The wind farm, with a 1.4 GW rated capacity, is located to the North of the San Francisco Bay area. A mesoscale model is used for the analysis, since it allows to simulate large areas with reasonable computation costs. For the analysis we simulate a complete year to account for the atmospheric effects of a complete annual cycle. From this simulation we find a smaller velocity reduction for the annual averaged velocity field for along-shore wind conditions compared to that of considerable smaller wind farms with the same turbine spacing (Barthelmie et al., 2010; Hansen, 2013). Additionally, we notice within the MBL, decreased temperatures and increased water vapor contents. For the most frequent, along-shore, wind direction the advection of the velocity, temperature and moisture anomalies reaches the Gulf of the Farallones. Furthermore, the wind farm induced gravity waves, cause velocity, temperature and moisture anomalies to extend within the lower troposphere.

In Sect. 6.1.2 we introduce the wind farm scheme, that parametrises the turbine-induced velocity reduction which is unresolved by the mesoscale model. In Sect. 6.1.2 the model set-up is given. In Sect. 6.1.3, we evaluate the results of the simulation, against buoy measurements and QuikSCAT satellite data. At the end of Sect. 6.1.3, the modelled wind conditions for the wind farm site are evaluated. In Sect. 6.1.4, the influence of the wind farm to the MBL and the lower troposphere, up to around 3 km, is studied. We examine first the annual effects and establish thereafter the findings in a case study.

6.1.2 Experimental Design

Wind farm parametrization

In this study the Explicit Wake Parametrization (EWP) is used to account for the effects of the wind farm. A complete description is found in Volker et al. (2013). In the approach wind turbines are treated as drag devices that execute a force to the opposite horizontal wind direction. In the parametrization we assume 1) that the grid cell pressure field is on average uninfluenced by the wind turbine (Ainsley, 1988) and 2) that on a several kilometre average, the shear-induced turbulence will dominate over the turbine blade induced turbulence. On the other hand, the sub-grid scale turbine wake development is not neglected and is stability dependent parametrised.

From the grid-scale averaged turbine induced wake, we obtain the average drag force, which is then applied to the Reynolds averaged Navier-Stokes equations

$$\frac{\partial U_i}{\partial t} + U_j \frac{\partial U_i}{\partial x_j} + \frac{\partial \overline{u_i u_j}}{\partial x_j} = -\frac{1}{\rho}\frac{\partial P}{\partial x_i} - \varepsilon_{i3k} f U_k - \delta_{i3} g + F_{D_i}. \tag{6.1}$$

Here we use capital letters for the averages, i.e. $U(\mathbf{x},t)$ for the velocity, $P(\mathbf{x},t)$ for the pressure and $F_{D_i}(\mathbf{x},t)$ for the turbine-induced force and lower-case letters for the fluctuations. The atmospheric density is described by $\rho(\mathbf{x},t)$, the gravitational acceleration constant by g and the Coriolis frequency by f. Furthermore, the Kronecker delta is denoted by δ_{ij} and the Levi-Civita symbol by ε_{ijk}. The index $i = x,y,z$ stands for the x, y and z direction. The approach follows the classical wake theory from Tennekes and Lumley (1972) and Wyngaard (2010). Due to the large horizontal grid-spacing, Δx, we expect the turbine-induced wake to expand in the vertical direction within the grid-cell. We describe the unresolved wake expansion by a turbulence diffusion process, which is governed by a single turbulence diffusion coefficient K at hub-height. The wake, or velocity deficit, is expressed by the velocity deficit at the wake's centre times a function that describes the wake's shape in the vertical direction, $U_0 - \widehat{U} = U_s f$. Here, U_0 is the hub-height velocity, $\widehat{U}(x,z)$ the sub-grid scale velocity, $U_s(x)$ the maximum velocity deficit at the wake's centre, $f(\sigma,z)$ the shape function and $\sigma(x)$ the length scale, which is a measure of the vertical wake extension. The downstream distance from the turbine is denoted by $x < \Delta x$. From the turbulence diffusion equation the shape function,

$$f = \exp\left[-\frac{1}{2}\left(\frac{z-h}{\sigma}\right)^2\right] \pm \exp\left[-\frac{1}{2}\left(\frac{z+h}{\sigma}\right)^2\right], \tag{6.2}$$

and the equation for the length scale,

$$\sigma^2 = \frac{2K}{U_0}x + \sigma_0^2, \tag{6.3}$$

can be obtained. In Eq. (6.3) we use σ_0 for the initial length scale. Equation (6.2) and Eq. (6.3) describe the ensemble averaged velocity deficit profile at any distance x. We apply a grid-cell averaged velocity deficit to Eq. (6.1). To a good approximation this is achieved by averaging the length, σ, over the grid-cell and apply it in Eq. (6.2). The unknown maximum velocity deficit, is obtained by equating the total thrust to the momentum deficit. This gives

$$U_s = \sqrt{\frac{\pi}{2}} \frac{C_T R_0^2 U_0}{2 \Delta y \, \overline{\sigma}}, \tag{6.4}$$

where Δy denotes the width of the wake, $C_T(U_0)$ the thrust coefficient, R_0 the rotor radius and $\overline{\sigma}$ the grid-cell averaged length scale. In models with $\Delta x = \Delta y$, the decelerations that are applied to Eq. (6.1), become

$$F_{D_x}(k) = -\sqrt{\frac{\pi}{2}} \frac{C_T}{2\overline{\sigma}} \left(\frac{R_0 U_0}{\Delta x} \right)^2 f(k) \, \cos(\varphi(k)) \tag{6.5}$$

and

$$F_{D_y}(k) = -\sqrt{\frac{\pi}{2}} \frac{C_T}{2\overline{\sigma}} \left(\frac{R_0 U_0}{\Delta x} \right)^2 f(k) \, \sin(\varphi(k)), \tag{6.6}$$

where $f(k)$ stands for the discrete function of Eq. (6.2), $\varphi(k)$ for the wind direction and k for the model mass-levels. The initial wake extension, σ_0, has been set to one and a half times the rotor radius and the wind turbines are assumed to be placed in the centre of the grid-cell, the wake is expected to extend over half a grid-cell.

WRF Model (Set-up)

For this study the Weather Research and Forecast (WRF) model Version 3.4 (Skamarock et al., 2008) has been used. We simulate the atmospheric conditions for a complete calendar year to examine the wind farm influence on the Marine Boundary Layer (MBL). 2009 was chosen because of the availability of satellite and buoy measurement data. For the simulations the model is initialised once and thereafter only forced by conditions at the lateral and lower boundaries. For the initial and lateral boundary conditions, as well as for the sea surface temperature (SST), the North American Regional Reanalysis (NARR) data-set is used (Mesinger et al., 2006). The data is provided in a 3 hourly interval on an approximately 32 km Northern Lambert Conformal Conic grid. The SST is kept constant for the entire period of the simulation. Due to upwelling of deep cold water its annual variation is low at the wind farm location (around 4 K).

The model layout consists of a main domain and a single nested domain. The outer domain with a 6 km grid spacing (domain I) serves to capture synoptic scale events and to realise a flow relaxation from the boundary data region with a course spatial resolution towards the inner domain (domain II), which is used for the wind farm simulation. In

the inner domain we use a 2 km horizontal grid spacing. To ensure that the inner domain is large enough to cover the entire wind farm wake, it covers 422×440 km in the x and y direction. The outer domain, which includes the entire Californian coast, covers 1200×1620 km. Fig. 6.1a shows the geographic extension of both model domains. We used 60 vertical levels to simulate the vertical structure of the wind farm induced wake and the inversion layer structure. 25 levels are located within the lower 500 m and 44 levels up to 3 km. To minimise the computational costs, we run a simulation of domain

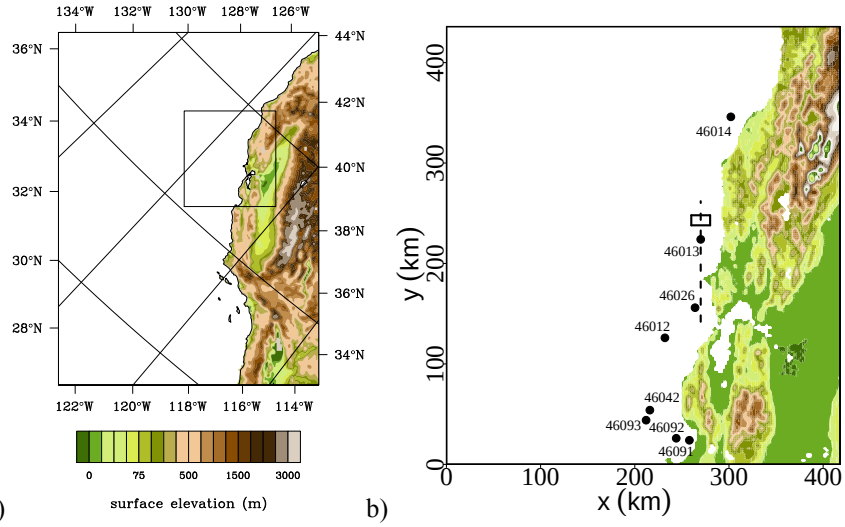

Figure 6.1: a) Nested domains used for the simulations. b) Map of the model domain II. The wind farm is indicated by a rectangle. The buoys used for the verification are represented by solid circles.

I once. For this domain only the wind speeds are nudged towards the NARR reanalysis data for all vertical levels, with the recommended coefficients. Although the 6 km horizontal resolution might be on the limit for the use of a convection scheme, it is not expected that over the cold ocean convective events are triggered often. The boundary conditions for domain II are determined from the output (every 3 hours) of the outer domain I. Thereafter, a simulation for domain II is run twice, with and without the wind farm. The later simulation defines the background state. The output of domain II is hourly. The model configuration is shown in Table 6.1.

The hypothetical wind farm contains 200 wind turbines with a rated capacity of 5 MW. The turbine hub-height is at 125 m and the turbine blade diameter, D_0, is 126 m. The wind farm contained 10 turbines along the direction of the coast and 20 turbines perpendicular to it. In the simulations we used the turbine thrust curve from a typical horizontal-axis wind turbine with a lower rated power. The turbine spacing is 1 km, which is slightly

Table 6.1: Table siting the WRF set-up used for the simulations.

Option	Domain I	Domain II
Grid points (nx,ny,nz):	200, 270, 60	211, 220, 60
Horizontal grid spacing (km):	6	2
Domain size (km × km):	1200×1620	422×440
PBL:	(Nakanishi and Niino, 2009)	same as I
Surface:	MYNN Surface	same as I
Convection:	(Kain, 2004)	-
Microphysics:	(Lin et al., 1983)	same as I
Long wave radiation:	(Mlaver et al., 1997)	same as I
Shortwave radiation:	(Dudhia, 1989)	same as I
Land-surface:	(Chen and Dudhia, 2001)	same as I
Nudging of U and V	Yes	No

larger than the turbine spacing of $7\,D_0$ at Horns Rev I, a Danish offshore wind farm. In this way, the wind farm extends over 50 grid cells, each one containing 4 wind turbines. The wind farm was positioned near to the Stillwater Cove, between point Arena and point Reyes. The wind farm is indicated by the rectangle in Fig. 6.1. The ocean within the wind farm area is not deeper than 80 m. This is quite deep, however, it still allows building the turbines on structures. The chosen region provides very good wind conditions according to the power density analysis made by Dvorak et al. (2010).

6.1.3 Evaluation of the Reference Simulation

Evaluation against point-scale observations

In Fig. 6.1b the locations of the selected National Oceanic and Atmospheric Administration's (NOAA) buoys are shown along with the buoy number. The extension of the wind farm is marked by a square. The dashed line indicates the horizontal extent of a cross-section used in the wind farm analysis in Sect. 6.1.4. Buoy nr. 46091, 46092 and 46093 are owned by the Monterey Bay Aquarium Research Institute (MBARI) and are equipped with cup anemometers 4 m above the sea level. Whereas, buoy nr. 46012, 46013, 4604, 46026 and 46042 are owned by the National Data Buoy Center (NDBS) and have their cup anemometers installed at 5 m above sea level. The air temperature is measured at a height of 3 and 4 m and the sea temperature at 0.6 m below the sea surface. We assumed that the water up to a few meters below the sea surface is well mixed and hence the sea temperature at 0.6 m to be comparable to the SST. The 10 min. averaged buoy data were obtained from the historical data set provided by the NDBS.For the average wind speed analysis, we use the model surface layer scheme (MYNN surface)

formulation, to calculate the wind speed on the respective buoy anemometer height. Due to expected local homogeneous surface conditions we compare the buoy measurements always to the nearest model grid cell. A model result is only considered if a measurement for that time-step is registered.

In Fig. 6.2a we use a quantile-quantile plot to compare the observed and modelled velocity distributions. The two velocity distributions are identical, when the dots lie on the diagonal (indicated by the dashed line). It shows that that the modelled and mea-

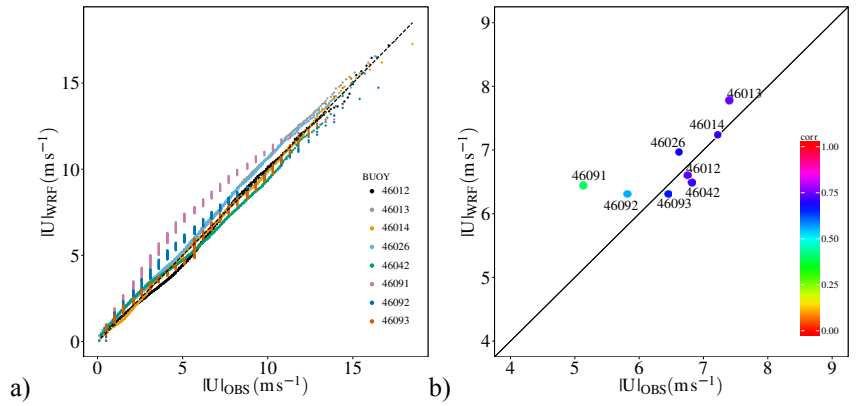

Figure 6.2: a) A quantile-quantile plot of the wind velocity considering all buoys. The abscissa represents the observed wind velocity and the ordinate the modelled wind velocity. b) A scatter plot, where the abscissa and ordinate are used for the mean observed and modelled velocity, respectively. The time correlation between measurements and the model is indicated by the colour.

sured velocity distributions are similar. An exception is buoy 46091. At this buoy the model overestimates the low wind speeds. Fig. 6.2b shows the mean modelled wind speed against the measured wind speeds. The averaged model wind speeds generally agree with the buoy measurements. The ratio between the average observed and modelled wind speed is in 7 out of 8 cases less than 6%. Buoy nr. 46091, located within the Monterey bay, is an exception. Here the average wind speed is overestimated by more than 1 meter per second and the correlation is low (0.4). Within this bay the model is not able to account for the local weather phenomena. The simulated wind direction was mainly along-shore in the South-East direction, whereas the observations show that the buoy was additionally influenced by land sea circulation systems (not shown).

Evaluation against remote-sensed data

The QuikSCAT satellite product is used for a spatial evaluation of the WRF reference run. The satellite images represent a 10 m wind speed, derived from the back-scatter,

assuming neutral conditions (Risien et al., 2011). The raw QuikSCAT RMSE is 2 $\mathrm{m\,s^{-1}}$. For the WRF model an equivalent neutral wind speed has been derived from the friction velocity, $u_\star$, and the roughness length, z_0, with the logarithmic wind profile assumption. We assume that QuikSCAT wind speeds represent an average in a $0.1^\circ \times 0.1^\circ$ cell. Therefore, the WRF wind speeds are downscaled to the QuikSCAT data grid. We select only model data further than 10 km away from the coast and its lateral boundaries, since the increased high frequency energy in near shore locations is not captured by the QuikSCAT data (Pickett et al., 2003). Model data is only considered if QuikSCAT data was available for the same time. Fig. 6.3 compares the model derived wind speeds, with those of QuikSCAT. Fig. 6.3a and Fig. 6.3b show respectively the mean wind speed for the

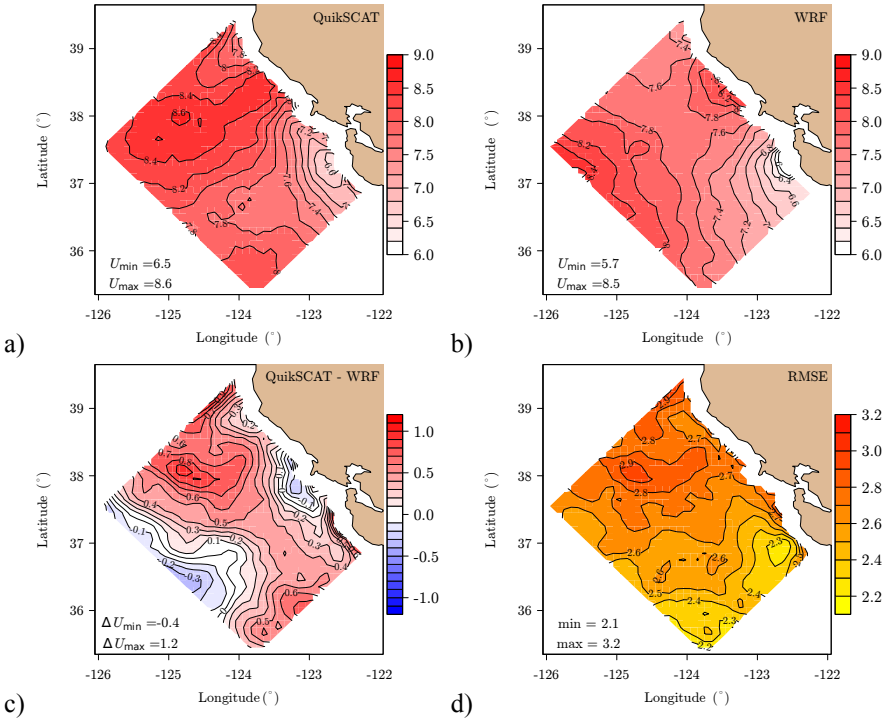

Figure 6.3: Annually neutral mean wind speed at 10 m for a) the QuikSCAT satellite data and b) the WRF simulation c) Difference between WRF and QuikSCAT wind speed, d) RMSE of the wind speed.

QuikSCAT data and WRF model, whereas Fig. 6.3c displays the velocity difference between the QuikSCAT data and the model, finally Fig. 6.3d shows the velocity's RMSE. Fig.6.3a and Fig.6.3b, show that the wind speed pattern in the Gulf of the Farallones (37°48′ N, 123°00′ W) to the West of the San Francisco Bay is simulated well. Fig.6.3c

shows generally a low bias between the model and the observations. Moreover, the model was able to simulate the velocity reduction in the wake of point Reyes (37°59′ N, 123°01′ W). However, to the North-West of the Gulf of the Farallones, in the deep ocean waters the annual SST variation is expected to be slightly larger. In this region the model seems not to be able to simulate the high wind speed pattern, which could be caused by the SST variation present in the satellite data. The underestimation in the WRF model of up to 0.8 m s^{-1} in this region.

Wind Farm Conditions

In this section the near surface wind velocity field near to the wind farm location is analysed. Therefore, the wind rose from buoy 46013 is compared to the model wind rose interpolated to 5 m height using the model surface layer scheme's formulation.

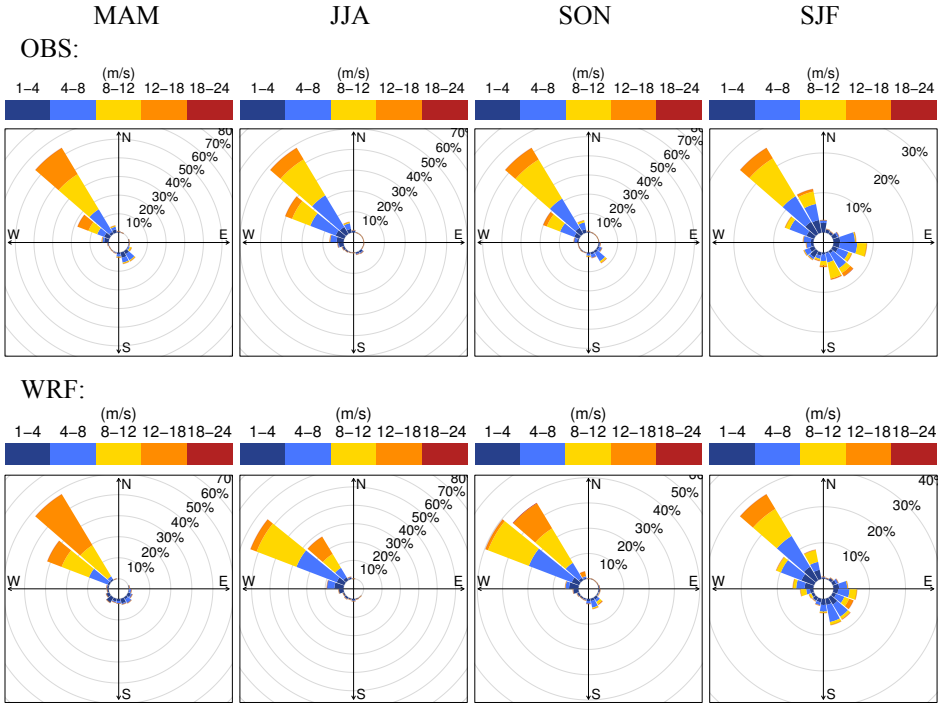

Figure 6.4: a) Wind rose from the winds measured at buoy 46013. In the top figures measured wind roses are shown and in the bottom the simulated ones. MAM stands for the period from the first of March to the end of May, JJA from the first of June to the end of August, SON from the first of September to end of November and DJF from the first of November 2009 to February 2009.

In Fig.6.4, the model and measurement-derived wind roses are shown for the four periods, indicated by MAM, JJA, SON and SJF. From the beginning of March to the end of November very persistent along-shore wind speeds are observed. In the periods JJA and SON along-shore winds are observed more than 50% of the time and in the first period this rises to almost 60%. These along-shore wind speeds are caused by the interplay of a semi-permanent high pressure over the North Pacific ocean, the blocking effect of the coastal orography, coastal jets and the coastal upwelling of deep ocean water. Due to coastal upwelling the annual SST variation is very low along the coast. Whereas larger SST fluctuations occur in the Pacific ocean further offshore in the absence of upwelling. In the winter months, when the high pressure area moves southwards, the wind direction variation increases. The persisting along-shore wind speeds that occur most of the year are extremely suitable for wind energy production. Firstly, since a low variation in electricity production is guaranteed for these steady wind conditions and secondly the small wind direction variation allows for an optimal wind farm layout for which wake effects are reduced. Figure 6.4 shows that the model is capable to simulate the wind direction and the wind speeds as observed.

6.1.4 Results

Local Effects

In Fig.6.5 we show the wind farm area averaged profiles of the changes in wind velocity, $|U|$, turbulence kinetic energy (TKE), potential temperature, θ and water vapour mixing ratio, Q_v. The wind farm averaged boundary layer height, H_{pbl}, is indicated by a horizontal solid and dashed line for the reference and wind-farm run, respectively. In the WRF model, the boundary layer height is a PBL scheme dependent diagnostic variable. In the MYNN scheme it is obtained via a weighted average of the height at which I) a minimum TKE value is reached and II) a potential temperature threshold is exceeded. Fig. 6.5a indicates a wind farm averaged velocity reduction at hub-height, $(1-|U|_{\mathrm{WF}}/|U|_{\mathrm{REF}})$, of around 6%. Here $|U|_{\mathrm{WF}}$ and $|U|_{\mathrm{REF}}$ are used for the velocity from the wind farm and reference simulation, respectively. The velocity reduction regions extend to around 500 m height, followed by a 1.5 km deep layer with a velocity surplus. In Fig. 6.5b, we notice that TKE decreases below and increases above hub height due to a decrease and increase in turbulence shear. The influence of the wind farm on the vertical mixing decreases exponentially with the height. In Fig. 6.5c and Fig. 6.5d we see that the inversion layer within the wind farm becomes on average around 0.1 K colder and 0.02 $\mathrm{g\,kg^{-1}}$ moister than in the reference run. Above the inversion the opposite happens, this time with reduced differences. We notice also the un-smooth character of the water vapour, which is due to phase transitions. The annual averaged boundary layer height over the wind farm does not change significantly. The wind farm averaged boundary layer height is 429 m in the reference simulation and it increases to 436 m.

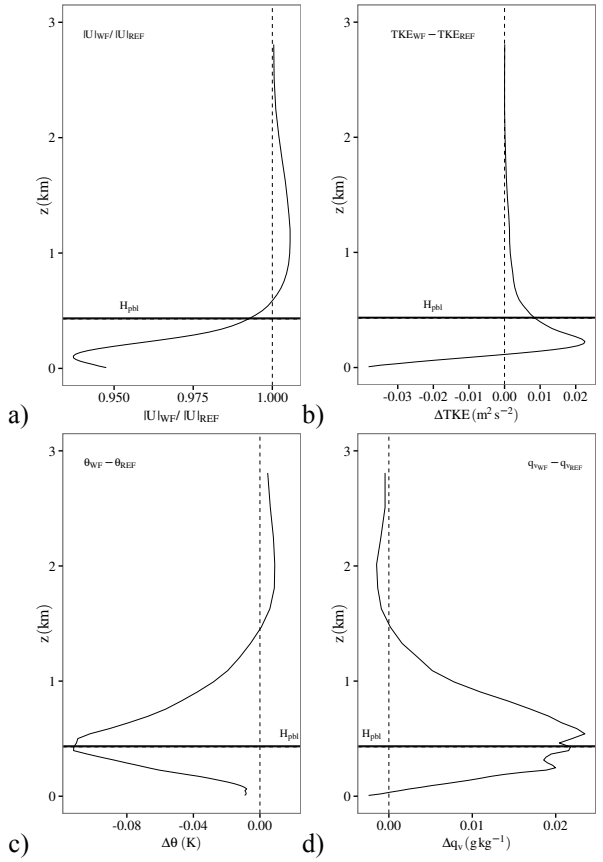

Figure 6.5: Annual and wind farm averaged profiles of the: a) normalised velocity, difference of b) turbulence kinetic energy, c) potential temperature, d) water vapour mixing ratio. The model boundary layer height, H_{pbl}, is indicated with a horizontal line.

Non Local Effects

We analyse the wind farm influence on the surrounding MBL for the most dominant North-West flow direction (Fig. 6.4). In the following we use a cross-section in the x, z plain, which is referred to as the wind farm cross-section. Its horizontal extension is indicated with a dashed line in Fig. 6.1. Atmospheric variables are only considered for wind directions between 270° and 274°. In the simulations this wind direction interval occurs more than 12% of the time and around 92% of the cases are between March and November.

Fig. 6.6 shows the averaged hub-height velocity for the wind farm simulation, $U_{h_{\mathrm{WF}}}$, (blue line) and the reference simulation, $U_{h_{\mathrm{REF}}}$, (red line) as well as their ratio (green line). The wind farm extension is marked by the vertical dashed lines.

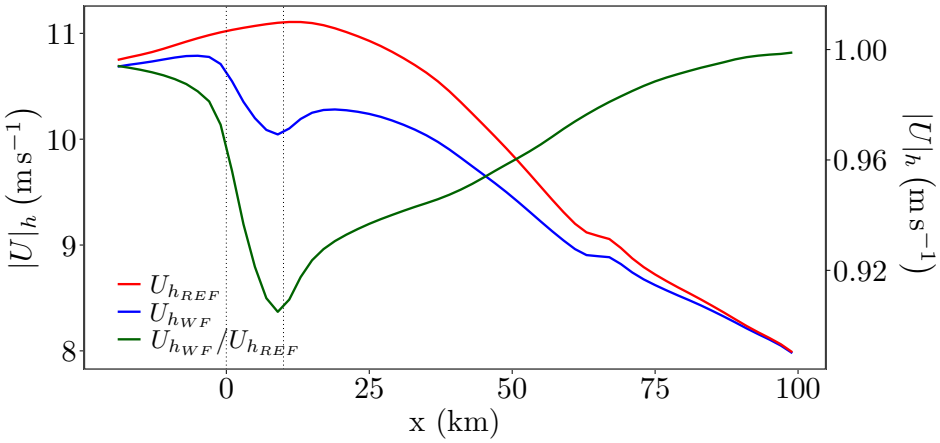

Figure 6.6: Hub-height velocity field in the wind farm wake as a function of the downstream distance along the dashed line in Fig. 6.1. The velocity field from the wind farm and reference simulation are represented by the red and blue lines, respectively. The normalised velocity is indicated by the green line. The wind farm extension is marked by the vertical dashed lines.

The slowing-down of the wind speed, due to the blocking effect of the downstream land is visible from the wind farm location onwards. At around 65 km downstream the influence of Point Reyes is found. The background velocity field reaches around 11 m s^{-1}at the wind farm location for the selected wind directions. The wind farm induces a velocity reduction of almost 4% upstream of the wind farm. Within the wind farm the reduction increases to around 10% at the end of the wind farm. The modelled velocity reduction of around 5% is considerably smaller than in smaller wind farms with a similar turbine diameter spacing. The long term velocity reduction at the Horns Rev I wind farm in the North Sea is for an average wind speed of 8 ± 0.5 m s^{-1} more than 15% at the end of the wind farm (Volker et al., 2013). Reasons for the higher wind farm efficiency could be the larger negative pressure gradients within the wind farm (Smith, 2009), the slightly larger spacing compared to Horns Rev I and the thrust coefficient which was high and constant for the selected wind speed interval at Horns Rev I, whereas it was in this simulation on average 8% lower and it varied. The wind farm induced wake with a 2% reduction extends around 60-70 km, a similar wake extension was simulated for the Horns Rev I wind farm (Volker et al., 2013).

Figure 6.7 shows the change in velocity, temperature, water vapour and TKE for the

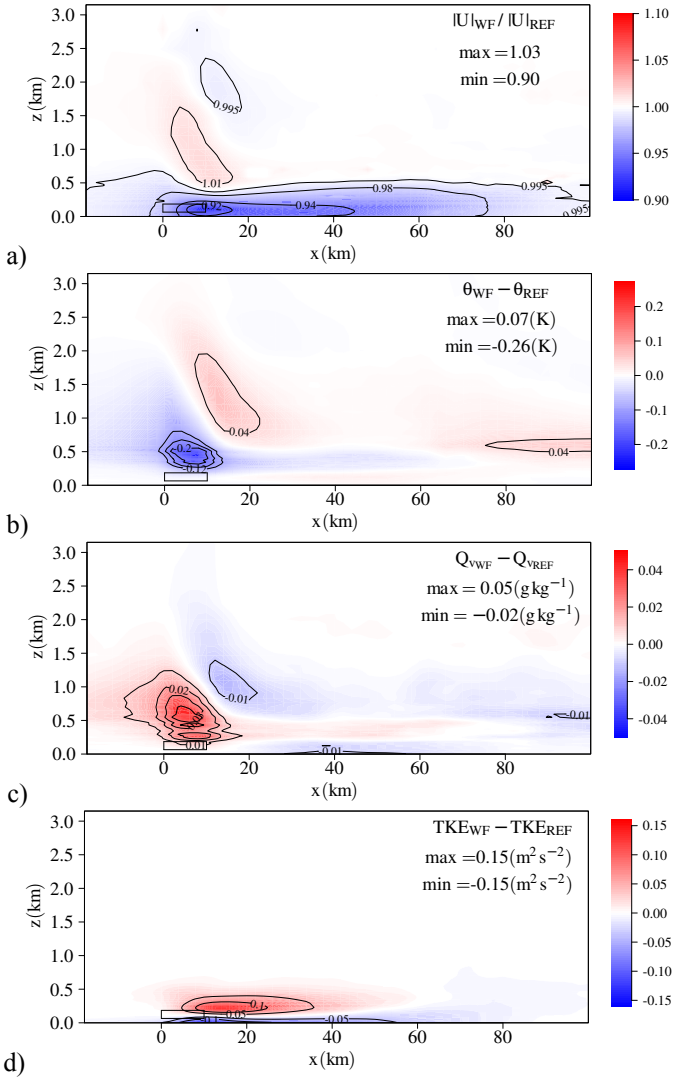

Figure 6.7: Wind farm cross-section of the a) normalised velocity, b) potential temperature difference, c) water vapour mixing ratio difference and d) TKE difference, between the reference and wind farm experiment. The rectangle indicates the horizontal and vertical (tip to tip) wind farm extension.

wind farm cross-section. In this figure we distinguish the influence of the wind farm to the MBL and to the lower troposphere. The 2% velocity reduction fills the whole

MBL and is advected up to the Gulf of the Farallones (Fig. 6.1). The temperature reduction and water vapour excess are transported to similar distances. The water vapour "wake" extends slightly further downstream. In the Gulf of the Farallones, circa 80 km downstream, a positive temperature and water vapour anomaly is seen. Fig. 6.5d shows that the enhanced TKE due to turbulence shear production remains within the boundary layer. The velocity surplus followed by a velocity reduction higher up are aligned to the wind farm. The same pattern is shown in Fig. 6.7b and Fig. 6.7c for the temperature and water vapour. Here negative temperature anomalies are related to positive water vapour anomalies and vice versa. The perturbations above the inversion layer cannot be explained by turbulence transport, since the enhanced turbulence mixing remains within the inversion layer (Fig. 6.7d, Fig. 6.5b). We hypothesise that the temperature and moisture anomalies are a consequence of wind farm induced standing waves. The ability of the WRF model to simulate mountain induced gravity waves has been demonstrated by e.g. Larsén et al. (2012). Furthermore, Smith (2009) used a linear wave model to analyse the influence of gravity waves to the wind farm efficiency. He found that when the vertical extension of the wind farm induced velocity deficit is in the order of the boundary layer depth, gravity waves are triggered due to a local shifting of the inversion layer.

Wind Farm Induced Standing Waves

We investigate if the atmospheric conditions within the wind farm area are favourable for gravity waves to be triggered by the wind farm and allow them to propagate. In Fig. 6.8a we show the boundary layer height perturbation, $\Delta H_{\mathrm{pbl}} = H_{\mathrm{pbl_{WF}}} - H_{\mathrm{pbl_{REF}}}$, for the wind farm cross-section, where $H_{\mathrm{pbl_{WF}}}$ and $H_{\mathrm{pbl_{REF}}}$ denote respectively the boundary layer height of the wind farm and reference simulation. In Fig. 6.8b the pressure perturbation $\Delta P = P_{\mathrm{WF}} - P_{\mathrm{REF}}$ is shown, where P_{WF} and P_{REF} are the turbine blade (tip to tip extension) averaged pressure in the wind farm and reference simulation. In Fig. 6.8c,d the Scorer parameter, L_s, times the characteristic length of the obstacle, b, Nappo (2002) and the Brunt-Väisälä frequency, N, are shown. The averaged boundary layer height perturbation follows approximately a bell-shaped distribution with a half-width of around 5 km. The positive pressure perturbation upstream of the wind farm, in Fig. 6.8b, shows that the wind farm acts as a porous medium to the flow. Consequently, the flow is partially directed around the wind farm leading to the boundary layer height perturbation. Consequently positive pressure gradients are found up and down-stream of the wind farm and negative gradients within the wind farm. For the considered wind farm, the pressure perturbation starts already more than 10 km upstream of the wind farm. This leads to an upstream deceleration of the flow, which is also seen in Fig. 6.7a. The magnitude of the pressure perturbations is in line with pressure perturbations, $\Delta P = 4$ Pa, obtained by Smith (2009). He used a linear wave model to simulate a large wind farm. The wind farm contained 4 times more turbines, however the results are comparable since the turbine blade area was 37 % smaller and the drag coefficient around 35% lower (for wind

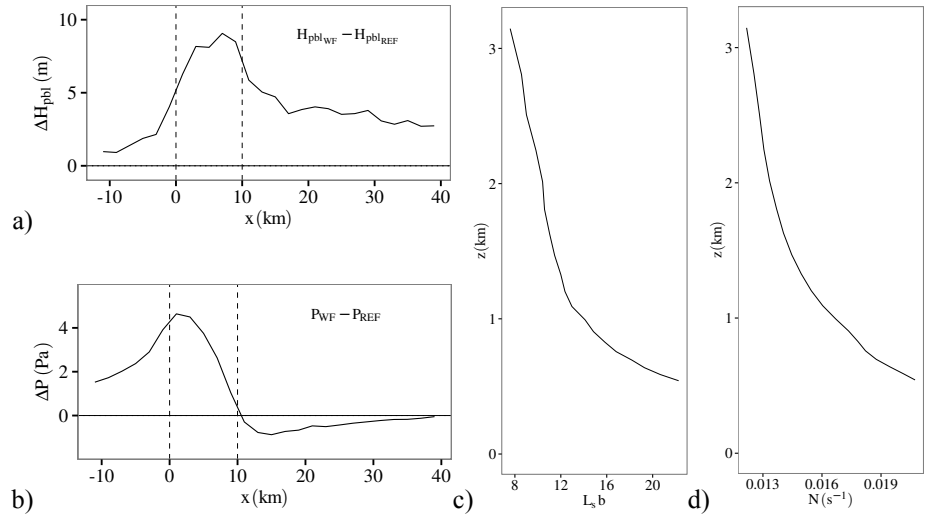

Figure 6.8: Annual average for wind directions between 270° and 274° of: a) the boundary layer height perturbation between the wind farm and reference simulation and b) the pressure perturbation averaged over the turbine blade tip to tip extension c) the wind farm averaged Scorer parameter, L_s times the characteristic length $b = 5000\,\text{m}$ and d) the wind farm averaged Brunt-Väisälä frequency, N. The dashed lines in figure a) and b) indicate the wind farm extension. Figure a) and b) are for the wind farm cross-section.

speeds of around $10\,\text{m}\,\text{s}^{-1}$). Furthermore, a lower turbine density was used. In Fig. 6.8c we plot the Scorer parameter,

$$L_s = \left(\frac{N^2}{U^2} - \frac{1}{U} \frac{\partial^2 U}{\partial z^2} \right)^{\frac{1}{2}},$$

times the characteristic length b of the wind farm as a function of the height, z. The Scorer parameter is obtained from the linear wave equation. In case we have $L_s/k > 1$, where $k = 2\pi/\ell$ is the wave-number with ℓ being the wavelength, wave propagation is supported by the flow. We follow Nappo (2002), where the product $L_s b$ is used. Fig. 6.8a shows that the characteristic length of the inversion layer perturbation is $b \approx 5000\,\text{m}$. For the product $L_s b$ it holds that if it is larger than one waves are supported for the considered obstacle characteristics, if it is around one the wave amplitudes decrease slightly in the downstream direction, while if it is smaller than one waves become directly evanescent. Fig. 6.8d shows the Brunt-Väisälä frequency,

$$N = \sqrt{\frac{g}{\theta} \frac{\partial \theta}{\partial z}},$$

as a function of the height. It follows from a decreasing scorer parameter in height, with $L_b\, b > 1$ and $N > 0.01\,\mathrm{s}^{-1}$ that the stratification of the atmosphere above 500 m supports waves. The decreasing product $L_b\, b$ suggests a decreasing wave amplitude in height.

Fig. 6.9 shows the contours of the staggered velocity component, V, for the wind farm cross-section, where V is the velocity component orthogonal to the longer edge of the wind farm. Additionally the vertical velocity difference between the wind farm and reference simulation is indicated by coloured contours. The patterns in vertical velocity

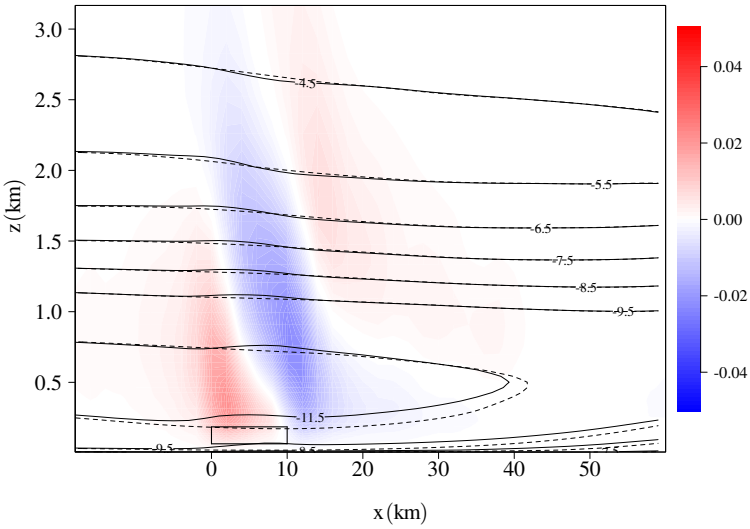

Figure 6.9: Cross-section of the velocity component, V, for the reference (dashed lines) and wind farm (solid lines) simulation. The coloured contours show the vertical velocity difference, between the wind farm and reference simulation.

anomaly follow those for the velocity, temperature and moisture in Fig. 6.5. The vertical velocity anomaly is associated with the increased and decreased velocity gradients, which are in turn related to changed gradients in the pressure field. In the next section we use a case study to consolidate our findings. We first analyse the single event for the implemented wind farm, then, we change the wind farm and turbine size to analyse the atmospheric sensitivity to the different forcing.

Wind Farm Induced Standing Waves - A Single Event

For the case study we choose 2009-07-25-10 UTC. In the model there are steady wind direction conditions for several hours, which range at hub-height between 272° and 276°. Under these conditions we expect the influence of the land to be small. Fig. 6.10 shows

the boundary layer height and pressure perturbation for the wind farm cross-section. The pressure perturbation is again averaged over the turbine blade tip to tip extension. The wind farm extension is marked by the vertical dotted line. Fig. 6.10a shows that the

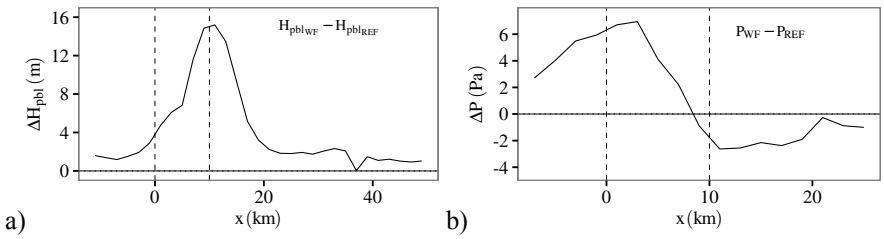

Figure 6.10: Wind farm cross-section plot from: a) the boundary layer height perturbation and b) the turbine blade tip to tip averaged pressure perturbation at 2009-07-25-10 UTC.

boundary layer height perturbation is approximately bell-shaped for this event. The perturbation grows within the wind farm and reaches its maximum at the end of it. The half width b of the distribution is almost 7.5 km. The pressure perturbation, as shown in Fig. 6.10b, increases again upstream of the wind farm and reaches a maximum of 6 Pa. The atmospheric background conditions within the wind farm area are shown in Fig. 6.11. It shows an always positive product of the Scorer parameter and b.

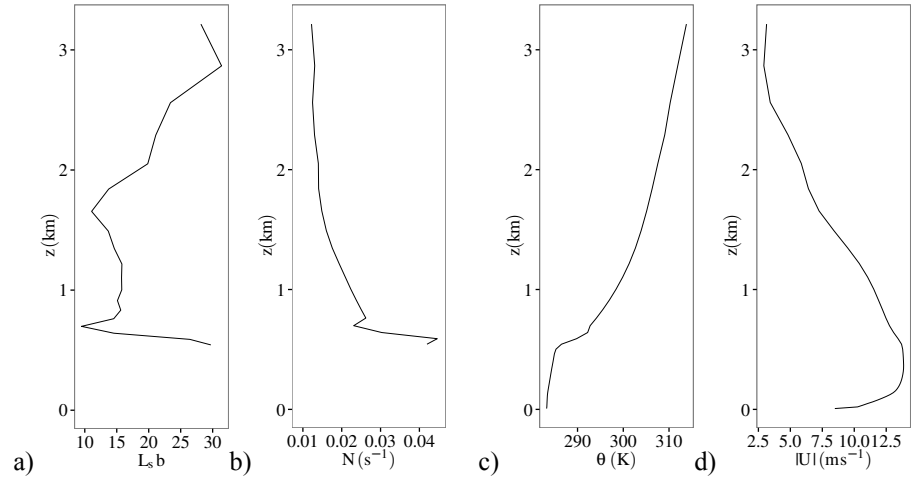

Figure 6.11: Wind farm averaged vertical profiles of the: a) Scorer parameter times b, b) Brunt-Väisälä, c) potential temperature and d) wind speed, at 2009-07-25-10 UTC.

Above 1.7 km the product increases due to the reduced horizontal velocity with height (Fig. 6.11d). Fig. 6.11b and Fig. 6.11c indicate a strong stability in the steep inversion layer. The lower troposphere has a constant stratification with $N = 0.01\,\mathrm{s}^{-1}$. Under

these conditions we expect wave motion to be supported in the lower troposphere. An additional useful parameter is the Froude number, $Fr = |U|/\sqrt{g'H}$ (Baines, 1995), where $g' = g\Delta\theta/\theta_0$ is the reduced gravity and H the thickness of the boundary layer. In a sub-critical flow, where the wave phase speed is higher than the wind speed, waves will travel upstream. Instead, in flows with super-critical Froude numbers the opposite happens. $\Delta\theta \approx 10\,\mathrm{K}$ and 500 m for the boundary layer height, gives a slightly sub-critical Froude number, $Fr = |U|/\sqrt{g'H} \approx 0.9$. This suggests upstream travelling waves, with related pressure gradients upstream of the wind farm (Fig. 6.10b).

Fig. 6.12a is similar to Fig. 6.9a, this time for 2009-07-25-10 UTC. In Fig. 6.12b we show instead of the velocity field the pressure contours. Figure 6.12c and Fig. 6.12d show the potential temperature and water vapour mixing ratio difference for the wind farm cross-section. Fig. 6.12a shows the blocking effect of the downstream land, which starts

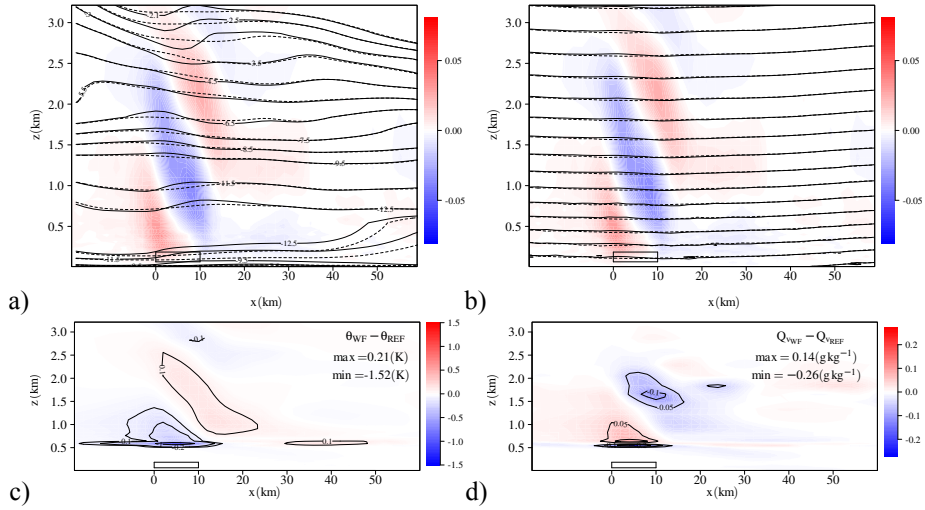

Figure 6.12: Wind farm cross-section for 2009-07-25-10 UTC of the a) velocity component V, b) pressure field, c) potential temperature difference and d) water vapour mixing ratio difference. In Fig. a) and b) the vertical velocity difference is shown in colour contours and the dashed and solid lines are from the reference and wind farm simulation, respectively.

around 40 km after the first row of the wind farm. The wave length of the inclined waves is around 20 km, which is approximately the size of the disturbance, ΔH_{pbl}. Furthermore, an increase in amplitude of the velocity component V is found at around 3 km, which is in line with the increased Scorer parameter at similar heights. The vertical velocity W anomaly follows the changed pressure field, where regions with a decreased pressure gradient show an enhanced vertical velocity and vice-versa (Fig. 6.12b). Fig. 6.12c and Fig. 6.12d show that the areas with temperature anomalies correspond to those with a

vertical velocity change. At around 500 m height, within the lower part inversion layer (Fig. 6.11c), a cooling up to 1.5 K occurs above the wind farm. In the places where the strongest cooling happens, the water vapour mixing ratio reduces due to cloud formation.

Flow Sensitivity to Wind Farm Dimensions

Finally, we examine the atmospheric response to a changed wind farm and turbine size for the same event, 2009-07-25-10 UTC. In this test we examine the atmospheric response to the changed forcing.

In the first sensitivity test, we reduce the total number of wind turbines to 80, while the number of turbines in the cross-wind direction is unchanged. Consequently, the number of turbines aligned to the flow is reduced to 4. Fig. 6.13 shows on the left panel the boundary layer height and pressure perturbation and on the right panel the contour lines for the velocity V-component, similarly to Fig. 6.12a. Fig. 6.13a and Fig. 6.13b show

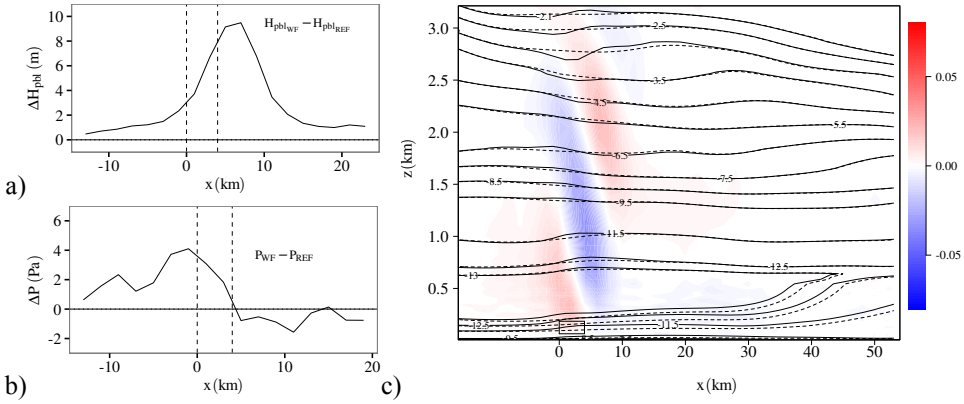

Figure 6.13: Left panel: Top, boundary layer perturbation. Bottom, turbine blade averaged pressure perturbation. The dashed lines mark the horizontal wind farm extension. Right panel: velocity contour plot, similar to Fig. 6.12a.

that the width and intensity of the boundary layer height perturbation distribution and the intensity of the pressure perturbations are reduced compared to those of the reference wind farm. The reduced intensity is expected from the reduced flow distortion for the smaller wind farm. Under equal atmospheric conditions the boundary layer height perturbation for a small wind farm will not grow to the same value, then that of a larger wind farm. The half width of the boundary layer height perturbation is around 4 km, compared to almost 7.5 km in the reference wind farm simulation. This leads to a $L_s\,b$ of around 8, which is still larger than one. Fig. 6.13 shows that the amplitude of the V

velocity perturbation is reduced compared to that of the reference wind farm simulation. This is a consequence of the decreased amplitude of the boundary layer perturbation. Furthermore, an increased frequency is found, which is a consequence of the reduced distribution width.

In the second sensitivity test we change the turbine characteristics and leave the total number of wind turbines and the wind farm extension unchanged. We increased the turbine hub-height to 160 m and its diameter to 150 m. The rated turbine power is in this way increased to approximately 10 MW. The individual turbine spacing is consequently reduced to around $6.7\,D_0$, compared to $8\,D_0$ for the reference wind farm. The

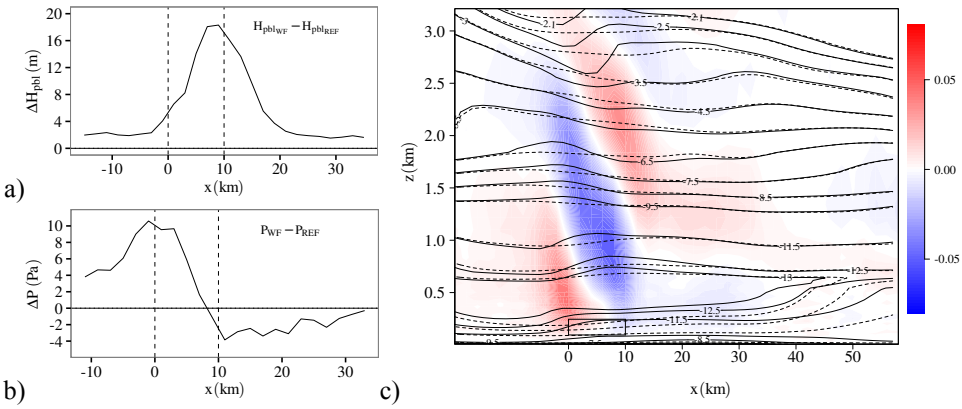

Figure 6.14: The plots are similar to those in Fig. 6.13. This time larger wind turbines have been used.

plots in Fig. 6.14 are similar to those in Fig. 6.13, this time for a wind farm with the larger turbines. Figure 6.14a shows that the width of the bell-shaped boundary layer height perturbation distribution is similar to that of the original wind farm (Fig. 6.10a). However, the perturbation increased due to the taller wind turbines. These results are expected, since the wind farm size is set to be equal to the reference wind farm. However, the total production is higher and hence the blocking effect of the wind farm increases. In Fig. 6.14c we see that the standing waves response is in line with the changed forcing. The amplitude of the waves increased, whereas the frequency is similar to that of the reference wind farm (Fig. 6.12a).

6.1.5 Conclusion

Offshore wind energy offers the advantage of generally higher and more steady wind conditions compared to that onshore. Hence, power generation from wind becomes more

efficient. The Californian coast is known for its persistent high wind speeds and the vast majority of its population is situated near to the coast, therefore it would provide perfect conditions for offshore wind power generation. However, its coastal ecosystem is complex.

We investigate with the Weather Research and Forecast (WRF) mesoscale model the interaction between a large hypothetical offshore wind farm, which was located around 80 km to the North-East of San Francisco and the lower marine atmosphere. The hypothetical wind farm contained 200 wind turbines with a rated power of 5 MW, giving it a nominal capacity of 1 GW. This capacity would be sufficient to provide energy to around 500.000 households in the San Francisco Bay area. For this study, a complete calendar year has been simulated, to account for the seasonal variation. From the reference simulation, without wind farm, we found that the near surface wind climatology was accurately simulated well by the WRF model. Generally a good agreement was found with buoy measurements, apart from one buoy in the Monterey bay. Here the model was not able to properly simulate the local land-sea interaction. Furthermore, we found low biases between the model and satellite data from QuikSCAT and a generally fine agreement with the spatial structure of the wind field. Similar to Dvorak et al. (2010), high wind speeds are found at the wind farm location, which is to the North of Point Reyes. The average wind speed for 2009 was at 125 m was almost 10 $\mathrm{m\,s^{-1}}$. For the wind farm simulation the EWP parametrisation has been used.

From the results of the wind farm simulation we found a high wind farm efficiency for along-shore wind speeds. The annual averaged velocity reduction within the wind farm was only around 6% and upstream to the wind farm it was 4%. The intensity of the upstream reduction is for an important part determined by the atmospheric conditions aloft. In case of the upstream travelling of gravity waves, increased upstream pressure perturbations are expected. The influence of the wind farm to the lower atmosphere can be divided into two parts. First, the reduced wind speeds provides the mechanisms for increased mixing in the boundary layer and second the blocking effect of the wind farm perturbs the stable stratified atmosphere aloft.

Within the boundary layer for along-shore winds there is an annual averaged velocity deficit extension of around 80 km downstream, which hence would reach the Gulf of the Farallones. The negative temperature and positive moisture anomalies extend within the boundary layer to similar downstream distances. Associated to the lower temperatures and higher water vapour content, boundary layer cloud formation in the inversion layer at locations where the largest temperature perturbations occur. In the lower troposphere aloft, gravity waves are generated, with related temperature and water vapour anomalies up to 3 km heights. We used the model boundary layer height to define the wind farm induced perturbation. For the performed simulations the boundary layer height, as

estimated with the MYNN boundary layer scheme, has given realistic results over the marine boundary layer. The boundary layer height perturbation was found to match the perturbations of the physical variables. Perturbations of stable flows over rigid lids are determined by the lid's structure, whereas those of wind farms are not only a function of the turbine and wind farm size, but vary also in time as a function of the velocity reduction.

We examined also the sensitivity of the atmospheric conditions to a smaller wind farm and to a wind farm with the same extension, but larger turbines. We found that for the smaller wind farm, both the amplitude and wave-length decreased. The decreased amplitude is related to the reduced wind farm size, since the perturbation grows in the downstream direction. The reduced wave-length is expected from the smaller wind farm extension. From the simulation with larger wind turbines, we found increased wave amplitudes and a similar wave-length to that of the reference wind farm. The increased amplitude, would increase the probability of breaking waves with related clear air turbulence.

We thus conclude that the wind farm efficiency was high for the atmospheric conditions as present in northern California. Atmospheric impacts were found in the boundary layer, where the increased mixing can cause additionally cloud formation. On the other hand, the shallow boundary layer does, with the steep inversion, provide good conditions for gravity waves to be generated. However, since the mesoscale model fields are smoother compared to those observed, it is expected that for real wind farms, the amplitude and frequency of the gravity waves differ.

An obvious extension to this work is to use the model results for studying the sensitivity of the wind farm induced cloud formation. Additionally, the influence of the wind farm to the planetary boundary layer and surface layer over land is to be investigated. Furthermore, since one of the most important characteristics of this region's eco-system is the upwelling of nutrient rich deep water, it would be of interest to study the ocean feedback to the reduced wind-farm induced near surface winds.

6.2 Velocity Restoring Mechanisms

In Sect. 6.1, we found that the upstream positive pressure gradients, which are related to flow decelerations, extended up to around one wind farm length. For the planning of wind farm layouts it can be therefore of relevance to understand in a quantitative way the restoring mechanisms: upstream, within and in the wake of the wind farm. Smith (2009) studied with a linear two layer wave model the velocity field in these three regions for different atmospheric conditions. The hypothetical wind farm contained 800 3 MW turbines (D_0 = 100 m) and it was placed in the lower mixed layer. This layer was capped by

a temperature inversion with different strengths determined by a step in potential temperature, $\Delta\theta$. The stable upper model-layer had a Brunt-Väisälä frequency $N = 0.01\,\mathrm{s}^{-1}$ in all simulations. The results of this study will be used as a reference in our experiments.

We use the mesoscale model to analyse the relative importance of the involved wake recovery processes for different atmospheric conditions. The main advantage of a mesoscale model, compared to a linear two layer wave model, is the vertical resolved flow structure. This allows for simulating the interaction between the mixed layer and the stable atmosphere more completely. However, the flow characteristics in mesoscale models are smoother compared to the actual conditions, since only averaged fields in the order of a few kilometres are resolved. In this way the wind farm acts as an homogeneous drag device. In reality, instead, only the single turbines act as drag devices and the flow in the perpendicular direction is at least in the first rows not homogeneous. Therefore, we assume that the flow disagreement between the mesoscale model and the observations is limited to the first turbine rows, where the single turbine wakes did not merge yet. Due to the blocking effects of wind farms, the flow is partially directed around the wind farm. Within the mixed boundary layer, this also leads to a lifting of the flow. The lifting of cold air from below causes then a local cold anomaly within the inversion layer, which is related to a pressure increase within the mixed layer. The altered pressure field will cause horizontal pressure gradients that act to accelerate or decelerate the flow. In this regard the introduction of the Froude number is of benefit. In Smith (2009) it is defined as the ratio between the flow velocity, U, and the phase velocity of the wave,

$$Fr = \frac{U}{\sqrt{g\frac{\Delta\theta}{\theta}H_{pbl}}}.$$

Here θ denotes the reference temperature of the mixed boundary layer and H_{pbl} the boundary layer height. For sub-critical flows, when $Fr < 1$, the phase velocity is larger than the wind speed and the waves travel upstream, whereas in a super-critical flow, when $Fr > 1$, the low phase velocity does not allow waves to propagate upstream. In Smith (2009) a clear sensitivity to the Froud number could be found. With decreasing Froude numbers a more pronounced wind reduction ahead of the wind farm was noticed and an associated large positive pressure gradients found within the wind farm.

6.2.1 Experimental Set-up

For this study we consider a wind farm of 200 turbines. The turbines are similar to the Enercon E-126 turbines, with a 126 m blade diameter and a 5 MW rated capacity. The hub-height is in this section defined at 130 m above the surface. The wind farm extends 10 turbines in the flow direction and each column contains 20 turbines. The turbine spacing is in both directions 8 turbine diameters. We examine the sensitivity of the velocity

field to four different atmospheric conditions. The selected flow conditions are a function of inversion strength and the velocity field above the inversion, see Table 6.2. The

Table 6.2: Experimental set-up of the Atmosphere

	Super-Critical		Sub-Critical	
	C1	C2	C3	C4
$\Delta\theta$ (K)	2	2	4.5	4.5
Fr	1.3	1.3	0.91	0.91
Geostrophic wind	Barotropic	Baroclinic	Barotropic	Baroclinic
$\Delta U/\Delta z\ \left(s^{-1}\right)$	-	-10^{-3}	-	-10^{-3}

cases with a weak inversion strength (C1, C2) are typical for mid-latitude offshore conditions, where the contrast between the sea temperature and the lower atmosphere is not large. Whereas the strong inversions are characteristic for a warm atmosphere above cold (deep) water as for example present near to the coast of California or North-West Africa. Furthermore, we initialise the model with a barotropic (C1, C3) and a baroclinic atmosphere (C2, C4). For the latter case we have chosen a decreasing geostrophic wind speed in height, which is observed along western coastal areas in the Northern-Hemisphere caused by a warm land and cold sea temperature contrast. Similar to Smith (2009), the lower troposphere has a constant Brunt-Väisälä frequency $N = 0.01\,\mathrm{s}^{-1}$. The model simulations are performed in the idealised case mode (Chapter 4). Two wind farm parametrisations are used, the WRF-WF scheme and EWP, which are described in Sect. 4.2.3 and Sect. 4.3, respectively. The model configuration is shown in Table 6.3.

Table 6.3: WRF Configuration

Wind farm parametrisation	EWP / WRF-WF:
Wind speed $\left(\mathrm{m\,s}^{-1}\right)$:	9.1
Wind direction $(^\circ)$:	270
Number of Grid points (nx, ny, nz):	120, 60, 80
Domain extension in x and y (km, km):	240, 120
Horizontal grid spacing (km):	2
H_{pbl} (m):	650
Wind farm extension (nx $\times$ ny):	5×10
Boundary condition:	OPEN
PBL scheme:	MYNN (1.5)

6.2.2 Velocity Recovery at Hub-Height

In Fig. 6.15 we show the normalised hub-height velocity for the EWP and WRF-WF scheme. Both schemes are sensitive to the inversion strength, which is expressed by the

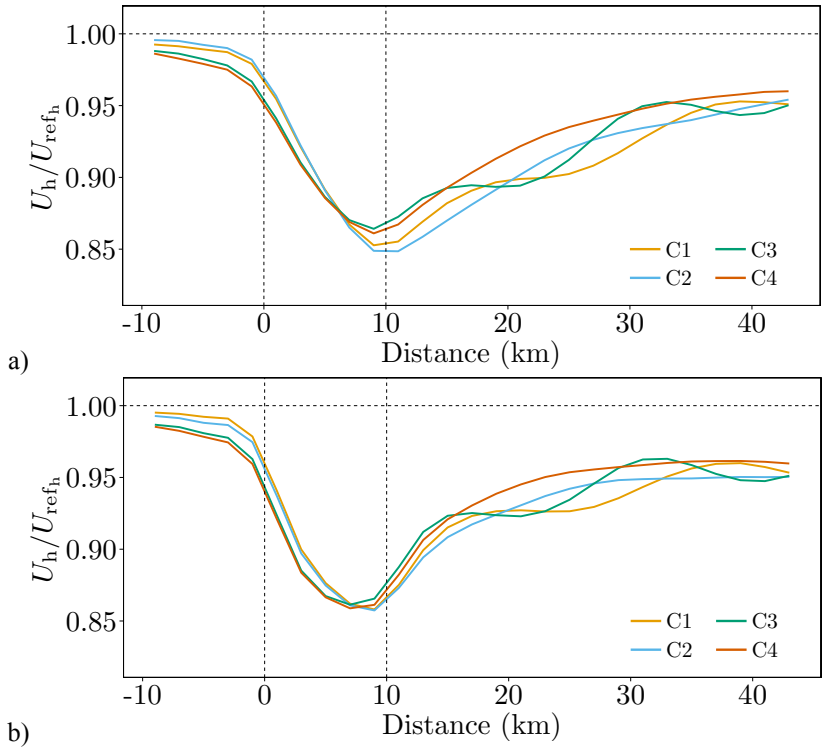

Figure 6.15: Normalised velocity at hub-height for the several experiments in Table 6.2 a) EWP and b) WRF-WF scheme. The four cases are indicated with the different colours. The wind farm extension is marked by the vertical dotted lines. The wind farm is defined from the left lateral boundary of the first turbine containing grid-cell up to the right lateral boundary of the final turbine containing grid-cell.

positive upstream pressure gradients. The velocity at the first turbine containing grid-cell is already up to around 5% reduced. At the end of the wind farm, differences in the hub-height velocity between the EWP and WRF-WF scheme occur. In the WRF-WF scheme the velocity deficits for all cases seem to converge, whereas in the EWP scheme they remain distinguishable for the different inversion strengths. In the wind farm wake, we notice from the velocity field that for barotropic atmospheres (C1 and C3) gravity waves travel horizontally downstream. For both schemes the wave length is of the order of the wind farm size, however the phase is shifted by around a quarter period.

With the baroclinic atmosphere the waves propagate upwards (not shown), similar to the waves simulated in Sect, 6.1. We notice, finally, that the recovery process is slower with the EWP scheme. In Table 6.4 the velocity response to the different atmospheric conditions is summarised. The general features conform with the results of Smith (2009).

Table 6.4: Summary of the velocity dependence on atmospheric conditions.

Atmosphere	Before Wind Farm	Wind Farm	After Wind Farm
Baroclinic wind	-	-	Not oscillating
Barotropic wind	-	-	Oscillating
Weak inversion	Small reduction	Large reduction	Faster recovery
Strong inversion	Large reduction	Small reduction	Slower recovery

Specifically, both models show the same sensitivity in the wind farm induced velocity field to changed inversion characteristics. For the super-critical flow (C1 and C2) the waves do not propagate upstream and hence the positive pressure gradients in front of the wind farm are smaller compared to the sub-critical cases. Within the wind farm, the negative pressure gradients acts to accelerate the flow in opposition to the turbine induced drag force. In the sub-critical flow the negative pressure gradients are larger.

6.2.3 Analysis of the Forcing Terms

In this section the forcing mechanisms that determine way the velocity field recovers are analysed. We will consider the individual forcing components that act on the Lagrangian the stream-wise U component of the velocity field. The Lagrangian RANS equation for U reads

$$\frac{DU}{Dt} = \frac{\partial U}{\partial t} + U_i \frac{\partial U}{\partial x_i} = -\frac{\partial \overline{u_1 u_3}}{\partial x_3} - \frac{1}{\rho}\frac{\partial P}{\partial x_1} - F_{D_1}. \tag{6.7}$$

Here the material derivative is denoted by D/Dt. The first and second term on the right hand side accelerate or decelerate the flow, through turbulent momentum fluxes and negative or positive pressure gradients. The turbine-induced drag, which causes the flow to decelerate, is described by the third term on the right hand side.

Fig. 6.16 shows the turbulent momentum flux $\overline{u_1 u_3}$ for the EWP and WRF-WF scheme. This flux is in the mesoscale model parametrised with Eq. (5.2). Its divergence or convergence causes a flow deceleration or acceleration due to turbulence momentum flux, respectively. The intensity of the vertical turbulent momentum flux is proportional to the turbine induced turbulence (Fig. 6.16a). The large turbulent momentum fluxes within the wind farm in the WRF-WF scheme, are mainly caused by the additional TKE production term $\overline{u_i f_{D_i}}$ (Fig. 6.16b). These large fluxes (up to around three times larger than in the EWP scheme) allow the velocity field to recover quickly. The WRF-WF scheme shows

a local minimum flux at the lower turbine blade tip. This is due to the low vertical shear of horizontal wind speed.

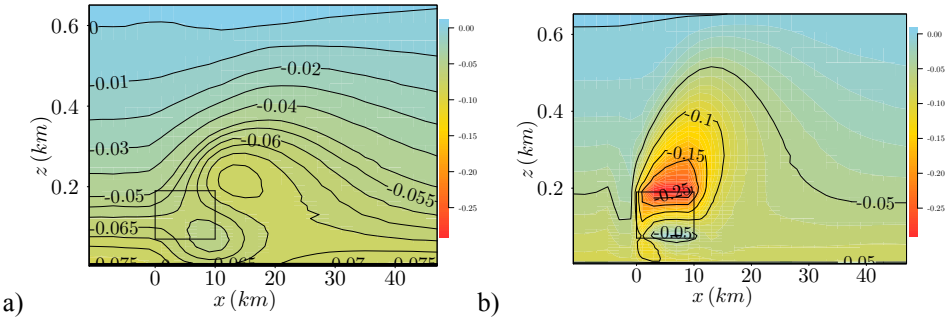

Figure 6.16: Cross-section of the vertical turbulent transport of horizontal turbulent momentum $\left(\mathrm{m^2\,s^{-2}}\right)$ for: a) EWP scheme and b) WRF-WF scheme. Note that different contour lines are used.

In Fig. 6.17, Fig. 6.18, Fig. 6.19 and Fig. 6.20 we plot for all atmospheric cases (Table 6.2) the single components from the right hand side of Eq. (6.7). The cross-section is from East to West and it passes through the centre of the wind farm. We use only different colour scales for the vertical component of the turbulent momentum flux divergence for both schemes. For the horizontal pressure gradient in the x direction, a five point stencil is considered. In Fig. 6.17 we show the single velocity restoring components for the barotropic case with a small temperature gradient at the inversion. Figure 6.17c and Fig. 6.17f show the distribution of the wind farm induced drag force. The maximum turbine-induced drag, F_D, is $-1.6 \cdot 10^{-3}\,\mathrm{m\,s^{-2}}$ and $-3.2 \cdot 10^{-3}\,\mathrm{m\,s^{-2}}$ for the EWP and WRF-WF, respectively. The drag force is in the WRF-WF limited to the vertical turbine blade extension, whereas the drag force in the EWP parametrisation is less intensive and extends beyond the turbine blades. Fig. 6.17a shows that the accelerations due to turbulent momentum flux convergence are up to $-0.2 \cdot 10^{-3}\,\mathrm{m\,s^{-2}}$for the EWP scheme. They occur at the end and in the near wake of the wind farm. Decelerations due to turbulent momentum flux divergence are found above the wind farm with a maximum of $0.3 \cdot 10^{-3}\,\mathrm{m\,s^{-2}}$. Figure 6.17d shows that for the WRF-WF scheme the accelerations are strictly within the turbine blade area and decelerations occur above and below turbine blade area. The accelerations reach $-2.2 \cdot 10^{-3}\,\mathrm{m\,s^{-2}}$ and the decelerations $1.2 \cdot 10^{-3}\,\mathrm{m\,s^{-2}}$. This means more than one order of magnitude higher accelerations in the WRF-WF scheme compared to the EWP scheme, due to turbulent flux convergence. The WRF-WF scheme shows also turbulence related accelerations upstream to the wind farm and decelerations below the lower turbine blade tip. Fig. 6.17b shows the altered pressure field related to the horizontally travelling waves. The intensity of the pressure

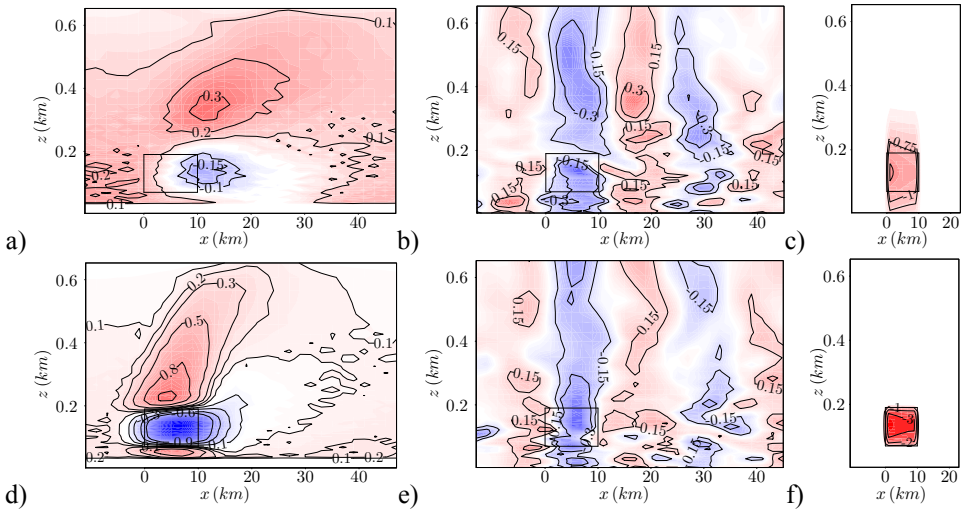

Figure 6.17: Individual terms of Eq. (6.7) $\left(\mathrm{m\,s^{-2}}\right)$ for the case C1. The plots a), b) and c) are for the EWP scheme and d), e) and f) for the WRF-WF scheme. Plot a), d) show the vertical divergence component of turbulent momentum flux, b), e) the horizontal pressure gradient and c), f) the turbine-induced force. The turbine blade extension is indicated by the rectangle.

gradient fluctuation is up to $\pm 0.6 \cdot 10^{-3}\,\mathrm{m\,s^{-2}}$ for both schemes.

In Fig. 6.18 we show the single velocity restoring components for the baroclinic case with a small temperature gradient at the inversion. Fig. 6.18c and Fig. 6.18f show, that the drag forces are very similar to those in the previous case. Also the influence of the turbulent fluxes remain fairly unchanged. In the EWP scheme those accelerations occur again at the end of the wind farm, between the regions with the locally lowest and largest momentum flux (Fig. 6.16), whereas, in the WRF-WF accelerations due to turbulent fluxes are found from ahead of the wind farm up to a few grid-cells after the wind farm. Here the locally lowest and largest momentum flux are at the lower and upper turbine blade tip, respectively. Compared to the previous barotropic case, the horizontal pressure gradients are limited to the wind farm area, since the gravity waves propagate upwards rather than downstream. The intensity of the pressure gradients is similar to the previous case.

Fig. 6.19 shows the velocity restoring components for the barotropic case, with the stronger inversion strength. Again the maximum drag force and the accelerations caused by the turbulent fluxes are almost identical to the previous cases. However, due to the strong inversion strength more pronounced horizontal pressure gradients in the down-

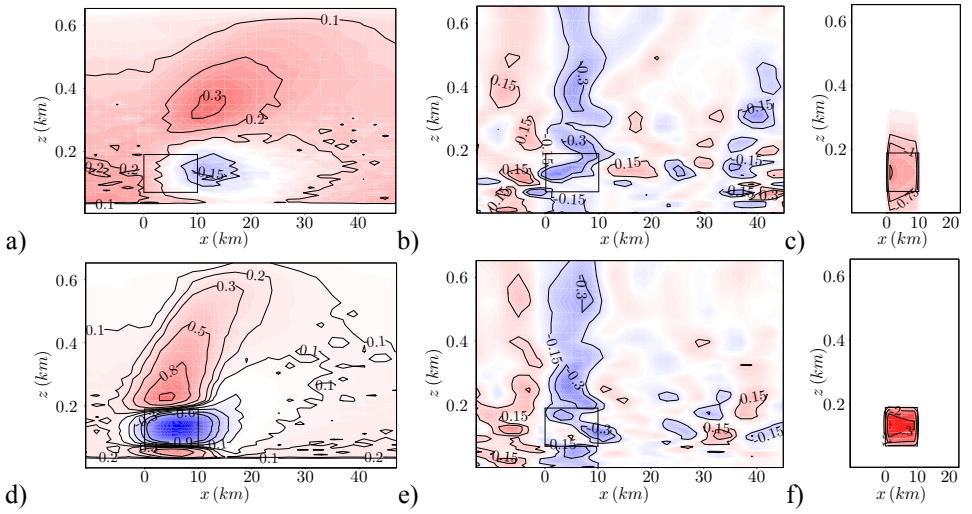

Figure 6.18: As in Fig. 6.17, but for the C2 case.

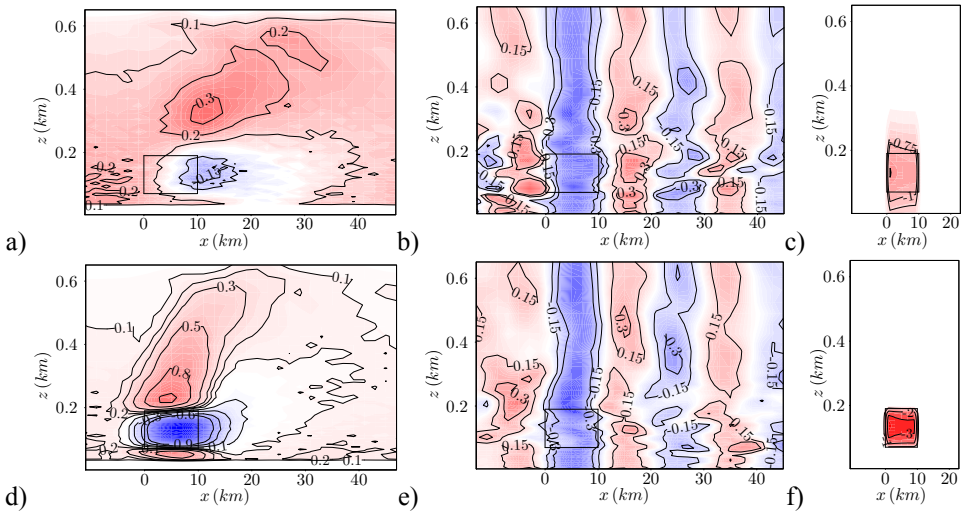

Figure 6.19: As in Fig. 6.17, but for the C3 case.

stream direction occur. Their intensity weakens somewhat in the downstream direction. Compared to Fig. 6.17b and Fig. 6.17e, we find also a more pronounced altered pressure gradients upstream of the wind farm. This is due to the larger wave phase velocity in

comparison to the wind velocity, which allows the waves to travel upstream. The pressure gradients are around 20% larger than in the previous cases. The pressure gradients are larger for the EWP approach.

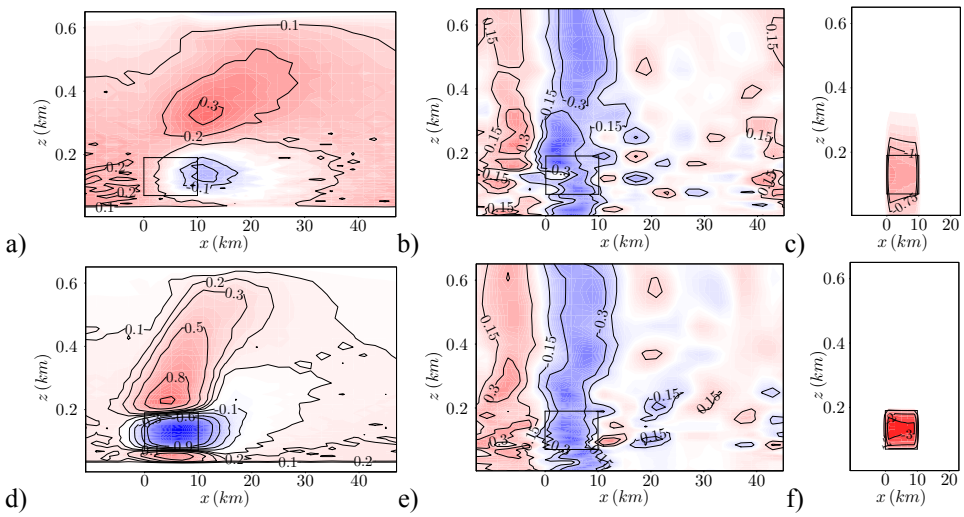

Figure 6.20: As in Fig. 6.17, but for the C4 case.

Fig. 6.20 shows the velocity restoring components for the baroclinic case, with the stronger capping inversion. For this case the positive horizontal pressure gradients upstream to the wind farm are more pronounced, compared to the first baroclinic case (Fig. 6.18). After the wind farm no pressure gradient are found, again due to the upwards travelling waves.

6.2.4 Wind Farm Production for Different Atmospheric Conditions

To which extend different atmospheric conditions can influence the wind farm power production, is an important question. With a mesoscale model the local turbine production can not be accurately determined from the standard model fields. However, the production can be estimated, assuming the local turbine wind speed to be on averaged comparable to the grid-cell wind speed. The power production per turbine is given by

$$P = \frac{1}{2}\rho_0 \pi C_P R_0^2 U_0^3, \tag{6.8}$$

where ρ_0 is the atmospheric density. In Table 6.5 the total wind farm productions for the different atmospheric conditions are listed.

Table 6.5: Estimated wind farm production for the four atmospheric cases.

Approach	C1	C2	C3	C4
EWP (MW)	371	362	368	358
WRF-WF (MW)	369	360	364	355

Table 6.5 shows that the power production is similar for both schemes and cases, which could be expected from their velocity fields. The production differs for the various atmospheric conditions up to 4%. The velocity field for the different inversion strengths develop analogously within the wind farm. They diverge however in the final wind farm grid-cells. Table 6.5 shows that a higher production is simulated for baroclinic conditions, in which the negative pressure gradient in the wind farm is larger than in the barotropic case. This suggests that for the examined flow conditions, the effect of the positive pressure gradients due to upstream travelling waves, influences the power production less, than those ones of the wind field characteristics in the free atmosphere.

6.2.5 Discussion

From these experiments, we find that the turbulence momentum fluxes are not affected strongly by a changed atmosphere aloft. Instead, the horizontal pressure gradient is shown to be sensitive to the atmospheric conditions aloft. For the EWP scheme the magnitude of the pressure gradients is around twice as large than the divergence of the turbulent momentum flux, consequently a higher sensitivity to changed pressure gradients is found in the velocity field (Fig. 6.15a). In the WRF-WF scheme, on the other hand, the turbulent fluxes dominate over the pressure gradients and hence the hub-height velocity field in Fig. 6.15b shows weaker dependencies to changed atmospheric conditions. The results of this study show, that the wind conditions above the inversion layer are not relevant for the velocity recovery, since the atmosphere above the boundary layer remains detached. We find that the power production is influenced by atmospheric conditions, with a higher sensitivity to the geostrophic wind than to the inversion strength.

For the mid-latitudes where baroclinic conditions with an increasing wind speed in height are common, it is interesting to investigate what an optimal wind farm spacing would be, since waves are expected to travel downstream. From the normalised velocity field we found that the most convenient position of a downstream wind farm is a function of the atmospheric conditions aloft. Especially in cases with downstream propagating waves the velocity field can be expected to vary significantly downstream. From these simulations the baroclinic atmosphere seems to be the most convenient environment for a downstream turbine.

7

Application of Mesoscale Wake Parametrisations

In this Chapter some applications for wind farm simulations are introduced. In Sect. 7.1, the mesoscale model is used to estimate potential power production limits. For the planning of future offshore wind farm it is crucial to understand if an actual power production limit exists in dependency of the wind farm size or turbine spacing for the choosen location. In Fig. 2.1 of Chapter 2 examples of large offhore wind farms are given. In Sect. 7.2 we discuss the option of coupling meso and micro-scale models. The advantage of such an oproach is that the high resolution of the misco-scale model allows to account for the local effects unresolved by the mesoscale model. Thereafter, in Sect. 7.3, wind farm interactions are studied for idealised case simulations. Here we analyse the sensitivity of downstream wind farm efficiency to wind farm spacing. In Sect. 7.4, we shortly discuss the wind farm induced velocity field at the lowest model layer. This is of interest, when studying the ocean feedbacks from a wind turbine induced forcing.

7.1 Power Production of Large Wind Farms

Wind turbines and wind farms continue to increase in size to become more economically viable. Therefore, one major question that arises for the energy industry in general and for policy makers, is whether the total amount of available wind energy that can be extracted by wind farms is limited. Equivalently one could pose the question if the energy production per area is generally limited.

It can be expected that the long-term energy production per unit area is a function of I) turbine density, II) wind turbine characteristics, III) wind farm extension, IV) wind climate and V) atmospheric conditions aloft. Regarding the final point the wind farm power production varies by up to 4% for different atmospheric conditions aloft (Chapter 6). Before we examine the sensitivity of power production to point III and IV, namely the wind farm extension and the wind climate, we summarise the findings of previous studies.

7.1.1 Previous Investigations

In the past decade several authors have estimated the total global available wind power or the power production per area (Archer and Jacobson, 2005; Lu et al., 2008; Jacobson and Archer, 2012; Adams and Keith, 2013). In the literature the power availability is often expressed by the power production, PD, which is the product of the capacity factor, CF, and the rated capacity density CD. The power density and the capacity density can be expressed in $\mathrm{W\,m^{-2}}$.

Archer and Jacobson (2005) estimated the global wind power potential at 80 m height, from a five year data-set. The data-set contained a dense network of 10 m surface wind speeds and sounding observations. For the extrapolation of the 10 m wind speeds to 80 m, the best fitting parameters of the five nearest soundings were used. The final 80 m wind speeds were categorised in 7 wind classes. For the total available power all stations with a wind speed higher than 6.9 $\mathrm{m\,s^{-1}}$ (class ≥ 3) were included. The land area with wind speed larger than 6.9 $\mathrm{m\,s^{-1}}$ was 12.7% of the land surface. All over this area 1.5 MW turbines with a rated power density of $CD = 9\ \mathrm{W\,m^{-2}}$ were placed. The spatial capacity factor was estimated with the empirical relation from Jacobson and Masters (2001). Considering the capacity factor, the wind production density was 4.3 $\mathrm{W\,m^{-2}}$ over the 12.7% of the land surface. Lu et al. (2008) used the unprocessed wind speeds from Goddard Earth Observing System Data Assimilation System (GEOS-5 DAS), with a spatial resolution of 66.7 $\times$ 50.0 km, to estimate the global available power. Their capacity factor was obtained by normalising the actual estimated power production density from GEOS-5 DAS data with the rated power density. The rated power density was 8.9 $\mathrm{W\,m^{-2}}$ and 5.8 $\mathrm{W\,m^{-2}}$ for onshore and offshore conditions, respectively. From this study the power density increased up to 7.2 $\mathrm{W\,m^{-2}}$. However, the data did not account for important local wind speed characteristics, such as the speed-up effects over mountains or the channelling effects of the topography. Furthermore, the effect of turbine interaction to the power production was not considered. Jacobson and Archer (2012) studied with a global coupled atmosphere-ocean model, the saturation wind power potential over the entire globe and over the land only. The turbines were treated as a momentum sink similar to Roy et al. (2004). They concluded the total amount of available energy at 100 m height to be 80 TW over land and coastal areas.

In a recent study, Adams and Keith (2013) estimated the limits of power production for very large wind farms with the mesoscale model WRF. The effects of the turbine-induced velocity and power reduction have been accounted for with a wind farm parametrisation. The authors estimated the limits of the power production, by comparing the expected power density with the actual power density. The expected power density was obtained from a control run without the effect of wind turbines, whereas the actual power density was obtained from a simulation with the wind turbines. The wind farm scheme is described in Adams and Keith (2007). It considers a sink for momentum

and a source in turbulence kinetic energy. The power production was assumed to be a function of the wind farm size and turbine density. The wind farm sizes varied from small $\left(2.7 \cdot 10^3\,\mathrm{km}^2\right)$ up to large $\left(2.5 \cdot 10^5\,\mathrm{km}^2\right)$ and the capacity density ranged from 0.5 $\mathrm{W\,m^{-2}}$ to 32 $\mathrm{W\,m^{-2}}$. The sensitivity study was limited to the Great Plains for a duration of 10 days, from 2009-01-05 onwards. For this period the mean wind speed over the whole region was less than 10 $\mathrm{m\,s^{-1}}$ (no wind speed distribution is provided). Additionally, to gain robustness, the authors have run an additional experiment over the same domain for the complete month of June with the very large wind farms only. In their simulations the actual power production converged to around 1 $\mathrm{W\,m^{-2}}$ for the considered wind farms ($2.7 \cdot 10^3\,\mathrm{km}^2$, $3.0 \cdot 10^4\,\mathrm{km}^2$, $1.1 \cdot 10^5\,\mathrm{km}^2$, $1.3 \cdot 10^5\,\mathrm{km}^2$, $2.5 \cdot 10^5\,\mathrm{km}^2$, $2.7 \cdot 10^5\,\mathrm{km}^2$ and $5.0 \cdot 10^5\,\mathrm{km}^2$). The authors suggested that the maximum energy that can be extracted by turbine arrays at large scales is about 1 $\mathrm{W\,m^{-2}}$ and was found to be independent of the wind farm size.

Analogous to (Adams and Keith, 2013), we use a limited area model to estimate the limits of power production as a function of the wind farm size. Furthermore, we extend the investigation in considering also different wind climates.

7.1.2 Experimental Set-Up

In this study we use for convenience the same nomenclature regarding the power production as that used in Adams and Keith (2013). The total wind farm power production without the wind turbine induced wake effects is referred to as “expected power” and with the inclusion of the turbine shadowing effects is referred to as “actual power”. The term expected power is, perhaps, somewhat misleading, since shadowing effects from turbines are expected.

The power production sensitivity is examined for 3 wind farm parametrisations, 3 wind climates and 6 wind farm sizes. The 3 wind farm parametrisation are the ROTOR-DRAG, WRF-WF and EWP approach (see Chapter 4 for further information). The three different climates are realised from nine simulations with different upstream wind speeds. Every simulation is run with and without wind farms. The simulations without wind farms are used to determine the expected power production, whereas the simulations with the wind farm are used for the actual power production estimation. We minimise the computational costs by running simulations for the largest wind farm size only. The smaller wind farms were computed by considering a fraction of the largest wind farm, starting from the first upstream grid-cell.

7.1.3 Model Set-Up

Similar to previous performed simulations, the mesoscale model is configured in the idealised case mode (see Chapter 4 for additional information). The simulations are performed for 9 different wind speeds, which range from 4.8 $\mathrm{m\,s^{-1}}$ to 18.5 $\mathrm{m\,s^{-1}}$ at hub-height. The hub-height wind direction is 270°. For this wind speed interval we maintain the upstream wind speed between the cut-in and cut-out wind speed. Later on the different wind speeds are used to compose different wind climates. The largest wind farm contains 1200 turbines with a nominal capacity of 2 MW (V80), hereafter referred to as WF6. The smaller wind farms include from 200 to 1000 2 MW (V80) wind turbines, hereafter referred to as WF1 to WF5. The number of turbines in the cross-wind, North-South, direction is always 20. In the West-East direction the number of turbines varies from 10 to 60. This means that the smallest wind farm is 2.5 times larger than Horns Rev I, but the number of turbines in the stream-wise direction is similar. The turbine's hub is at 70 m above the surface and the turbine rotor diameter is 80 m. The turbine spacing is similar to that of Horns Rev I, 560 m in the x and y direction. A single turbine occupies with this layout an area of 0.3136 $\mathrm{km^2}$ and the total wind farm area varies consequently from 62 $\mathrm{km^2}$ to 376 $\mathrm{km^2}$. The rated capacity density is 6.4 $\mathrm{W\,m^{-2}}$. The wind farm size of the largest wind farm is still smaller than the smallest wind farm in Adams and Keith (2013), however its total nominal capacity of 2.4G W is far larger than any planned wind farm. The different wind farm properties are summarised in Table 7.1. For the simulations the power and thrust curves were obtained through WA^{s}P. The most important characteristics are summarised in Table 7.2.

Table 7.1: Wind farm characteristics of the sensitivity simulations

	WF1	WF2	WF3	WF4	WF5	WF6
Wind farm extension x (km):	5.6	11.2	16.8	22.4	28.0	33.6
Wind farm extension y (km):	11.2	11.2	11.2	11.2	11.2	11.2
Turbines per grid-cell:	4	4	4	4	4	4
Capacity Density $\left(\mathrm{W\,m^{-2}}\right)$:	6.4	6.4	6.4	6.4	6.4	6.4

Table 7.2: WRF Model Configuration of the sensitivity experiment

$\lvert U_0\rvert$ $\left(\mathrm{m\,s^{-1}}\right)$:	4.9 / 5.4 / 6.4 / 8.0 / 9.6 / 11.3 / 13.5 / 16.2 / 18.5
Wind direction (°)	270
Grid points (nx,ny,nz):	150, 40, 40
Horizontal grid spacing (m):	1120
Wind farm schemes:	EWP / WRF-WF / ROTOR-DRAG

7.1.4 WRF-WF scheme adjustment

In the WRF model default set-up, a wind velocity independent relation between the thrust and power coefficient is used. To overcome this simplification, both the turbine specific thrust and power coefficient have been used.

7.1.5 Single Wind Speed Regime

First we analyse the wind speed development within the largest wind farm and the related power production for two wind speeds.

In Fig. 7.1 the normalised velocities for the largest wind farm for two exemplary wind speeds are shown. For the low upstream wind speed, all three approaches converge to a

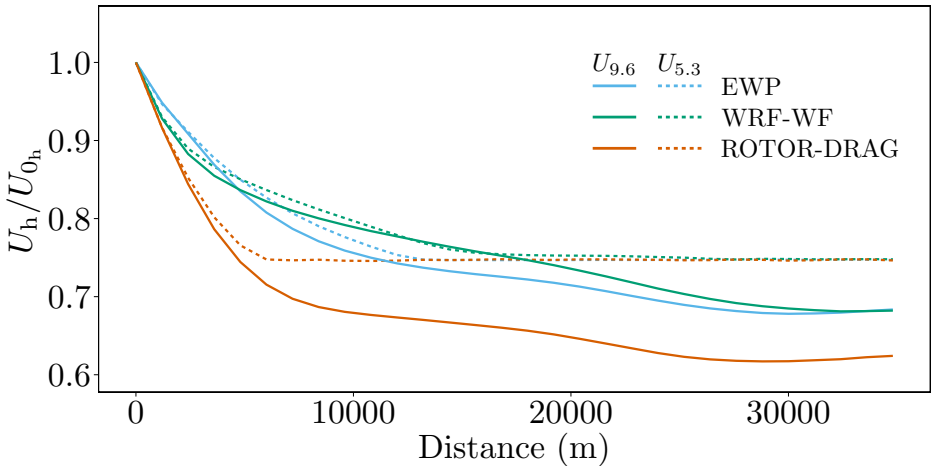

Figure 7.1: Downstream development of the normalised velocity within the largest wind farm. The velocity is averaged over the two central wind farm rows. The normalised velocity with a 5.3 $\mathrm{m\,s^{-1}}$ and 9.6 $\mathrm{m\,s^{-1}}$ upstream wind speed are indicated with dashed and solid lines, respectively.

constant velocity deficit after less than 20 km. Whereas, for the higher upstream velocity the normalised velocity in the EWP and WRF-WF still converge to the same asymptotic wind speed at the end of the wind farm. Furthermore, a circa 5% lower normalised velocity for the ROTOR-DRAG approach can be seen. With increasing wind speeds, the difference in normalised velocities between the single approaches becomes larger. For the highest considered up-stream velocity $\left(18.5\,\mathrm{m\,s^{-1}}\right)$, no equilibrium was reached within the wind farm in any of the approaches. The normalised velocity at the end of the wind farm was for that wind speed the largest in the WRF-WF and the lowest for the ROTOR-DRAG scheme. The bias between WRF-WF and the EWP approach was

around 4% and between the WRF-WF and ROTOR-DRAG approach 10%. This leads to the conclusion that the differences in power production between the schemes increase with wind speed. Given the results in Fig. 7.1 we expect the wind farm size to be more sensitive for higher wind speeds, since the wind speed reduction continues even at the end of the largest wind farm (not shown).

Fig. 7.2 shows a contour plot of the actual power production per turbine for the largest wind farm, WF6, with an upstream wind speed of 9.6 $\mathrm{m\,s^{-1}}$.

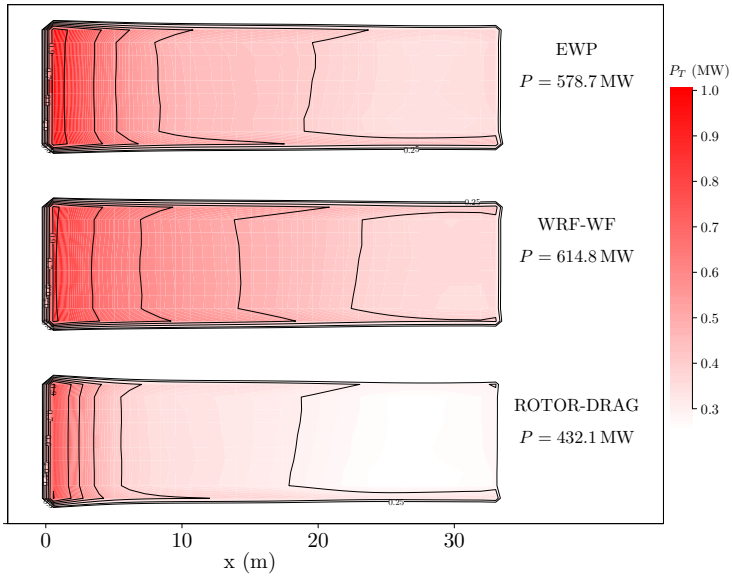

Figure 7.2: Contour plot of the power production for the $U_{9.6}$ simulation. Top: EWP approach, centre: WRF-WF approach and Bottom: ROTOR-DRAG approach. The total wind farm power production, P, is denoted on the right side.

The total power production for the reference simulation is 1362.9 MW. The power production estimation is in the WRF-WF scheme 6% and 30% higher compared to the EWP approach and ROTOR-DRAG approach, respectively. Furthermore, the contour lines in the EWP and ROTOR-DRAG approach show a higher power production in the southern part of the wind farm, whereas the contour lines in the WRF-WF are rather symmetric in the north and south. One reason for the different behaviour could be explained by the turning of the flow due to the Coriolis forcing, which did not occur in the WRF-WF scheme.

7.1.6 Wind Farm Averaged Power Curve

In this section the wind farm averaged power production as a function of wind farm size and wind speed is examined. The power curve relates the upstream wind speed to the turbine power production. Due to the slowing down of the wind speed in the wind farm, we expect the power curve to decrease with increasing wind farm size. However, of importance is to find out if for the considered wind farm sizes an asymptotic curve is reached. The density at hub-height was in the simulations $\rho_{mod} = 1.152\,\mathrm{kg\,m^{-3}}$.

In Fig. 7.3 we show the wind farm averaged power curves for the three wind farm schemes and all wind farm sizes. The V80 power curve from WA^{s}P is plotted in black. It is obtained with a atmospheric density $\rho_{mes} = 1.225\,\mathrm{kg\,m^3}$. The model power output is corrected towards the V80 power curve by multiplication with the ratio ρ_{mes}/ρ_{mod}. The

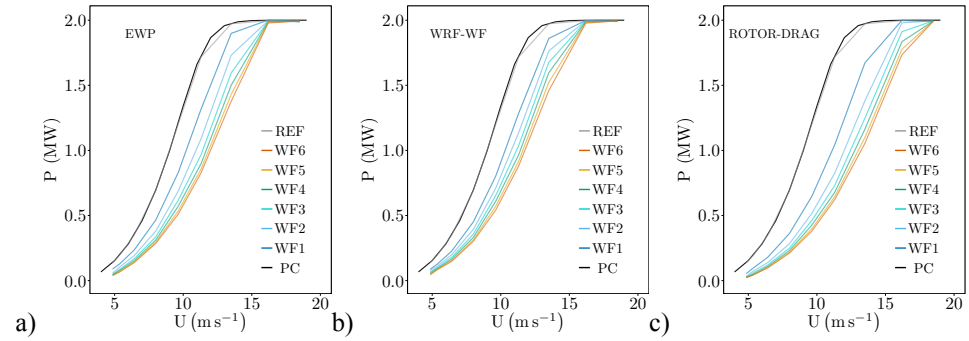

Figure 7.3: Average turbine power curve for the three different approaches. a) EWP, b) WRF-WF and c) ROTOR-DRAG. The colours are used to indicate the different wind farm sizes. The back line represents the reference V80 power curve and the grey line that one of the reference simulation without turbines.

V80 power curve overlaps, as expected, with the power curve in the reference run. In all three approaches the power production starts to diverge due to turbine shadowing at lower speeds. Afterwards they converge again at high velocities where the rated power is reached. The wind farm averaged power curve starts to converge with increasing wind farm size. This means that the power density estimation for the largest wind farm is expected to be valid as an asymptotic limit. It seems that the power production in the EWP scheme converges slightly faster. Conforming with the previous section we find that the power production in the ROTOR-DRAG approach is lower compared to the other schemes. Especially for high wind speeds, where the power productions in the EWP and WRF-WF scheme are already independent of the wind farm size, a wind farm size dependency can be found in the ROTOR-DRAG approach. Only at the highest upstream wind speed $\left(18.5\,\mathrm{m\,s^{-1}}\right)$, the power production becomes wind farm size independent.

7.1.7 Power Density Estimation

Similarly to what is shown in Fig. 4 in Adams and Keith (2013), we compare the actual power production to the expected power production density. The expected power density is obtained by applying Eq. (6.8) to the unperturbed wind speed at hub-height. The actual power density is obtained with the inclusion of the turbine-induced drag to the model. In the power density estimation we consider six different wind farm sizes, three climates and three wind farm schemes. The selected climates are representative for different regions. The climate C1 is similar to that one observed at the Golf of Suez (Saleh et al., 2012), the climate C2 is an example for a wind climate with a very narrow wind speed distribution and a high average wind speed as can be found in locations with trade winds. The climate C3 is similar to wind climates in the North Sea (Sommmer, 2002). The av-

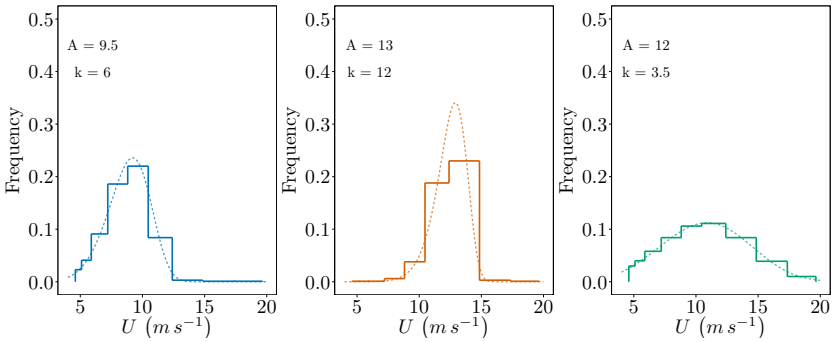

Figure 7.4: The three wind climates C1, C2 and C3 at hub height are plotted from left to the right. The Weibull distribution is plotted in dotted lines and its parameters are indicated on the top of the plot. The simulated distributions are indicated with the histograms.

erage hub-height wind speeds are respectively 8.9 $\mathrm{m\,s^{-1}}$, 12.6 $\mathrm{m\,s^{-1}}$and 10.9 $\mathrm{m\,s^{-1}}$for the three wind climates C1, C2 and C3. We obtained a slightly higher shape parameter k, since the simulated wind speeds ranged only from 4.8 $\mathrm{m\,s^{-1}}$to 18.5 $\mathrm{m\,s^{-1}}$. Especially for the climate C2 a large shape parameter is used, to obtain a climate for narrow wind speed distribution with an high average. In Fig. 7.4 we plotted the Weibull distribution of the considered climates at hub-height.

Figure 7.5 shows the actual power density, P_a, versus the expected power density, P_e, for the different wind farm parametrisations. The wind farm efficiency decreases with increasing wind farm size for all wind farm approaches. This is in line with the findings in Sect. 7.1.6. A clear climate dependency is found, the climate with the largest average wind speed, has the highest actual power production. For none of the approaches an actual power limit seems to be reached. The spread between the power production of the different wind farm sizes, increases somewhat with an increased expected power. This

behaviour is more pronounced for the ROTOR-DRAG approach. In the ROTOR-DRAG scheme no sub-grid scale wake expansion is considered, consequently the interaction between turbine containing grid-cells is overestimated, which leads to smaller yields. Therefore, it can be expected that a saturation takes place in the WRF-WF and EWP schemes with an increased turbine density.

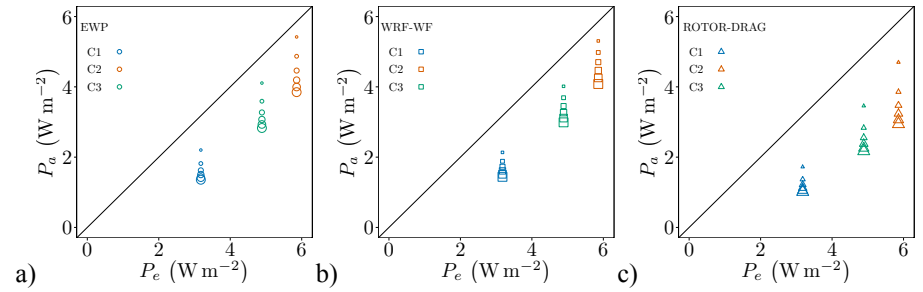

Figure 7.5: Actual power density, P_a, versus the expected power density, P_e, for the 3 wind farm approaches: a) EWP, b) WRF-WF and c) ROTOR-DRAG. The various colours indicate the climate and the symbol's size is related to the wind farm size from 62 km^2 to 376 km^2.

Figure 7.6 shows the actual power density, P_a, as a function of the expected power density, P_e, for the smallest and largest wind farm, the wind climates and the wind farm parametrizations. The results from the small ($2.7{\cdot}10^3$ km^2), medium ($3.0{\cdot}10^3$ km^2) and large ($2.7{\cdot}10^5$ km^2) wind farms in Adams and Keith (2013) serve as a reference and are indicated by the diamonds (black). A point on the diagonal would represent a wind farm without wake losses. The actual power density in Adams and Keith (2013) converges to around 1 W m^{-2}as the size of the wind farm increases. The point with a very high expected power density of around 9.0 W m^{-2} is obtained from a large wind farm ($2.7{\cdot}10^5$ km^2) with a capacity density of 32 W m^{-2}. This wind farm had a very low efficiency due to intense turbine shadowing effects. This is expected, since wind farms with larger turbine spacings, such as Horns Rev I, show considerable lower wake impacts compared to wind farms with smaller turbine spacings, such as Lillgrund (Peña et al., 2013). The simulations performed here show that due to a constant turbine density, the expected power is a function of the wind climate only. Regarding the actual power density, we find that in all simulations the power production was higher than 1 W m^{-2}. Therefore, we can suggest that the two simulation periods in Adams and Keith (2013) had slightly worse wind conditions than the C1 climate in this simulation and thus are not representative of an optimal wind farm.

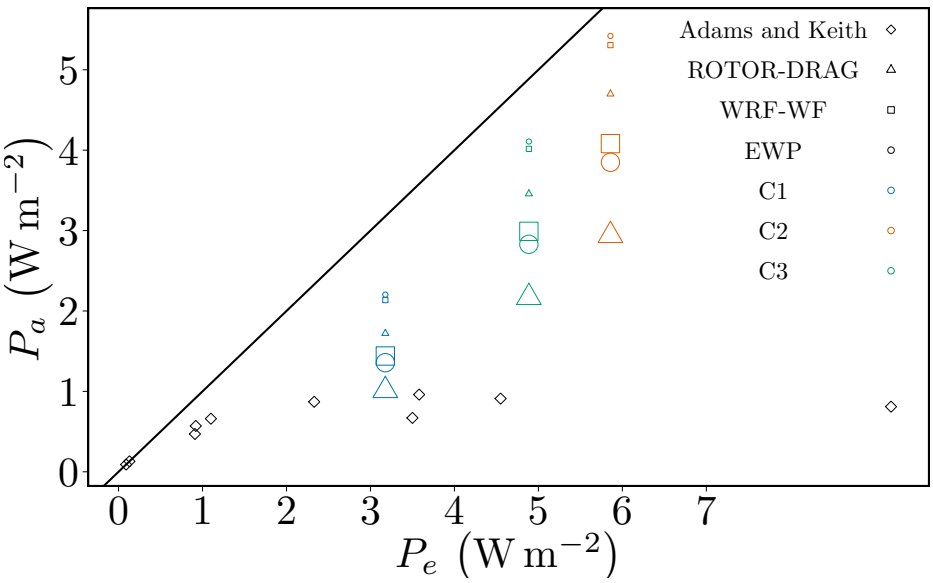

Figure 7.6: Actual power density versus expected power density for the largest and smallest wind farm, wind climates and wind farm schemes. The colour of the symbols indicate the wind climate (C1, C2, C3), their shape the wind farm approach and their size is related to the wind farm size. The diagonal line represents wind farms without wake losses. The results of Adams and Keith (2013) are indicated by diamonds.

7.1.8 Discussion & Conclusion

In this section we used a mesoscale model to investigate possible limits to the power production density as a function of the wind farm size and the hub-height wind climate. Mesoscale models allow us to simulate atmospheric flows over large areas, however lack horizontal resolution. Therefore, the effect of wind turbines are unresolved and have to be parametrised. To add robustness in this regard three wind farm schemes are used. The low horizontal resolution, limits also the prediction of the local, turbine, power production. It estimates instead a grid-cell averaged power production. The results show that the model power density estimation of around 3.5 W m^{-2} (C3 wind climate, $\rho = 1.152\,\mathrm{kg\,m^{-3}}$) for the smallest wind farm, which has 10 turbines in the downstream direction, is roughly comparable to the measured long term averaged power density at Horns Rev I, 3.98 W m^{-2} (Petersen et al., 2013). Differences are expected to occur, since in the real wind farm the intensity of turbine-interaction varies strongly with the wind direction.

From Sect.7.1.6, we find that the largest wind farm with a total rated capacity of 2.4 GW is expected to behave similar, in terms of power density, to the small, medium and large wind farms in Adams and Keith (2013). In Sect. 7.1.7 we compared the actual power production density for three different climates, six different wind farm sizes and three wind farm parametrisations, to the results of Adams and Keith (2013). We find that for all climates, all approaches and all wind farm sizes, the power production density was higher than the upper limit in Adams and Keith (2013). From the results presented in Adams and Keith (2013), we can expect that an increased installed power density will not necessarily lead to higher yields. Exceptions are wind climates which allow for specific wind farm layouts. Instead from the presented simulations we find that the power production density increases for better wind conditions, even for very large wind farms. These results encourage the development of large turbines and suggest that the power production of large wind farms lead to higher yields.

7.2 Coupling to Microscale Models

In Chapter 4 several wind farm parametrisations have been introduced. These parametrisations model the effects of unresolved turbine-induced wakes. Microscale models on the other hand, with their fine mesh, resolve the flow around turbines. Examples are ElipSys 3D (Réthoré et al., 2009) or CRESflow-NS (Prospathopoulos and Chaviaropoulos, 2013). The linear wake model Fuga (Ott et al., 2011) provides local flow information. In this section the detailed flow information of the microscale model is used to determine the grid-cell averaged velocity deficit. In this way the unresolved turbine interaction is accounted for. The "coupling" is realised through look-up tables, guaranteeing fast computational times. The advantage is that any microscale model can be "coupled" in a rather uncomplicated way. In this section the principles will be described.

Conceptually, one would aim to obtain wind speed and wind direction dependent averaged turbine-induced velocity profiles from a microscale model. However, several problems arise. Usually wind farms extend over several model grid-cells and consequently upstream turbines influence turbines in downstream grid-cells. This induces double counting if a grid-cell averaged velocity is determined directly from the flow field, since it is composed of multiple wakes. The attempt to separate the accumulative wake into separate wind turbine wakes is not possible without modifying the microscale model outputs. One option could be that that each turbine would produce its wake additionally in a separate domain. This however, requires a considerable amount of additional computation. A simpler approach is to store each turbine's local upstream hub-height velocity or its total amount of thrust applied to the flow. These values are then tabulated as a function of the upstream wind speed and direction. Afterwards this table is used in the mesoscale model for the estimation of the total turbine thrust in Eq. (4.16). The grid-cell averaged vertical thrust distribution however needs still to be parametrised. Here

one can use for example the simple ROTOR-DRAG WRF-WF or EWP approach. The main advantage is that the information of the wake is included in the turbine hub-height velocity. Interpolations as a function of the look-up table will still be involved and the vertical distribution of the thrust will be parametrised.

7.2.1 Implementation

For the initialisation the wind farm parametrisation requires turbine specific total turbine-induced thrusts as a function of the upstream wind farm wind speed and wind direction, with a precision of ΔU and $\Delta\phi$. In case the microscale model include stability, a Richardson number dependency can be added. In the parametrisation we define the upstream wind speed, which is wind direction dependent, to occur one grid-cell ahead of the wind farm. Optional the microscale model's air density can be added. In case it is not provided, we assume the air density in the microscale model to be $\rho = 1.225\ \mathrm{kg/m^{-3}}$, as defined for the International Standard Atmosphere. With this information the thrust for every specified wind speed in the table is additionally tabulated.

For every model time-step the wind farm upstream wind velocity and wind direction is determined. From the look-up table we obtain from the upstream velocity through interpolation a turbine i specific thrust, $T_m(i)$. To apply Eq. (4.18) and Eq. (4.19) to the RANS equation, the local hub-height wind speed, U_0 and the thrust coefficient, C_T, have to be obtained. The grid-cell averaged wake extension $\overline{\sigma}$ can afterwards be obtained from Eq. (4.15). One way to obtain the unknown hub-height and thrust coefficient is through the thrust equation on the left hand side of Eq. (4.16). It can be written as

$$T(U,C_T) = \frac{1}{2}\rho\, C_T\, A_0\, U^2 = \frac{1}{2}\rho \left(\frac{\Delta C_T}{\Delta U}\,(U - U_{\mathrm{in}}) + C_{T_{\mathrm{in}}} \right) A_0\, U^2, \tag{7.1}$$

where $T(U,C_T)$ is the thrust, ρ the pre-defined density, A_0 the turbine rotor area, U_{in} and $C_{T_{\mathrm{in}}}$ the velocity and thrust coefficient of the lower interpolation limit and ΔU and ΔC_T the velocity and thrust coefficient difference between the lower and upper interpolation limit. The lower limits are given from the upstream hub-height velocity and the difference is a function of the look-up table's precision. Now starting from the velocity $U_{\mathrm{in}}$the velocity U is increased until $T(U,C_T)$ exceeds the microscale model thrust $T_m(i)$. The velocity and thrust coefficient from final step are used as hub-height velocity and thrust coefficient in Eq. (4.18) and Eq. (4.19).

7.2.2 Idealised case

In this section we compare the EWP approach, to the three different microscale model coupling approaches. The WRF model is set-up in idealised case mode, similar to Sect. 4.2. For this case the horizontal resolution is 2240 m. In this section only the near wind farm

wake is compared with Horns Rev I met mast data. For this purpose only a single model simulation with a converged wind speed of 7.97 $\mathrm{m\,s^{-1}}$and wind direction of 269.4° is run. We use the turbine-induced thrusts from the microscale model CRESflow-NS (Prospathopoulos and Chaviaropoulos, 2013). The CRESflow-NS has been performed for neutral conditions in one direction only. The microscale model thrusts are used for three approaches. In the first approach, CRES-EWP, the vertical thrust distribution is obtained as described in the previous Sect. 7.2.1. The second approach, CRESS-ROTOR, is based on the ROTOR-DRAG approach presented in Sect. 4.2.2. The hub-height velocity is determined from Eq. (7.1). The final approach, CRESS-ROTOR-FA, is similar to the CRESS-ROTOR one. This time the wind farm is aggregated in one column only. The results and a description are presented extensively in Badger et al. (2013). Figure (7.7) shows the normalised velocity for the four approaches. The normalised ve-

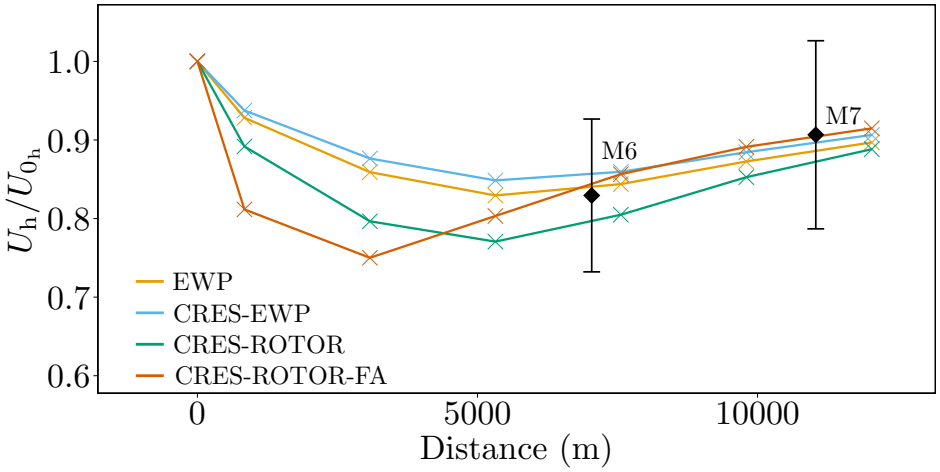

Figure 7.7: Normalised velocity at hub-height, U_h/U_{0_h} for the EWP (orange), CRES-EWP (blue), CRES-ROTOR (green) and the CRES-ROTOR-FA simulation (red), see Badger et al. (2013).

locity in the EWP and the CRES-EWP approach are similar. The velocity deficit for the EWP approach, in which we only account for grid-cell interaction, is however deeper. In Prospathopoulos et al (2013) it can be found that the CRESflow-NS model estimated the power deficit for the flow directions $270° \pm 15°$ extremely well from the fourth turbine column onwards. This suggests that the wake expansion in the EWP approach is estimated well, since the normalised velocity of the CRES-EWP approach is very similar to that one in Prospathopoulos et al (2013). However, we notice that with the velocity reduction in the EWP is larger than with the CRES-EWP approach. This means that the interaction between grid-cells is stronger than between single turbines. The downstream development of the normalised velocity for the CRESS-ROTOR approach is very similar to that found in Fig. 4.7. Interesting is the wake recovery from the aggregated wind farm,

represented with the red line. In this approach the turbine thrusts include still the turbine interaction, simulated with the CRESflow-NS model. This approach fits the measurements at mast M6 and M7 very well, despite the low normalised velocity within the wind farm. However, complications in applying a accumulative thrust to one turbine column will arise, when the flow wind direction is not aligned with the model grid. Furthermore, it should be investigated if the aggregated thrust from large wind farms cause model instabilities. Finally it can be expected that the concentrated force, affects the atmosphere around the wind farm differently.

7.3 Impact of Wind Farm Wake on Neighbour Wind Farms

The study of wind farm interaction will gain importance in the near future, since the number of offshore wind farms, especially in the North Sea, is expected to increase significantly, see Fig. 2.1. In this section we show first results of a sensitivity study on wind farm interaction.

7.3.1 Model Set-Up

Similarly to previous simulations, the model is run in the idealised mode. Only the EWP scheme is used. The configuration is similar to that one used in Chapter 2 and its most important settings are shown in Table 7.3.

Table 7.3: WRF Configuration for the wind farm interaction experiments

$\|U_0\|$ ($\mathrm{m\,s^{-1}}$)	7.97
Grid points (nx,ny,nz):	80, 30, 40
Horizontal dimension in x, y (km, km):	89.6, 33.6
Horizontal grid spacing (m):	1120
PBL-Scheme:	MYNN (1.5)

We study the wind farm interaction between two equally sized wind farms similar to Horns Rev I. With the given resolution this results in a turbine density of 4 turbines per grid-cell. The wind farms extend 5 grid-cells in the West-East direction and 4 in the North-South one. The sensitivity to the influence of the upstream wind farm is examined for three different wind farm spacings, namely 8 km, 15 km and 22 km, hereafter referred to as WF08, WF15 and WF22. This is equivalent to 1.6, 3 and 4.4 wind farm spacings. The three different simulations are specified in Table 7.4.

Table 7.4: Experimental set-up for the wind farm interaction experiments

	WF08	WF15	WF22
Wind farm Separation (km)	8×1.12	15×1.12	22×1.12

For each simulation the wind farms are aligned, such that the downstream wind farm is in the wake of the upstream one. We study the interaction for one wind direction only, to obtain the impact for the worst case scenario.

7.3.2 Velocity Recovery and Wind Farm Production

In Fig. 7.8 the normalised velocity for the WF08, WF15 and WF22 run, from top to bottom, are plotted. We find that in the WF08 run the downstream wind farm is still in the

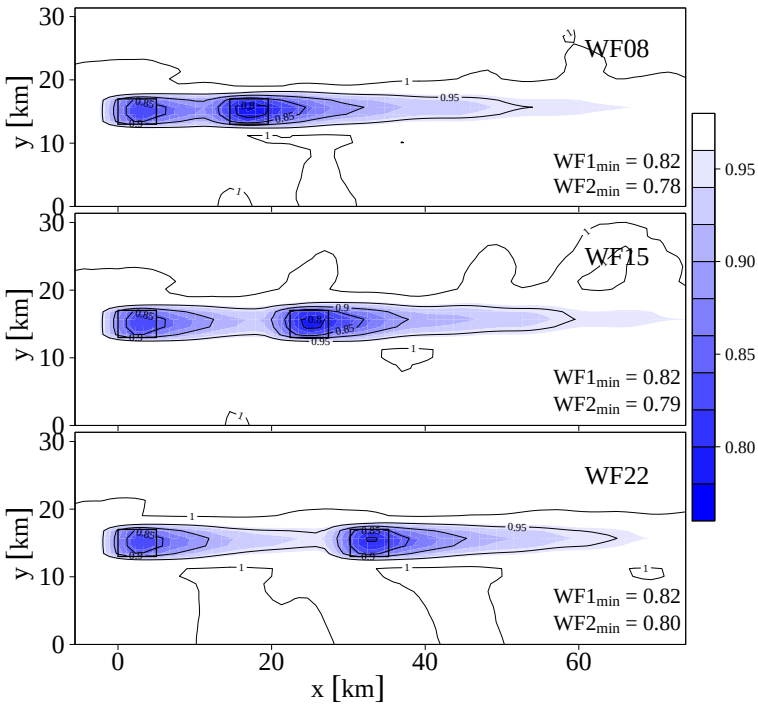

Figure 7.8: The normalised velocity for the WF08, WF15 and WF22 simulation are plotted on the top, middle and bottom, respectively. The wind farms are marked by a rectangular box.

deep wake of the upstream one, causing a larger velocity reduction at the downstream

WF with respect to the other runs. The wind farm wake extension after the second WF is very similar in al three simulations.
In Fig. 7.9 we show the power production, as defined in Eq. (6.8), for the WF08, WF15 and WF22 simulations. The upstream wind farm production depends slightly on the wind

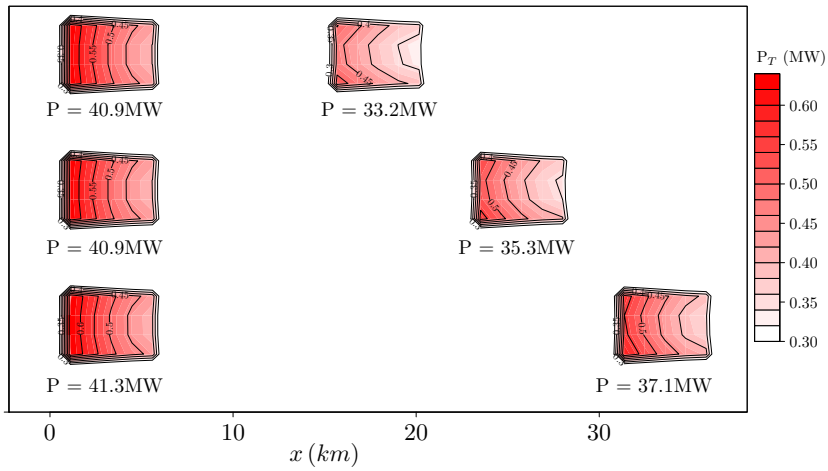

Figure 7.9: Power production for the WF08, WF15 and WF22 run from top to bottom.

farm separation. The higher production of the upstream wind farm is achieved for the largest separation. One reason could be, that for small wind farm separations, the negative pressure gradient in front of the downstream wind farm is influences the velocity field in the upstream wind farm slightly. The normalised power is 0.81, 0.86 and 0.90 for the WF08, WF15 and WF22 simulations, respectively. Here we normalised with the upstream wind farm power. In this study the power deficit at the second wind farm is close to a linear function of the distance.

The second wind farm is still in the wake of the upstream wind farm (Fig.7.8). Therefore, due to the larger velocity gradients, the flow will be more turbulent at the first turbine of the downstream wind farm, than it is at the first turbine of the upstream wind farm. The higher turbulence levels are disadvantageous for the loads on the blades. However, since the turbulence is connected to larger momentum fluxes from aloft, they could be beneficial regarding the velocity reduction in the downstream wind farm. In Fig. 7.10 we show the normalised velocity within all wind farms. The velocity is this time normalised by the velocity of the first turbine. We notice that the velocity development within the upstream wind farm is indistinguishable. Furthermore, with decreasing wind farm spacings, the velocity deficit reduces within the wind farm, due to the larger momentum fluxes. As shown in Fig. 7.9, this positive feature is not able to compensate for

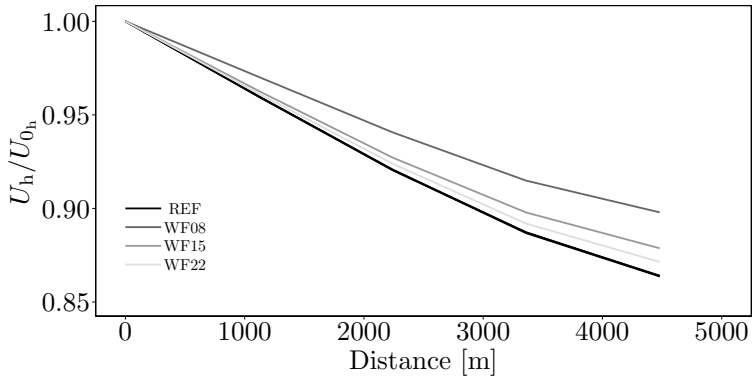

Figure 7.10: Normalised velocity within all wind farms as a function of the distance from the start of the first wind farm. The black line represent the normalised velocity of the upstream wind farms. The velocities are normalised with the velocity of the first wind farm grid-cell.

the reduced upstream wind farm velocity.

7.3.3 Conclusions

These first results show significant power losses for the downstream wind farm. Even at distances of around 25 km, wind farms similar to Horns Rev I will affect downstream wind farms. This is, however, the worst case scenario. Moreover, we have to consider that the wind farm interaction is simulated for a single wind direction only. For a wind farm separation of approximately 25 km, this would require unchanged wind direction for at least 50 minutes with an upstream wind speed of 8 m s^{-1}.

7.4 Atmosphere-Ocean Interaction

In the final part the influence of the offshore wind farm to the near surface is qualitatively analysed. In future with an increased installed offshore power, investigations of ocean feedback on the changed atmospheric forcing from large wind farm can become of interest. Broström (2008) showed by forcing a 1.5 layer ocean model with a changed wind farm induced wind stress, that up-welling, which is sensitive to the curl of the wind stress, was triggered under steady conditions. In this regard, the vertical curl component of the wind stress of the EWP and WRF-WF scheme has been compared.

7.4.1 Model Set-up

The simulation was performed in the idealised case mode as described in Chapter 4. The model is initialised with a constant geostrophic wind, that converged to a westerly wind speed with 7.93 $\mathrm{m\,s^{-1}}$ at 70 m. The hypothetical wind farm consists of 80 2 MW with a hub at 70 above mean sea-level wind turbines. The wind farm contains 5 grid-cells in the West-East and 4 grid-cells in the North-South direction. The turbine density per grid-cell is 4. The model configuration is shown in Table 7.5.

Table 7.5: WRF Configuration for the ocean feedback experiments

Wind speed $\left(\mathrm{m\,s^{-1}}\right)$	7.93
Wind direction $(^\circ)$	270
Grid points (nx, ny, nz):	80, 30, 40
Horizontal dimension x, y (km, km):	89.6, 33.6
Horizontal grid spacing (m):	1120
Wind farm extension (nx $\times$ ny):	5×4
Turbines per grid-cell	4
Boundary condition:	OPEN
PBL scheme:	MYNN (1.5)

7.4.2 Velocity Field at the lowest Level

To be independent of the diagnostic model friction velocity, $u_\star$, the drag formulation from Garratt (1977) has been used to derive the wind stress τ. The friction velocity reads, $\tau_i = \rho\, C_D |U| U_i$, where the index i represents the directions x and y, C_D the drag coefficient and $|U|$ the absolute horizontal wind velocity. The drag coefficient was obtained from the logarithmic wind profile assumption, $C_D = [\kappa / \ln(z/z_0)]^2$. κ is the Von Kármán constant and z_0 the surface roughness length. In all simulation the sea roughness length was set to $z_0 = 2 \cdot 10^{-4}$ m and the Von Kármán constant was set to 0.4.

The vertical component of the curl from in Fig.(7.11a) looks similar to that one depicted in Broström (2008) (Fig.4), which could lead to upwelling. In Fig.(7.11b) we observe a double dipole structure, caused by the speed-ups and slow-downs at the lowest model level (at approximately 4 m). The curl is far less pronounced, than that one from the EWP scheme. Future wind farm wake measurements from offshore wind farms have to give additional information about the wind field in the near surface region.

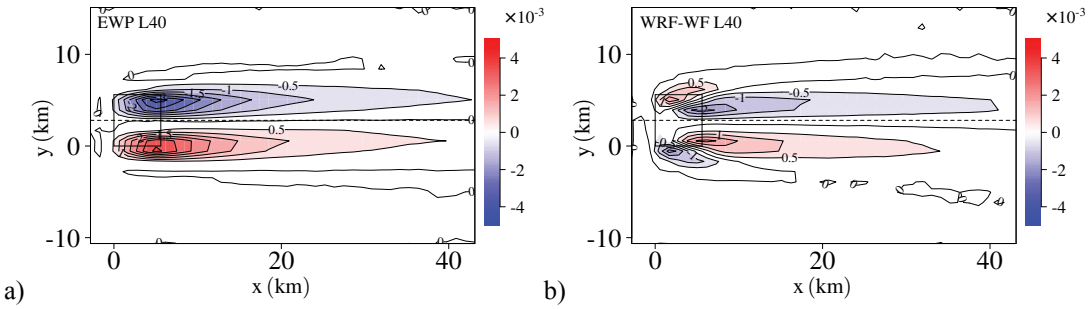

Figure 7.11: Vertical component of the Curl of the wind stress $\left(\mathrm{m\,s^{-2}}\right)$ from the lowest model level. a) EWP scheme b) WRF-WF scheme.

8

Conclusions

Wind energy production has matured significantly over the past decades. Its main advantage is its high safety compared to nuclear energy and its low carbon food print compared to conventional combustion of fossil fuels. Policy makers throughout the globe have adapted to a certain amount their plans towards increasing the fractions of renewable energy production. Offshore wind energy production has high potentials, since wind resources are by nature higher over the smooth water surfaces. The installed offshore capacity today is still only a small fraction of what has been planned. Fig 2.1 shows with red and the green areas, the planned and already installed wind farms. To predict possible restrictions in power production for large wind parks, as well as their possible influence to the environment, a better understanding in the interaction between wind turbines and the atmosphere is necessary.

Until today, investigations on the influence of wind turbines on the atmosphere for a large variety of scales have been carried out. On smaller scales, turbine wakes are examined, whereas on large scales the interaction of entire clusters of wind farms with the atmosphere is studied. It is evident that the larger the scales involved, the less accurate the local flow can be described. Therefore, the consequences of the simplifications should be investigated.

Throughout this thesis wind farms have been simulated with mesoscale models. The horizontal resolution of mesoscale models is in between the resolution of high resolution models and global circulation models. The downstream evolution of a single turbine-induced wake remains unresolved. However, the relatively high vertical model resolutions allow the vertical wake structure to be described fairly well. The challenge is to describe the unresolved processes in such a way, that an accurate as possible velocity flow within and in the wake of the wind farm is obtained. The velocity development within the wind farm is of importance for the estimation of power production, whereas the wind farm wake flow is of importance for wind farm interaction.

Several approaches to the parametrization of wind farms are published. The basic principle in these parametrisations is very similar. A local turbine drag force is applied in the horizontal flow directions and a turbine induced turbulence is added to the turbulence kinetic energy equation. The latter source term accounts implicitly for the sub-grid scale wake expansion. In this thesis a somewhat different approach is proposed. Here, we

assume that the unresolved wake expansion is mainly due to the turbulent shear caused by vertical velocity gradients between the environmental flow and the velocity field in the turbine wake. The shear is, however, already part of the model turbulence kinetic energy equations, but acts only on horizontal scales in the order of the grid size. In the parametrisation we account for the unresolved turbine-induced wake expansion with a simple diffusion model. The resulting grid-cell averaged velocity deficit is then added as a drag term to the model equations. In this fashion the model is forced by an estimated velocity deficit and the related grid-cell averaged shear is afterwards determined by the model.

The introduced parametrisation, together with the scheme implemented in the Weather Research and Forecast model, have been evaluated against long term averaged wind turbine and met mast measurements from the offshore wind farm Horns Rev I. It has been shown that the model wind fields fit with wind direction averaged measurements. Among the advantages of the introduced approach are its vertical resolution independence, and the more reasonable turbulence kinetic energy fields it produces. Regarding the vertical position of the maximum velocity deficit, which is in the WRF parametrisation up to the upper turbine blade tip, we expect remote sensing measurements in the vertical direction to provide further insights.

The introduced approach has been used to investigate the interaction of a hypothetical large offshore wind farm, situated to the North of San Francisco, with the lower marine atmosphere. For a one year simulation we found that the influence of the wind farm was not limited to the marine boundary layer only, but wind farm induced gravity waves caused anomalies in temperature and humidity in the lower troposphere. The very persistent weather conditions favoured the existence of gravity waves. The findings of the simulations of the California simulation have been used to study the effect of different atmospheric conditions to the velocity restoring components with an idealised "case" model set-up. We found a variation of the wind farm power production up to 4% for the selected atmospheric conditions. We noticed that unfavourable upstream pressure gradients were balanced by favourable conditions within the wind farm.

In the final part of the thesis we used the mesoscale model to investigate the influence of the wind climate to the wind farm production. With the increasing installed wind power this is an important issue. A previous investigation suggested a possible limit in power production for very large wind farms of around 1 $\mathrm{W\,m^{-2}}$. This result was obtained from a 10 days and a 1 month simulation for different very large wind farm sizes and densities. In our study we examined a sensitivity for different wind farm sizes from 400 MW up to 2.4 GW, to different climates with 3 wind farm parametrisations. We found that the ratio between the actual production and the estimated power remained, for the different climates, almost constant for the small wind farm. Even for the largest wind

farms no saturation was found with the introduced and WRF wind farm parametrisation. The results suggest that the power production depends mostly on the wind climate. For wind farms with conventional turbine spacings, it can be expected that larger wind farms will still give larger yields. Instead, an increased turbine spacing is likely to cause a power production saturation.

.1 Appendix: Coriolis Effects on the Wind Field

Fig. 1 shows the normalised velocity U_h/U_{0_h} for the EWP and the WRF-WF scheme. Here we used U_h and U_{0_h} for the hub-height velocity in the wind farm and reference simulation, respectively. The vectors indicate the (magnified) direction of the wind velocity. The U velocity component is defined in the West-East direction and the V velocity component in the South-North direction. The wind farm extends 5 grid-cells in the West-East and in the South-North direction. The most southwesterly wind turbine is defined at the coordinate (0,0). The wind direction in the reference simulation was 270.06°.

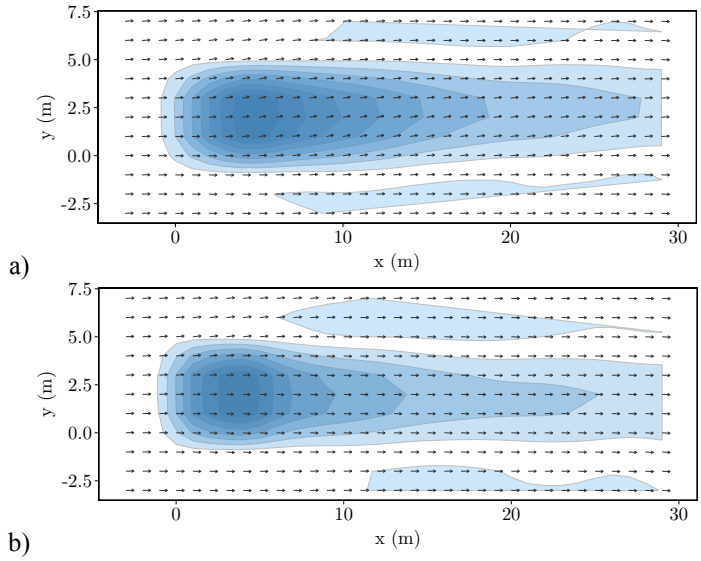

Figure 1: Normalised velocity, U_h/U_{0_h}, for the L40 simulation (see Sect. 5.1.4). Here U_h and U_{0_h} denote the hub-height velocity of the wind farm and reference simulation, respectively. The contour lines indicate the velocity reduction and the arrows indicate the magnified wind direction. Figure a) is for the EWP scheme and b) for the WRF-WF scheme.

The velocity field at the end of the wind farm is directed towards the left in the EWP (Fig. 1a). The wind direction at the final wind farm row ranges from 270.11° to 270.97° and it returns back to 270° in the wind farm wake. Fig. 1b shows instead a flow divergence within the wind farm. At the end of the wind farm the wind direction ranges from 269.57° to 270.58°. One explanation for the flow divergence could be the superposition of the Coriolis effect, that deflects the reduced wind speed to the North, and the intense turbulence fluxes that transports the negative V velocity component down to the hub-height. Interesting is that at the wind farm's centre, both effects seem to compensate each other. In the wind farm wake we find that the flow is slightly turned to the right.

Future measurements have to provide additional insides. However, this task can be challenging, since remote sensing data does not measure the wind directions. However, Light Detection And Ranging (LIDAR) measurements from velocity profiles in wind farm wakes can provide information of the vertical wake structures at several distances.

Acknowledgements

I gratefully acknowledge the funding provided by the Wind resource assessment audit and standardization (WAUDIT) programme, financed by Marie Curie ESR-FP7. I am thankful to Vattenfall AB and DONG Energy A/S for providing the data from the Horns Rev I offshore wind farm.
Foremost, I would like to express my gratitude to my advisers Andrea N. Hahmann and Jake Badger for their patience, help and continuous support during these three years. Andrea's constructive advices regarding mesoscale modelling have significantly helped in improving the manuscript, while the long and fruitful discussions with Jake, which by far exceeded the time allocated to the project, have substantially contributed in the development of the wind farm parametrisation and its applications. I am particularly indebted to Søren Ott for the extensive and inspiring discussions regarding the fundamental flow behaviour around wind turbines and its modelling, particularly regarding the mesoscale model application.
Furthermore, I would like to thank Alex Hall and the Climate Sensitivity Research Group, Jerry H-Y. Huang, Scott Capps, Xin Qu and Fengpeng Sun for their hospitality and support during my stay at UCLA.
I am glad to have worked in the stimulating research environment at the Risø Campus DTU Wind Energy Department. Special thanks go to my colleagues Rogier Floors, Jesper Grønnegaard Pedersen and Paul van der Laan for the many useful discussions.
Lastly, I want to thank my lovely wife for her patience and support during these years.

Journal Papers

Badger, J., Volker, P. J. H., Prospathospoulos, J., Sieros, G., Ott, S., Rethoré, P.-E., Hahmann, A. N., Hasager, C. Wake modelling combining mesoscale and microscale models. Submitted to *Renewable Energy*, 2013.

Volker, P. J. H., Badger, J., Hahmann, A. H., Ott, S., Implementation and evaluation of a wind farm parametrisation in a mesoscale model. Planned to be submitted in January 2014 to *Boundary-Layer Meteorol.*

Conference Papers

Volker, P. J. H., Badger, J., Hahmann, A. H. and Hansen, K. S. Wind-Farm Parametrisations in Mesoscale Models. *ICOWES*, 2013.

Volker, P. J. H., Badger, J., Hahmann, A. H., Ott, S., Wake effects of large offshore wind farms on the mesoscale atmosphere. *EWEA-Conference*, 2012.

Conference (extended abstract)

Volker, P. J. H., Hall, A., Capps, S. B., Huang, H.-Y., Sun, F., Badger, J. and Hahmann, A. H.. Impact of Wind Farms on the Marine Atmospheric Boundary Layer. *AGU*, 2012.

Volker, P. J. H., Badger, J., Hahmann, A. H. and Hansen, K. S. Outline for a study of wake effects of large offshore wind farms: a study of mesoscale atmosphere andocean feedbacks. *Wake Conference, Visby, Schweden*, 2011.

Volker, P. J. H., Badger, J., Hahmann, A. H., Ott, S., Wake effects of large offshore wind farms - a study of mesoscale atmosphere andocean feedbacks. 7^{th} *PhD Conference EAWE*, 2011.

Reports

Badger, J., Muñoz, P. A. J., Correia, P. M. F., Galiana, S. L., Volker, P. J. H ., Prospathopoulos, J., Mouche, A., Badger, M., Schepers, G., Losada, A. M. P, Montesinos, J. N., Mallafre, I. M., Hansen, K. S., Hasager, C. B. Benchmark report on wake models at the cluster scale. *EERA-DTOC*, 2013.

Prospathopoulos, J., Badger, J., Volker, P. J. H ., Sieros, G., Chaviaropoulos, C., Rethoré P.-E. Physical scale integration (coupled use). *EERA-DTOC*, 2013.

Bibliography

Adams, A. S. and Keith. D. W. A Wind Farm Parametrisation for WRF. AGU Conference, 2007.

Adams, A. S. and Keith. D. W. Are global wind power resource estimates overstated? *Environ Res Lett*, 8, 2013.

Ainsley J. F. Calculating the flow field in the wake of wind turbines. *J Wind Eng Ind Aerodyn*, 27:213-224, 1988.

Badger, J. , Volker, P. J. H. , Prospathopoulos, J. , Sieros, G. , Ott, S., Rethoré, P.-E., Hahmann, A. N., Hasager, C. B. Wake modelling combining mesoscale and microscale models. *Submitted to Renewable Energy*, 2013.

Baines, P. G. Topographic effects in stratified flow. *Cambridge University Pess*, 1995.

Archer, C. L. and Jacobson, M. Z. Evaluation of global wind power. *J. Geophys. Res.*, 110,D12110, 2005.

Barrie, D. B. and Kirk-Davidoff, D. B. Weather response to a large wind turbine array. *Atmos. Chem. Phys.*, 10:769–775, 2010.

Barthelmie, R. J., Pryor, S. C., Frandsen, S. T., Hansen, K. S., Schepers, J. G., Rados, K., Schlez, W., Neubert, A., Jensen, L. E. and Neckelmann, S. Quantifying the Impact of Wind Turbine Wakes on Power Output at Offshore Wind Farms. *J. Atmos. Oceanic Technol.*, 27:1302–1317 , 2010.

Barthelmie, R. J., Larsen, G., Pryor, S., Jørgensen, H., Bergström, H., Schlez, W., Rados, K., Lange, B., Vølund, P., Neckelmann, S., Mogensen, S., Schepers, G., Hegberg, T., Folkerts, L. and Magnusson, M. ENDOW (efficient development of offshore wind farms): modelling wake and boundary layer interactions. *Wind Energy*, 7(3):225-245, 2004.

Bengöl, F., Larsen, G. C., Mann, J., Wake Meandering - An Analysis of Instantaneous 2D Laser Measurements. *J Phys: Conf Ser*, 75, 2007.

Blahak U., Goretzki, B. and Meis, J.. A simple parametrisation of drag forces induced by large wind farms for numerical weather prediction models. *EWEC Conference*, 2010.

Broström, G.. The influence of large wind farms on the upper ocean circulation. *Journal of Marine Systems*, 74:585-591, 2008.

Calaf M., Meneveau C. and Meyers J. Large eddy simulation study of fully developed wind-turbine array boundary layers. *Phys Fluids*, 22:015110, 2010.

Chamorro, L. P., Porté-Agel, F. A Wind-Tunnel Investigation of Wind-Turbine Wakes: Boundary-Layer Turbulence Effects. *Boundary-Layer Meteorol*, 132:129-149, 2009.

Chamorro, L. P., Porté-Agel, F. Effects of thermal stability and incoming boundary-layer flow characteristics on wind-turbine wakes: A wind-tunnel study. *Boundary-Layer Meteorol*, 136:515-533, 2010.

Chen, F., and Dudhia, J. Coupling an advanced land-surface/ hydrology model with the Penn State/ NCAR MM5 modeling system. Part I: Model description and implementation. *Mon. Wea. Rev.*, 129:569–585 , 2001.

Christiansen, M. B., Hasager, C. .B. Wake effects of large offshore wind farms identified from satellite SAR. *Remote Sensing and Environment*, 98:251-268, 2005.

Crespo, A., Hernández, J. Turbulence characteristics in wind-turbine wakes. *J Wind Eng Ind Aerodyn*, 61:71-85, 1996.

Dudhia J. Numerical study of convection observed during the wind monsoon experiment using a mesoscale two-dimensional model. *J. Atmos. Sci.*, 46:3077–3107 , 1989.

Dvorak, M. J., Archer, C. L., Jacobson, M. .Z. California offshore wind energy potential. *Renewable Energy*, 35:1244–1254 , 2010.

Fitch, A., Olson, J. K., Lundquist, J. K., Dudhia, J., Gupta, A., Michalakes J., and Barstad, I.. Local and mesoscale impacts of wind farms as parameterized in a mesoscale NWP model. *Monthly Weather Review*, 140, 3017-3038, 2012.

Fitch, A., Lundquist, J. K. & Olson, J. B. Mesoscale influences of wind farms throughout a diurnal cycle. *Monthly Weather Review*, 141, 2173–2198, 2013.

Frandsen, S. T., Turbulence and turbulence generated structual loading in wind turbine clusters. *Risø National Laboratory, Roskilde, Denmark*, Risø-R-1188(EN), 2007.

Frandsen, S. T., Jørgensen, H. E., Barthelmie, R., Badger, J., Hansen, K. S., Ott, S., Rethore, P.-E., Larsen, S. E. and Jensen, L.E. The making of a second-generation wind farm efficiency model complex. *Wind Energy*, 12:445-458, 2009.

Garratt, J. R. Review of drag coefficients over Oceans and Continents. *Mon Weather Rev*, 105:915-929, 1977.

Gaumond, M., Réthoré, P.-E., Bechmann, A., Ott, S., Larsen, G. C., Peña A. and Hansen, K. S. Benchmarking of Wind Turbine Wake Models in Large Offshore Windfarms. *The science of Making Torque from Wind*, 2012.

Grachev, A. A., Fairall, C. W. Dependence of the Monin-Obukhov stability parameter on the bulk Richardson Number over the ocean. *J of Appl Meteorol*, 36:406-414, 1996.

Hansen, M. O. L. Aerodynamics of Wind Turbines. *James & James*, 2003.

Hansen, K. S. Summary Report: The shadow effect of large wind farms: measurements, data analysis and modelling. *Information Service department*, Risø, 2007

Hansen, K. S. Presentation of Horns Rev offshore wind farm and the Vestas V80 Wind turbine. *Report: EERA-DTOC*, 2012.

Hansen, K. S., Barthelmie, R. J., Jensen L. E., Sommer, A. The impact of turbine intensity and atmospheric stability on power deficits due to wind turbine wakes at Horns Rev wind farm. *Wind Energy*, 15:183:196, 2012.

Hansen, K. S. WP1.1 Wake model performance validations Horns Rev offshore wind farm. *Report: EERA-DTOC*, 2013.

Hirth, B. D., Schroeder J. L., Gunter, W. S. and Guynes, J. G. Measuring a utility-scale turbine wake using the TTUKa mobile research radars. *J. Atmos. Oceanic Technol.*, 29:765–771, 2012

Högström, U., Asimakopoulos, D. N., Kambezidis, H., Helmis, H. and Smedman A. A field study of the wake behind a 2 MW wind turbine. *Atmos Env*, 22(4):803-820, 1988.

Iungo, G. V., Wu, Y-T, and Porté-Agel, F. Field measurements of wind turbine wakes with lidars. *J. Atmos. Oceanic Technol.*, 30, 274–287, 2012.

Jacobson, M. Z. and Masters, G. M. Exploiting wind versus coal. *Science*, 293:1438, 2001.

Jacobson, M. Z., Archer, C. L. Saturation wind power potential and its implications for wind energy. *Proc. Natl Acad. Sci. USA*, 109(39):15679-15684, 2012.

Jensen, N. O. A note on wind generator interaction. *Risø National Laboratory, Roskilde, Denmark*, Risoe-M-2411(EN), 1983.

Kain, J. S. The Kain-Fritsch convective parameterization: An update. *J. Appl. Meteor.*, 43:170–181, 2004.

Katic, I., Højstrup, J., and Jensen, N. O., A simple model for cluster efficiency. *EWEA Conference*, 1986.

Kirk-Davidoff,D. B. and Keith, D. W. On the climate impact of surface roughness anomalies. *J. Atmos. Sci.*, 65:2215-2234, 2008.

Lettau, H. Note on aerodynamic roughness-parameter estimation on the basis of roughness-element description. *J of Appl Meteorol*, 8:828-832, 1969.

Larsén, X. G., Larsen, S., Hahmann, A. N. Notes and correspondence origin of the waves in 'A case-study of mesoscale spectra of wind and temperature, observed and simulated': lee waves from the norwegian mountains. *Q. J. R. Meteorol. Soc.*, 138:274–279, 2012.

Lin, Y.-L., Farley, R. D. and Orville, H. D. Bulk parametrisation of the snow field in a cloud model. *J. Climate Appl. Meteor.*, 22:1065–1092, 1983.

Lu, X., McElroy, M. B., Kiviluoma, J. Global potential for wind-generated electricity. *Proc. Natl Acad. Sci. USA*, 106:10933-8, 2008.

Marvel, K., Kravitz, B., Caldeira, K. Geophysical limits to global wind power. *Nature Climate Change*, 3:118-121, 2013.

Mesinger, G., Di Mego, E., Kalnay, K., Mitchell, P. C., Shafran, W., Ebisuzaki, D., Jovic', J., Woollen, E., Rogers, E. H., Berbery, M. B., Ek, Y., Fan, R., Grumbine, W., Higgins, H., Li, Y., Lin, G., Manikin, D., Parrish, D. and Shi, W. North American Regional Reanalysis. *Bull. Amer. Meteor. Soc.*,87:343–360, 2006.

Mlaver, E. J., Taubman, S. J., Brown, P. D., Iacono, M. J. and Clough, S. A. Radiative transfer for inhomogeneous atmosphere: RRTM, a validated corrected-k model for the long wave. *J. Geophys. Res.*, 102:16663–16682, 1997.

Mortensen, N. G., Heathfield, D. N., Myllerup, L., Landberg, L., and Rathmann O. Getting started with WAsP 9. *Risø National Laboratory, Roskilde, Denmark*, Risø-I-2571(EN), 2007.

Nakanishi, M., and Niino, H.. Development of an improved turbulence closure model for the atmospheric boundary layer. *J of the meteorol Soc of Jpn*, 87:895-912, 2009.

Nappo, C. J. An Introduction to Atmospheric Gravity Waves. *International Geophysics*, 2002.

Ott, S., Berg, J., and Nielsen, M.. Linearised CFD models for wakes. *Risø National Laboratory, Roskilde, Denmark*, Risø-R-1772(EN), 2011.

Peña, A., Rethoré, P.-E., Hasager, C. B. and Hansen, Results of wake simulations at the Horns Rev I and Lillgrund wind farms using the modified Park model. *Risø National Laboratory, Roskilde, Denmark*, DTU Wind Energy-E-Report-0026(EN), 2013.

Peña, A. and Rathmann, O. Atmospheric stability-dependent infinite wind-farm models and the wake-decay coefficient *Wind Energy*, 2013.

Petersen, L. P., Troen, I., Jørgensen, H. E., Mann, J. Are local wind power resources well estimated? *Environ Res Lett*, 8, 2013.

Pickett, M. H., Tang, W., Rosenfeld, L. K., Wash, C. H. QuikSCAT satellite comparisons with nearshore buoy wind data off the U.S. West Coast *J. of Atm. and Ocean. Techn.*, 1869:1879, 2003.

Porté-Agel, F., Wu, Y.-T., Lu, H., Conzemius, R. J.. Large-eddy simulation of atmospheric boundary layer flow through wind turbines and wind farms. *J Wind Eng Ind Aerodyn*, 99:154-168, 2011.

Porté-Agel, F., Wu, Y.-T., Chen, C.-H. A Numerical Study of the Effects of Wind Direction on Turbine Wakes and Power Losses in a Large Wind Farm. *Energies*, 6:5297-5313, 2013.

Réthoré, P-E Wind Turbine Wake in Atmospheric Turbulence *Risø National Laboratory, Roskilde, Denmark*, Risø-PhD-53(EN), 2009.

Réthoré, P-E, Sørensen, N. N., Zahle, F., Bechmann, A., Madsen, H. A. CFD model of the MEXICO wind tunnel. *Wind Energy Research*, 2011.

Réthoré, P-E, van der Laan, P., Troldborg, N., Zahle, P. and Sørensen,N. N. Verification and validation of an actuator disc model *Wind Energy*, 2013.

Risien, C., Vanhoff, B., Morini, D. F. QuikSCAT level 3 near-coast wind and stress fields with enhanced coastal coverage (OSU): US West Coast region. *PO.DAAC*, 1–23, 2011.

Prospathopoulos, J. M., Chaviaropoulos, P. K. Numerical simulation of offshore wind farm clusters *European Wind Energy Association, Conference proceedings*, 2013.

Prospathopoulos, J., Badger, J., Volker, P. J. H ., Sieros, G., Chaviaropoulos, C., Rethoré P.-E. Physical scale integration (coupled use). *EERA-DTOC*, 2013.

Ross, J. N. and Ainsie, J. Wake measurements in clusters of model wind turbines using laser Doppler anemomtry *Proc. 3rd BWEA Wind Energy Conf.*, Cranfield, United Kingdom, British Wind Energy Association, 17284, 1981.

Roy, S. B, Pacala, S. W., and Walko R. L. Can large wind farms affect local meteorology? *J. Geophys. Res*, 19, 2004.

Roy, S. B. and Traiteur J. J. Impact of wind farms on surface air temperature *Proc. Natl Acad. Sci. USA*, 2010.

Roy, S. B. Simulating impacts of wind farms on local hydrometeorology *J Wind Eng Ind Aerodyn*, 2011.

Skamarock, W., Klemp J., Dudhia J., Gill, D., Barker, D., Duda M., Huang X., Wang W., and Powers, J,. A Description of the Advanced Research WRF Version 3. *NCAR Technical note*, 2008.

Saleh, H., Abou El-Azm Aly, A., Adbel-Hady, S. Assessment of different methods used to estimate Weibull distribution parameters for wind speed in Zafarana wind farm, Suez Gulf, Egypt. *Energy*, 44:710-719, 2012.

Snel, H., Schepers, J.G. and Montgomerie, B. The MEXICO project (Model Experiments in Controlled Conditions): The database and first results of data processing and interpretation. *J. Phys.: Conf. Ser.*, 75, 012014, 2007.

Smith, R. B. Gravity wave effects on wind farm efficiency. *Wind Energy*, 13:449-458, 2009.

Sommer, A. Wind Resources at Horns Rev. *Report*, Eltra PSO-2000 Proj. nr. EG-05 3248, 2002.

Tennekes, H., and Lumley J. L.. A First Course in Turbulence. *The MIT Pess*, 1972.

Vermeer, L. J., Sørensen, J. N., Crespo A. Wind turbine wake aerodynamics *Progress in Aerospace Sciences*, 39:467-510, 2003.

Wang, C. and Prinn, R. G. Potential climatic impacts and reliability of very large-scale wind farms. *Atmos. Chem. Phys.*, 10, 2053:2061, 2010.

Volker, P. J., Badger, J., Hahmann, A. N., Ott, S. Implementation and evaluation of a wind farm parametrisation in a mesoscale model. *Sumitted*, 2013.

Wu, Y. T., Porté-Agel, F. Simulation of turbulent flow inside and above wind farms: Model validation and layout effects. *Boundary-Layer Meteorol*, 146:181–205, 2012.

Wyngaard, J. C. (2004), Toward Numerical Modeling in the "Terra Incognita", *Bull. Amer. Meteor. Soc.*, 61:1816-1826, 2004

Wyngaard, J. C. Atmosheric Turbulence. *Cambridge Press*, 2010.

Zhang, W., Markfort, C. D. and Porté-Agel, F. Near-wake flow structure downwind of a wind turbine in a turbulent bundary layer. *Exp. Fliuds*, 52:1219-1235, 2012.

This dissertation is submitted in partial fulfilment of the requirements for the degree of Doctor of Philosophy in Engineering at the Technical University of Denmark. The work was done at the Meteorology Section of the Department of Wind Energy and has been part of the WAUDIT project, financed by Marie Curie ESR-FP7.

Principal supervisor: Dr. Andrea N. Hahmann
Co supervisor: Dr. Jake Badger
Examiners: Dr.Pierre-Elouan Réthoré, DTU Wind Energy
Dr. scient. Idar Barstad, Geophysical Institute, University of Bergen, Norway
Dr. Nicolai Gayle Nygaard, Renewables Wind Assessment & Measurement, DONG

DTU Wind energy
Technical University of Denmark

Bygning 101 DTU Risø campus
Frederiksborgvej 399 P.O. Box 49
DK-4000 Roskilde
www.vindenergi.dtu.dk

ISBN 978-87-92896-76-6